Fiber Optic Distributed Temperature Sensing of Soil Moisture in Waste Rock

Robert Wu

Department of Earth and Planetary Sciences

McGill University

March 2021

A thesis submitted to McGill University in partial fulfillment of requirements of the degree of Doctor of Philosophy.

Abstract

One of the most challenging aspects of controlling contamination in mining operations is the management of tailings and waste rock piles. Waste rock is the material extracted from a mine that has no economic value and may be a source of contamination from acid or neutral mine drainage. Only in recent decades have mining operations incorporated covers in the design of waste rock piles to prevent the infiltration of water and oxygen, increase chemical stabilization, and minimize contaminant leachate. This thesis focuses on the distributed measurement of soil moisture in a waste rock pile using active fiber optic distributed temperature sensing (aFO-DTS). Soil moisture is measured by heating the metal casing of a fiber optic cable and evaluating the thermal response. This emerging geophysical method allows for the measurement of soil moisture continuously along several kilometers of fiber optic cable, with measurement spacing every half meter, and a temporal resolution of less than an hour per measurement.

In this thesis, I undertake three related projects: (1) A laboratory column experiment in which the fiber optic cable was buried in two layers of soils with different hydrogeologic properties. By using aFO-DTS, I evaluate the spatial resolution of soil moisture in the column and at the interface between the two layers of soil using the created protocol. (2) I apply my new aFO-DTS method to a constructed test waste-rock pile at the Lac Tio mine in eastern Quebec. The test pile is using a new capillary barrier cover design. By using aFO-DTS, I assess the temporal distribution of soil moisture at different depths within the pile. (3) I test uncertainties and common assumptions used by aFO-DTS methods using a numerical model. To date, there has been very little analysis of the potential errors related to subsurface heterogeneity and method calibration. The rate and period of recharge are found to be among the largest potential sources of error and require careful calibration when using the aFO-DTS method.

Résumé

La gestion des résidus miniers et des haldes à stériles est un des plus grands défis associés au contrôle de la contamination dans les mines. Les stériles sont constitués des matériaux extraits d'une mine qui n'ont aucune valeur économique et pourraient être source de contamination dans les eaux d'exhaure de mine acides ou neutres. Ce n'est qu'au cours des dernières décennies que les exploitations minières ont intégré des couvertures à la conception de haldes à stériles pour prévenir l'infiltration d'eau et d'oxygène, accroître la stabilisation chimique et minimiser la production de lixiviats contaminés. Le présent mémoire s'intéresse principalement à la mesure distribue de la teneur en eau dans une halde à stériles par la méthode active de mesure distribue de la température par fibre optique (MRT-FOa). La teneur en eau est mesurée en chauffant la gaine métallique d'un câble optique et en évaluant sa réponse thermique. Cette nouvelle méthode géophysique permet de mesurer la teneur en eau du sol en continu le long de plusieurs kilomètres de câble optique, à tous les demi-mètres et à une résolution temporelle de moins d'une heure par mesure.

Le présent mémoire décrit les trois projets suivants : 1) une expérience en colonne en laboratoire dans laquelle un câble optique est enseveli dans deux couches de sols de propriétés hydrogéologiques différentes. En utilisant la MRT-FOa, j'évalue la résolution spatiale de la teneur en eau des sols dans la colonne et à l'interface entre les deux couches en employant le protocole établi; 2) j'applique ma nouvelle méthode de MRT-FOa à une halde à stériles expérimentale à la mine du lac Tio, dans l'est du Québec. La halde expérimentale intègre un nouveau concept de couverture à barrière capillaire. J'utilise la MRT-FOa pour examiner la répartition temporelle de la teneur en eau à différentes profondeurs dans la halde; 3) j'évalue les sources d'incertitude et je procède à la validation d'hypothèses courantes des méthodes de MRT-

FOa en utilisant un modèle numérique. Les erreurs potentielles reliées à l'hétérogénéité de la subsurface et à l'étalonnage des méthodes ont été très peu analysées à ce jour. Le taux et la période de recharge representent parmi les plus grandes sources potentielles d'erreur et doivent être soigneusement étalonnés quand la méthode de MRT-FOa est utilisée.

Table of Contents

List of Figures

(Captions abridged)

Contribution to Original Knowledge

Active fiber optic distributed temperature sensing (aFO-DTS) is an emerging technology to measure soil moisture along a fiber optic cable. While the method has the potential to be an important tool for hydrology (i.e., cables can be greater than one km in length with sub-meter measurement spacing), research in using the technology for applied research at an industrial capacity has not previously been published.

This project is the first to apply aFO-DTS for measuring soil moisture and geoenvironmental monitoring in a mine setting. Using both field and laboratory studies, my research provides a new and improved theoretical understanding on the movement of water through a waste rock pile and also important technological advances in geophysical approaches for mine environmental monitoring. Previous research has demonstrated that aFO-DTS has the potential to measure soil moisture in controlled settings. I created a protocol that demonstrates the effectiveness of aFO-DTS in an industrial capacity and in soils that previously represented challenges for traditional in-situ tools to measure soil moisture.

My PhD research also elucidates the challenges and limitations of the aFO-DTS method through a parametric numerical modelling approach. My PhD represents the first effort to incorporate the effects of parameters changes to calibration accuracy, including length of time of recharge and different heterogeneity scenarios. The results contribute to knowledge in a new but understudied technology that is simultaneously incorporated in new geoenvironmental monitoring solutions.

Acknowledgements

A special word of sincere appreciation is extended to my supervisor, Dr. Jeffrey M. McKenzie, for his leadership over the course of my time at McGill. Jeff possesses the qualities of a great leader and allowed me to become a confident and independent researcher, while providing full support and guidance during the more challenging periods of my studies. It has been my privilege to work with him and have learned tremendously from the environment he has created. My thesis would not have been possible without his support and facilitation.

It has been a privilege to work with the best and the brightest from the Research Institute of Mines and Environment. In particular, Dr. Vincent Martin has been instrumental in facilitating the technical and logistical challenges of my thesis. Furthermore, I would like to thank Noura El-Harrak and Lukas Cheung their help in creating a productive environment when I first joined the project. This project would also not have been possible without the support of Dr. Michel Aubertin, Dr. Bruno Bussière, and Dr. Stephan Broda who have all helped me grow as a researcher by providing engaging discussions and fieldwork opportunities.

I would also like to thank Pierrick Lamontagne-Hallé for his support and friendship throughout my thesis as well as the current and past members of the Laboratory of Advanced Hydrogeological Modelling and Stuff (LAHMAS) including Lauren Somers, Laura Lyon, Pan Wu, Lin Chen, Greg Langston, and Sam Zipper.

Finally, I would like to thank my parents for their moral support without which none of my success would have been possible.

Contribution of Authors

This thesis is composed of three manuscripts of which I am first author, in collaboration with colleagues. My supervisor, Jeffrey M. McKenzie, is a co-author in all three manuscripts for his contribution to the vision of the projects and manuscript editing.

The first manuscript (Chapter 2) was published in *Canadian Geotechnical Journal* in 2020. Vincent Martin and Stefan Broda are included for their contribution in the initial setup of the experiment and suggestions in the manuscript. Bruno Bussière and Michel Aubertin contributed to the project vision as well as manuscript editing. Barret Kurylyk is included for his insights into the mathematical complexities of our approach. *Wu, R., Martin, V., McKenzie, J., Broda, S., Bussière, B., Aubertin, M. and Kurylyk, B.L. (2020), Laboratory-scale assessment of a capillary barrier using fibre optic distributed temperature sensing (FO-DTS). Canadian Geotechnical Journal, 57(1), pp.115-126.*

The second manuscript (Chapter 3) was published in *Groundwater* in 2021. Similar to Chapter 2, Vincent Martin, Stefan Broda, Bruno Bussière and Michel Aubertin are co-authors as they contributed to the project vision as well as manuscript editing. Stefan Broda and Vincent Martin initially installed the apparatus at the mine site. John Selker is a co-author for his help in the initial design and implementation of the project. *Wu, R., Martin, V., McKenzie, J.M., Broda, S., Bussière, B., Selker, J. and Aubertin, M. (2021), Fiber Optic Measurements of Soil Moisture in a Waste Rock Pile. Groundwater. Accepted Author Manuscript. https://doi.org/10.1111/gwat.13075*

The third manuscript (Chapter 4) is submitted for publication in *Vadose Zone*. Pierrick Lamontagne-Hallé is included as a co-author for his expertise and assistance in implementing the groundwater modelling as well as manuscript editing.

1. Introduction and Literature Review

1.1. Waste Rock Piles

A major challenge in mining and geotechnical engineering is the construction of reliable long-term waste rock piles. Waste rock piles have the potential to be significant, long-term sources of environmental contamination. New waste rock pile designs have been developed to incorporate inclined cover systems to prevent water from entering the pile interior, an approach that uses capillary forces to effectively block the influx of water into waste rock pile. A key design consideration for these covers is limiting factors that may have influenced effluent discharge due to interactions between water, air and the waste rock material. The purpose of this introduction is to highlight key points and recent progress in developing a waste rock pile that is isolates reactive material from the surrounding environment. I also discuss current methods used to monitor how water interacts with the waste rock pile interior and introduce the active fibre-optic distributed temperature sensing (aFO-DTS) method to assess the effectiveness of waste rock cover strategies.

Waste rock piles are heterogeneous coarse-grained mounds that are constructed from mined rock that has no economic value and thus, will not be transported to refining processing facilities. These waste rock piles, often hundreds of meters in height, are permanent man-made structures deposited at a mine site. In high cut-off grade mining, however, the waste rock piles may act as a secondary ore supply in cases where commodity prices make it viable to extract lower grade ore from waste rock.

Traditionally, waste rock piles were constructed using various, poorly-documented methods. Many of these methods did not consider pile stability nor environmental consequences that could arise as a result of leachate migrating from the pile. Distinct construction techniques will result in varying amounts of compaction and grain size distribution; these two factors can have significant effects on how fluids move through the interior of the waste rock pile (Aubertin et al., 1998; Fala et al., 2005).

Fluid migration through a waste rock pile is a relatively new area of research. Over the last few decades, researchers and mining companies are becoming more conscious of environmentally friendly reclamation stage mining techniques. One major concern relates to leachate migration out of waste rock piles and into the surrounding environment. This can be exceptionally problematic with sulfide bearing (ex. porphyry, Ag/Au, diamond) and heavy metal bearing (ex. REE, Li, pegmatite) waste rock.

Precipitation events and heavy winds may create conditions where water and oxygen can react with the waste rock material. For example, oxygen may react with pyrite in a sulphide bearing waste pile, producing sulphuric acid. Such exothermic reactions can drive temperature and pressure gradients within the pile interior and create a positive feedback loop that results in more sulphuric acid production and lower pH in the resulting leachate (Lefebvre et al., 2001; Fala et al., 2005). With the possible addition of heavy winds and snow cover, the contrast in temperature and pressure within the pile can be quite significant and amplify the complexity of moisture storage by producing vapour and condensation within the waste rock pile (Fala et al., 2005). Methods to create a catalyst to turn the sulphuric acid back into a precipitate (pyrite) have been developed and are utilized today in several diamond mines (Amos et al., 2009). However, such composite is expensive to produce and there has been a lack of research into the environmental hazards of the catalyst itself. A more constructive solution may be a preventative system in which leachate production is mitigated by reducing the probability of waste-fluid interactions.

Waste rock piles are commonly constructed by several different methods; the most utilized method is *end dumping*, whereby dump trucks unload the waste off the crest of the pile. This is often accompanied by *push dumping* where the waste rock is dumped at the crest of the pile and pushed over the edge (Fala et al., 2010). These two methods often result in layered, compacted sublayers with finer grained material is often found at the bottom of these sublayers. *Push dumping* often results in less segregated grain size distribution because of lower initial angular velocities of the larger material when pushed over the crest of the waste rock pile (Fala et al., 2005). *Free dumping* is often used to create the base of a waste rock pile. Waste material is dumped in heaps and subsequently spread flat. This method produces the least amount of grain size segregation (Fala et al., 2010). When the grain size distribution of the waste rock pile is well graded, the vertical profile will appear heterogenous throughout the pile. Such heterogeneity can affect how water can oxygen move through the pile, including potentially promoting the movement of water through deeper parts of the pile.

1.2. Capillary Barrier Cover Systems on Inclined Slopes

Several methods have been proposed to limit the environmental ramifications due to moisture ingress into waste rock piles. One viable method involves a design framework that limits the amount of water that can infiltrate into the waste rock pile core by using an overlying cover material with low saturated hydraulic conductivity properties.

Another approach is the construction of a cover system that will limit wind driven advection of gas migration into the pile. This is heavily favoured in sulphide bearing waste rock piles due to the relationship between sulphide oxidation reactions and gas gradients that exist in waste rock piles due pressure differences caused by temperature differences and advection cells near the pile exterior (Amos et al., 2009). A possible challenge with these types of cover systems stems from the difficulty in maintaining an effective oxygen barrier due to unsaturated pockets that can exist in sloped areas (Bussière et al., 2003). Nonetheless, Amos et al. (2009) demonstrated that these systems can work in arid and semi-arid climate, such has the Canadian north, where cover system designs are not in limiting precipitation and snowmelt, but rather reducing temperature gradients in and around the waste rock pile.

An additional viable option are waste rock covers that induce capillary barrier effects. These cover systems have been proposed as an alternative to traditional cover systems to prevent gas and liquid migration through waste rock piles (Morris et al., 1997; Bussière et al., 2003). This is an increasingly attractive alternative to cover systems that rely on low saturated hydraulic conductivity (Aubertin et al., 2009). Cover systems with capillary barrier effect use material that can be found at or near the mine operation and are relatively simple to construct. Furthermore, the durability of the cover is strong due to the probable low plastic nature of these materials (Bussière et al., 2007).

Such cover systems work by relying on the capillary phenomenon that exists in fine grained soils. Water tends to "stick" to finer grained materials under unsaturated water content due to capillary (adhesive and cohesive) forces as finer materials have high water retention capacities. This can be represented on a water retention curve, where cohesive forces are dominant at high suction values before the water entry inflection point and reflected by a large air entry value (Figure 1.1). The air entry value is the pressure where the maximum pore diameter starts to drain. The tendency to store water means less water can leave the overlying medium and thus the material does not drain easily (Aubertin et al., 2009).

The capillary barrier system is created by situating fine, non-reactive waste material on top of the coarse waste rock pile. The contrast between the grain size of the two layers will induce water retention in the overlying finer cover until the pressure of the overlying water becomes stronger than then capillary force. The unsaturated hydraulic conductivity of the waste rock layer is also lower than that of the cover system at the same suction pressure because the coarse material is easily drainable, which helps keep the water in the overlying fine layer (Bussière et al., 2003). Thus, the net result is that the water retention property is stronger in the finer grained material.

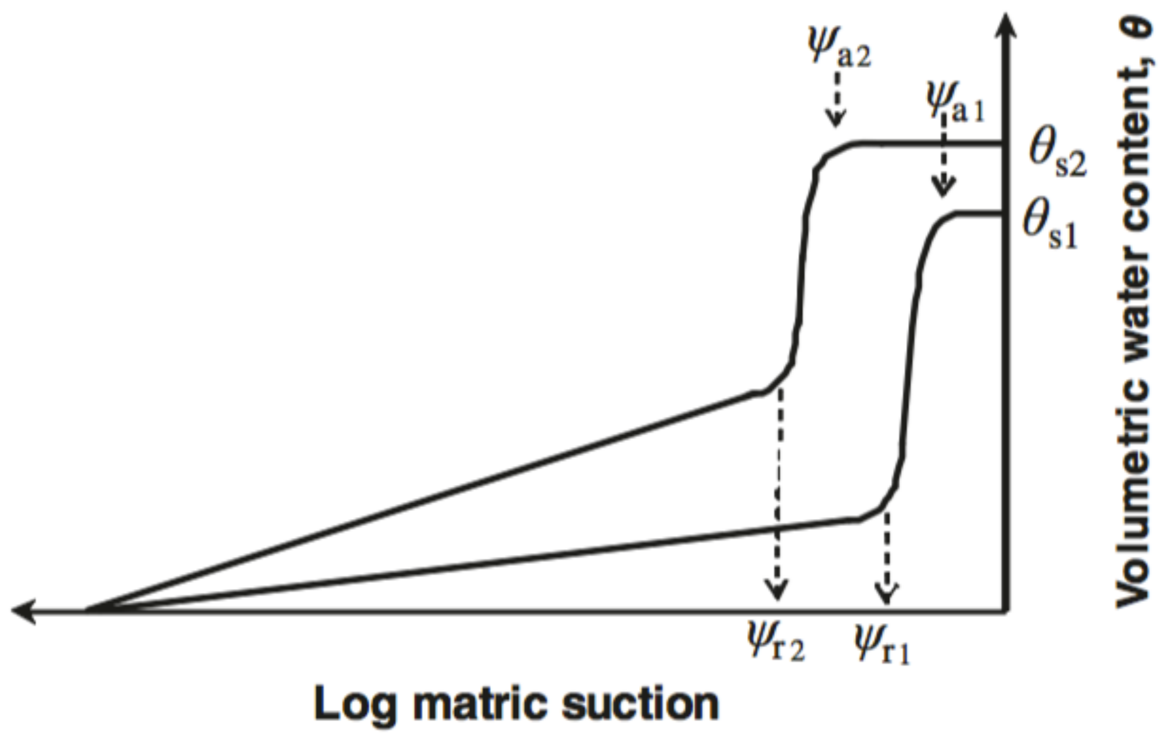

Figure 1.1: Water retention curves of a coarse grained material (1) and fine grained martial (2) with their respective water and air entry values (Aubertin et al., 2009).

Water, when it reaches the capillary barrier between the cover and waste rock, will be retained at this boundary until the suction of the cover material decreases sufficiently due to an increase in the overlying weight of added water. Water will then drain the waste rock region when the suction pressure approaches the water entry value of the coarse material (Figure 1.1). This representative value means the waste rock layer increased beyond residual water contents. Water will start to flow within the waste rock interior because the volumetric water content that exists in the cover system exceeds what the capillary suction can hold. In the design of an effective cover system the water entry value of the cover system should be much larger than that of the waste rock, in addition to a high air entry value (Aubertin et al., 2009).

When the cover system is inclined, the water entry value can help represent how far down slope water will travel in the cover layer before infiltrating into the waste rock. At some distance downslope, the moisture accumulated in the cover material will cause a shift below the pressure associated water entry value in the waste rock layer. Aubertin et al. (2009) describe this point as the *down dip limit* and the length between this point to the top of the slope as the diversion length.

Consideration of local climate must be taken in assessing the down dip limit. In semi-arid environments, short and intense rainfalls can penetrate the pile before the *down dip limit* and long-term rainfall events in humid areas may reduce a cover's reliability (Aubertin et al., 2009). A cover material must be made from a fine-grained material that can have strong capillary forces and high unsaturated hydraulic conductivity. A common assumption is that clayey soils may be suitable owing to its characteristic behavior to hold onto water, thus well suited for capillary action. However, such a soil texture has the tendency to retain water for exceeding long periods of time. Thus, clayey material may not be suitable as a cover material, especially in climates where long and recurring precipitation events are common. In an ideal cover, there should be balance between capillary action and downslope fluid migration; water should be held within the cover but able to migrate towards the toe of the pile.

From a practical standpoint, increasing the thickness of the cover layer will increase the effectiveness of the cover system because there will be more material to hold water and subsequently prevent gas from entering the waste rock medium. Aubertin et al. (2009) show that increasing the thickness of the fine-grained layer will improve cover efficiency, but such relationship is not linear. Beyond a certain threshold, excess thickness becomes unwarranted due to cost of material and construction.

1.3. Water Content and Matrix Suction Relationship

When analyzing the efficiency of an inclined cover in a lab setting, it is often useful to compare results with that of numerical models. Bussiere et al. (2003) attempted to show this relationship with an inclined box combined with predictive modelling. Figure 1.2 displays the results of the study of a two layered covered waste rock system.

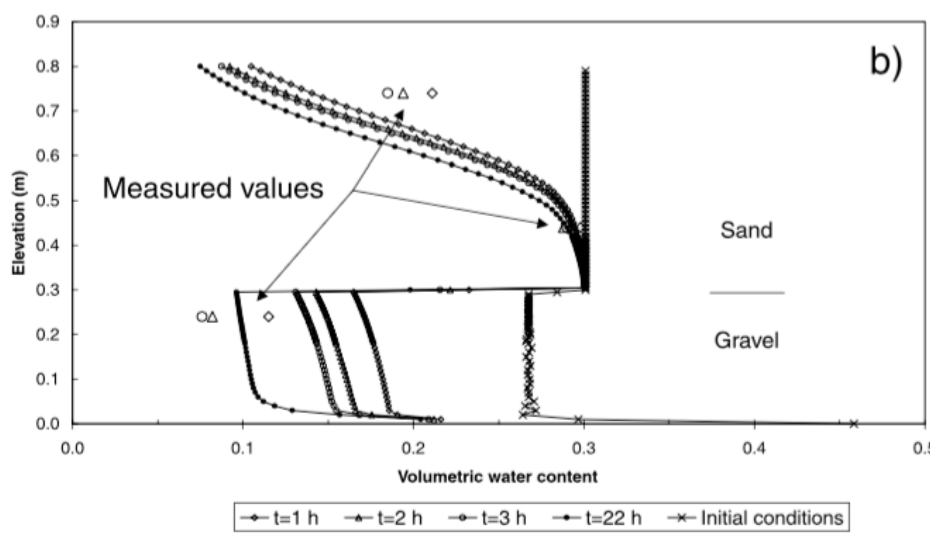

Figure 1.2: Volumetric water content at various stages in the drainage period across a sand-gravel capillary barrier (from Bussiere et al. 2003).

Due to the high saturated hydraulic conductivity and poor retention capability of the waste rock layer, the moisture content is much lower than the finer material above. The lower part of the sand layer (closer to the capillary break) has a higher water content because water can seep through the upper portion where the matrix suction is higher and exceeds the air entry value (Bussiere et al., 2003). Designs have been tested with several degrees of declination, showing higher degrees of saturation near the toe of the slope and increase pressure near the top of the slope in the sand layer as a function of increased declination. Thus, desaturation can commonly occur at the top of the slope in the fine cover material due to higher suction (Bussiere et al., 2003). These tests demonstrate that the effectiveness of the cover system to prevent water infiltration and reduce gas flux is a partial function of the declination slope angle.

The *down dip limit* represents the water entry value whereby the *down dip limit* is the inflection point where the matrix suction in the waste rock layer becomes low enough for water to start accumulating above residual values. Several methods have been developed to find the location of the air entry value. These methods include fitting experimental data to a soil characteristic curve, such as the van Genuchten soil characteristic curve (van Genuchten, 1980), using the tangent of the inflection paths, and basing the location at 90% saturation (Aubertin et al., 1998). Understanding how this parameter behaves on a water retention cure is key to creating an effective cover system. However, a contrast between water retention properties of the fine and coarse layer can lead to better capillary effect but does not necessitate a better diversion length (Broda et al., 2015).

1.4. Numerical Modelling of Unsaturated Flow in Covers

Numerical simulations indicate prominent factors that affect the diversion length of covers include the thickness of the cover layer, material strength, and precipitation (and more generally) recharge rates of the area (Aubertin et al., 2009). These factors are represented in Figure 1.3. The diversion length is affected more by precipitation when the cover layer is thinner. The *down dip* *limit* is closer to the head of a slope for large precipitation events.

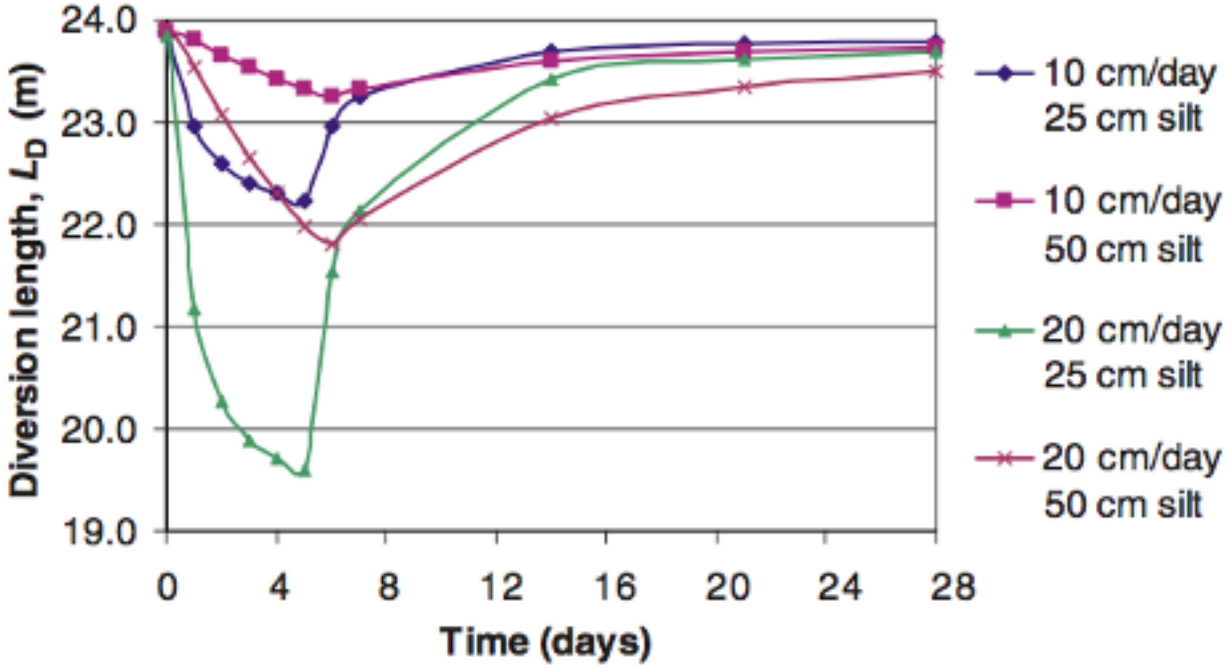

Figure 1.3: Thickness of a sand layer with its relationship to the diversion length in a cover system (from Aubertin et al., 2009).

Aubertin et al. (2009) concluded that the optimal thickness to divert water along a slope in a two-layer system is about 1.0 to 1.5 m thickness (Figure 1.4). Beyond this thickness, the relationship plateaus. This must be taken into consideration when constructing the waste rock pile where we need the down dip limit to be longer than the point down slope where the reactive rock lies underneath.

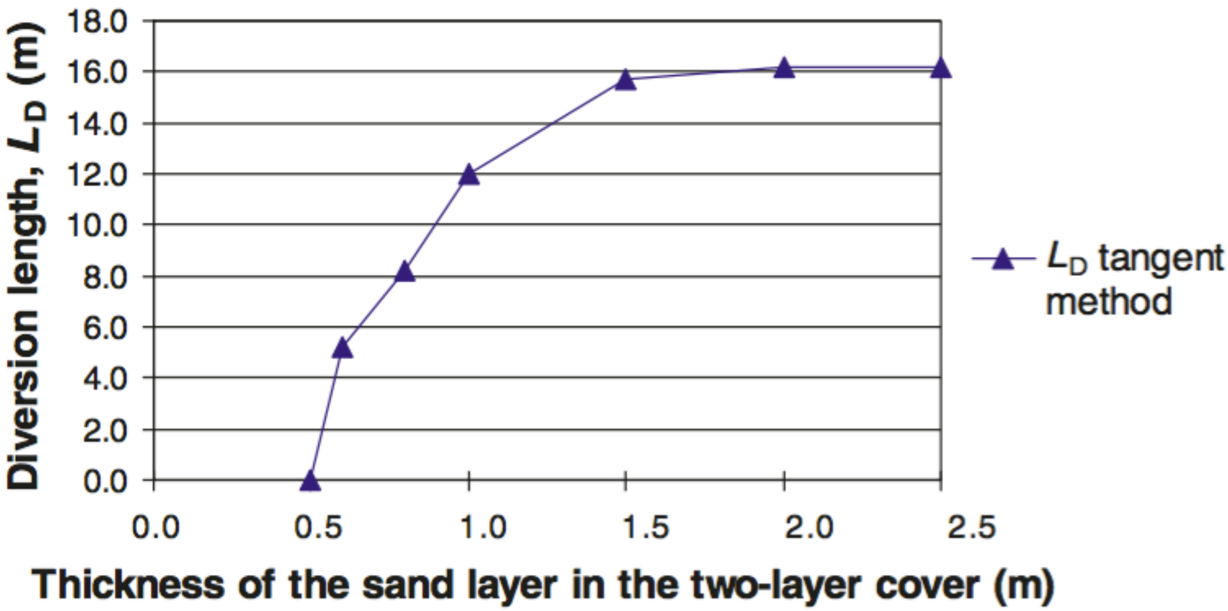

Figure 1.4: Diversion length through time for a 10cm and 20cm cover layer (Aubertin et al., 2009).

Aubertin et al. (2009) found that the diversion length can also shorten when the slope of the cover is less steep. Variables such as material availability and precipitation rates will dictate the declination angle of the cover and cover erosion has a strong control on the length of the down dip limit. The advantage of creating a capillary barrier system is that many other cover systems cannot be constructed easily without durability issues on the inclined surfaces.

When choosing the type of material for the cover system, the properties of sand size particles is a compromise between water retention properties and cost associated with material crushing and grinding. Fala et al. (2005) recorded simulations with a sand covered gravel layer and suggests that a sloped capillary barrier system can divert moisture from the waste rock pile interior. With a flat cover system, flow channels are more likely to form and can penetrate the barrier system easier. A sloped layer forces flow towards the toe of the pile and the sand can maintain low levels of saturation at its center without letting water enter the coarser section below (Fala et al., 2005). This study has theoretical simulations such as a waste rock pile of homogenous gravel and homogenous sand. After an amount of time, the water content in the sand pile is lower than the gravel pile (Fala et al., 2005). Despite this situation, the water that infiltrated into the sand layer spreads further than in the gravel pile (Figure 1.5). This can be explained by the higher capillary pressure associated with finer materials. At residual water content values, the relative permeability of fine material is higher so there is an additional force acting on water.

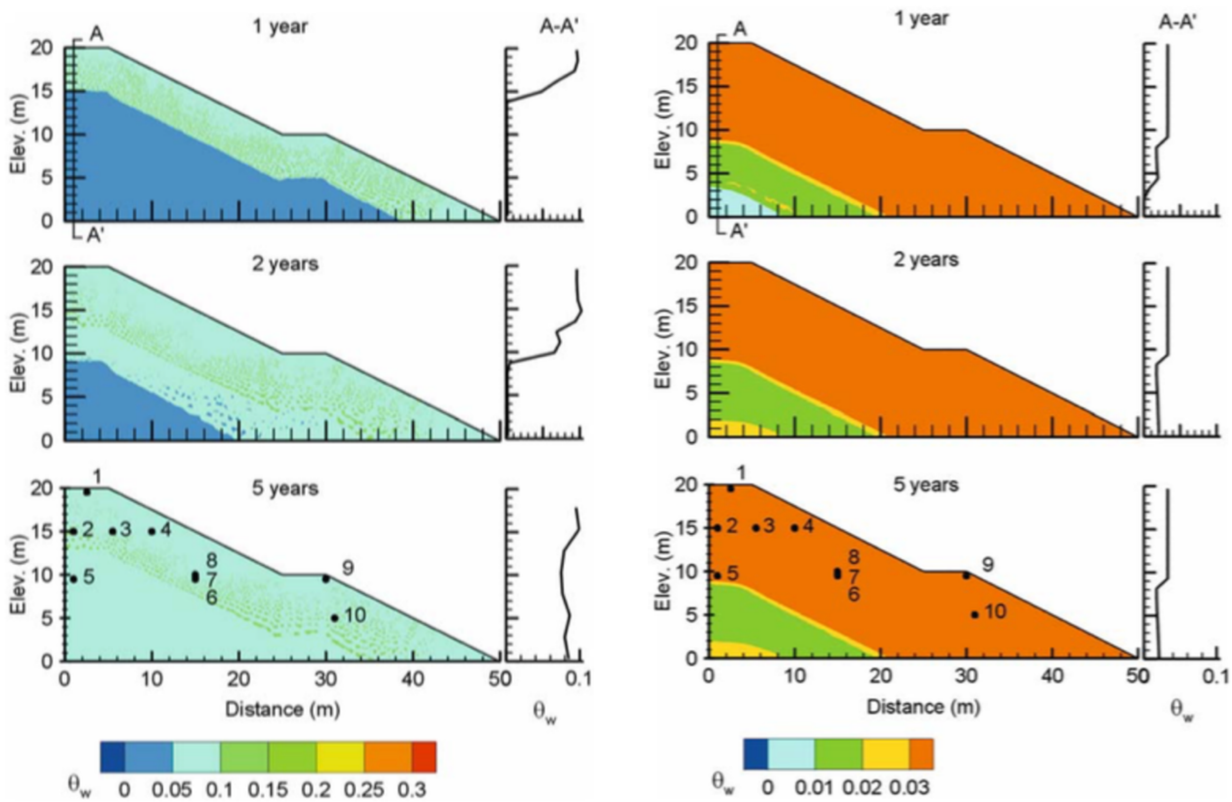

Figure 1.5: Time simulations of a homogenous gravel (left) and sandy material through a waste rock pile (adapted from Fala et al., 2005).

Fala et al. (2005) were also one of the first to simulate capillary barrier action in a waste rock pile. The bottom color plot in Figure 1.6 shows a break in the capillary barrier. There are many more of these breaks in the flat cover compared with the inclined cover. The breaks were randomly generated due to localized preferential flow regions. In the tiled cover systems, these vertical flow regions are limited, and water flows as the toe of the cover. The waste rock directly adjacent to the cover system is completely dry. This suggests that the efficiency of the capillary barrier cover system is better when there is a sloped angle to divert water. However, the homogeneity of the pile affects how quick and deep the water infiltrates through the pile (Fala et al., 2005). As a result, stratified layers throughout the pile can cause flow regimes and do not work well when compared to the sloped system.

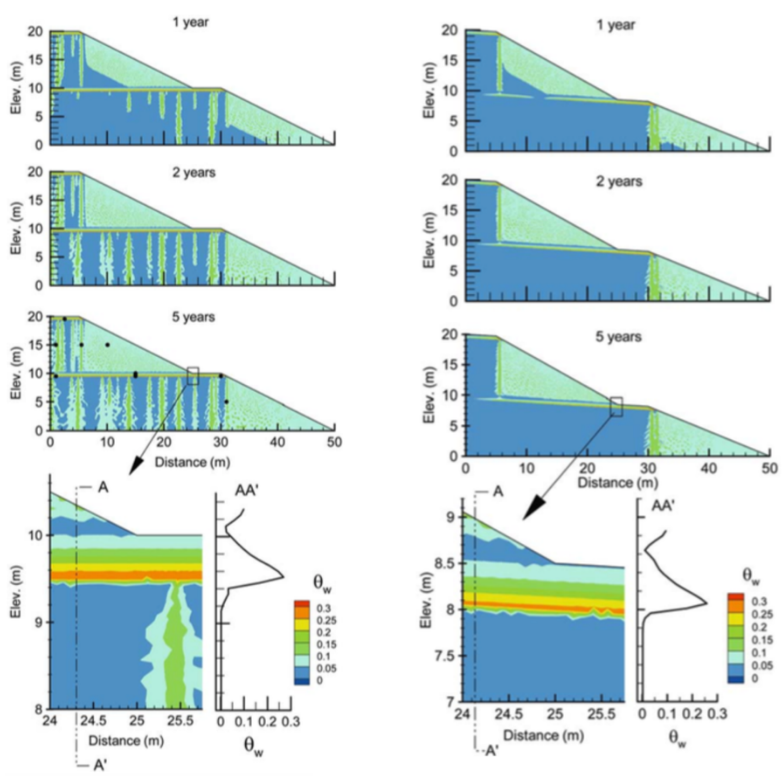

Figure 1.6: Randomly generated fractures and modelled efficiency of a flat (left) and declined (right) system (adapted from Fala et al., 2005).

The exact value of the slope declination angle, layer thickness and layer spacing depends on the material available at or near the mine site as well as the local precipitation rates. Since flow rates in the cover are low, the stability of the material is not a significant concern (Fala et al., 2010). An inclined cover has been modelled to show promise as an effective cover system.

Broda et al. (2015) illustrate avenues of infiltration mitigation by minimizing precipitation into the waste rock pile interior by modelling with random generated fractures in the coarse waste rock pile. This may be a more appropriate representation of waste rock piles since fractures and flow channels are common features. Fractures may play an import role especially in design efficiency, especially near the capillary break. These results were meant to be used for guidelines for efficient covers with capillary barrier effect.

The model suggests that the air entry value influences the amount of water that can seep through the capillary system. The larger the air entry value, the more water can infiltrate, although this can be locally enhanced if fractures are present. The degree of saturation at the capillary break is less with the presence of fractures (Figure 1.7). This result implies that fractures can decrease the efficiency of the capillary barrier at localized spots (Broda et al., 2015). The paper’s strongest argument for fractures having a large influence on capillary efficiency comes from decadal-length simulations.

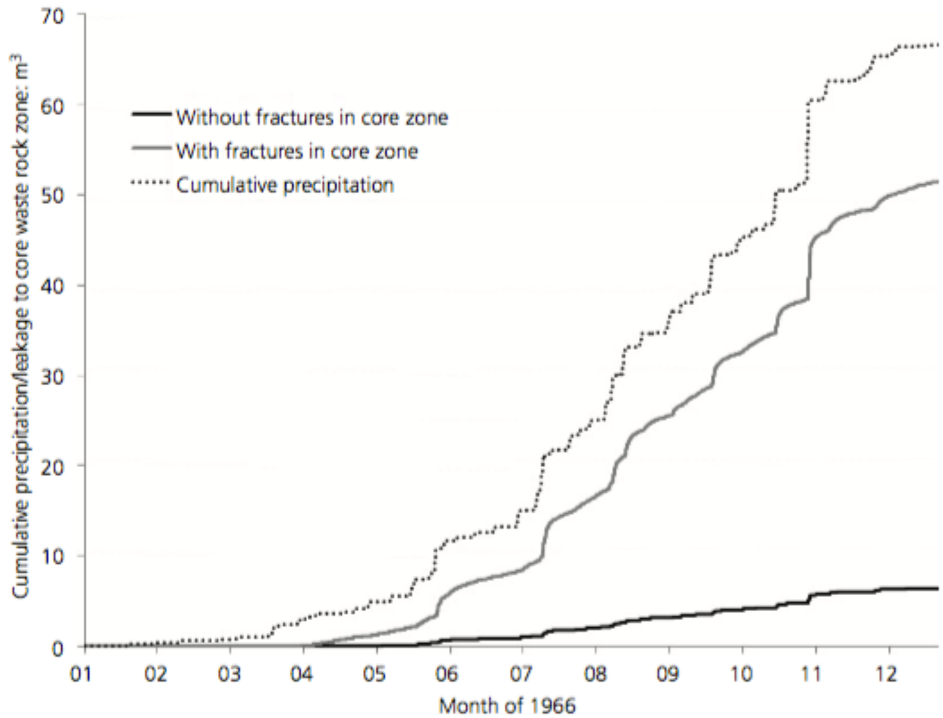

Figure 1.7: Cumulative precipitation and infiltration values for trials with and without fractures (from Broda et al., 2015).

The model outcomes show that more water enters a waste rock pile with fractures compared to models without (Figure 1.8). Nearly 80% of the precipitation infiltrated into the waste rock pile with fractures, compared with 12% in simulations without fractures. Broda et al. (2015) state that the simulations are considered conservative as all precipitation seeps into the fine-grained layer; there is no water loss due to runoff or evaporation.

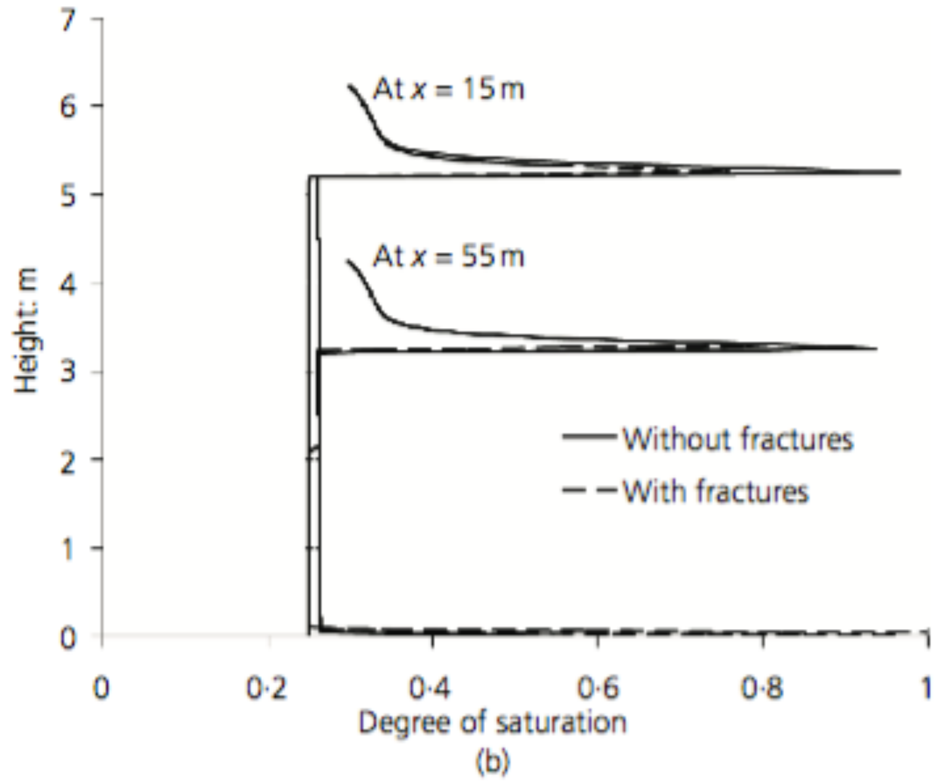

Figure 1.8: Vertical profiles associated with degree of saturation of trials with and without fractures (Broda et al., 2015).

1.5 Active Fiber Optic DTS Sensing to Evaluate Waste Rock Pile Cover Performance

Active fiber optic distributed temperature sensing (aFO-DTS) is a method to measure soil moisture along a fibre-optic cable, and can be used to assess the performance of a covered waste rock pile. By heating the fiber-optic cable, and then monitoring the heat dissipation, soil moisture (i.e. water content) can be calculated. The aim of this method is to interpret fiber optic temperature measurements from a waste rock pile to observe if an experimental cover system is able to divert water away from the core and thus prevent leaching of potential contaminants.

aFO-DTS operates via nonelastic Brillouin and Raman backscattering. In Raman backscattering, a change in the intensity of the reflected light occurs when incident light strikes the fiber optic glass wall and causes reflection at two frequencies, which are referred to as Stokes and anti-Stokes frequencies (Selker et al., 2006). The intensity of backscatter at the anti-Stokes frequency is dependent on the temperature of the cable, so temperature can be calculated from the ratio of intensity of the anti-Stokes to Stokes (Grattan and Sun, 2000; Ciocca et al., 2012). The precision of this measurement is proportional to the square root of the integration period or the square root of the time in one step interval assuming no errors in temperature drift (Selker et al., 2006; Sayde et al., 2010; Ciocca et al., 2012). FO-DTS systems are portable and are used for many environmental and hydrologic applications (e.g. Selker et al., 2006; Bense et al., 2016). The rugged and compact nature of this tool makes it a good candidate to evaluate soil conditions in harsh environments.

To obtain volumetric water content, heating cycles create heat signatures based on the duration and temperature increase of the cable during the heating event. The magnitude of these signatures will correspond to specific moisture contents. We can heat the fiber optic cable by attaching a power supply to two ends of the cable. The steel sheath that surrounds fiber optic cables generates heat when an electrical current is applied across it. When the cable is buried in a porous medium (e.g. soil), the change in temperature induced by the current on the fiber optic cable is dependent on the thermal conductivity and heat capacity properties of the medium, including the porous soil, air, and moisture. Assuming that the thermal properties of the solid porous media do not change with time and the contact resistance to the medium is not affected by hysteresis, the change in temperature during a heating cycle should be a function of changes in moisture content in the soil. As air has a very low thermal conductivity and density, it is assumed to have negligible effects on the bulk thermal properties of the medium (de Vries, 1963; Kluitenberg, 2002).

2. Lab scale Assessment of a Capillary Barrier using aFO-DTS

Authors: Robert Wu, Vincent Martin, Jeffrey M. McKenzie, Stefan Broda, Bruno Bussière, Michel Aubertin, and Barret L. Kurylyk

2.1. Abstract

Recent waste rock pile designs have been proposed to incorporate a fine-grained layer to create a capillary barrier to prevent surface water from draining into the pile interior. This study analyses active fiber optic distributed temperature sensing (FO-DTS) as a tool to measure the effectiveness a capillary barrier system following an infiltration test. A laboratory waste rock column was built with anorthosite waste rock overlain by sand. Volumetric water content is calculated during heat cycles lasting 15 min powered at 15 W/m in the column. A new algorithm is employed to circumvent several requirements for soil specific calibration. The inferred moisture contents were verified by soil moisture probes located adjacent to the cable. The FO-DTS data indicate, at vertical resolutions up to 2 cm, that water is retained in the sand and does not drain into the anorthosite following the infiltration test. The coefficient of determination, R2, between the inferred and measured volumetric water content in the fine cover sand layer is 0.90, while the screened anorthosite maintained an R2 of 0.94 with constant moisture content throughout the test. This study will ultimately help guide future waste rock storage design initiatives incorporating fiber optic sensors, leading to improved environmental mine waste management.

2.2. Introduction

Waste rock, extracted coarse-grained rock below the ore cut-off grade, is stored on the surface of mine sites and exposed to natural climatic conditions. The most common method to store this material is through constructed waste rock piles. These piles can be large, with heights exceeding hundreds of meters and area covering tens of hectares (Martin et al., 2005; Aubertin 2013). The typical design and construction methods for waste rock piles may create favourable conditions for the internal flow of fluids, which in turn may promote the development of acid mine drainage or contaminated neutral drainage where water is discharged as contaminated leachate from the pile (Morin et al., 1991; Bussière et al., 2005; Aubertin 2013; Chi et al., 2013). Waste rock piles generally exhibit hydrologic heterogeneity, particle segregation, sorting along slopes, and compacted layers due to machinery traffic (Bussière et al., 2003). The net-effect of these structures is the enhancement of water and air flow through the waste rock pile and the potential generation of acid mine drainage and contaminated neutral drainage (see Morin et al., 1991; Herasymuik 1996; Newman et al., 1997; Wilson et al., 2000; Aubertin et al., 2002a; Aubertin et al., 2002b; Fala et al., 2003; Fala et al., 2005; Martin et al., 2005).

Several modified designs and engineering improvements in and around waste rock piles have been proposed over the past 25 years to limit the generation of contaminated leachate. The optimal design of waste rock piles depends on their specific purpose and environmental setting. One potential design improvement is based on the concept of an inclined cover with a capillary barrier effect (CCBE) (Aubertin et al., 2002b; Bussière et al., 2003; Fala et al., 2005; Martin et al., 2005; Aubertin 2013). This type of multilayered system consists of a relatively fine-grained moisture retaining material above coarser waste rock to create a capillary break that limits infiltration into the pile interior (Rasmusson and Erikson 1986; Nicholson et al.1989; Morel-Seytoux 1992; MEND 2.22.2 1996; Aubertin et al., 1996; Bussière and Aubertin 1999).

An effective capillary barrier exists at the interface of the coarse layer and the overlying fine material, where suction remains above the water entry value of the coarse material, preferentially retaining water in the overlay. When relatively dry, the lower coarse-grained material has a very low unsaturated hydraulic conductivity, while the fine layer exhibits stronger water retaining capabilities and tends to retain moisture (Bussière et al., 2003; Aubertin et al., 2009). When the layered system is inclined, it enhances diversion down slope through the fine-grained layer. Capillary barrier systems are relatively straightforward to construct and durable, which may decrease the costs compared to other systems (Bussière et al., 2003).

To date, there are only a few technological options available for monitoring soil moisture in industrial settings. Point measurements (e.g. dielectric-permittivity soil moisture sensors) are commonly used, but they may cause difficulties during installation and when extrapolating data across large areas given system heterogeneities. Remote sensing techniques overcome some of these limitations but may resolve moisture content at resolutions that are too coarse for research purposes. In many circumstances, a combination of methods are used to understand the nature and distribution of soil moisture (e.g. Andrieau et al., 2010; Dobriyal et al., 2012).

One emerging method to evaluate soil moisture is fiber optic distributed temperature sensing (FO-DTS). This system records the thermal response of a medium to natural or engineered thermal forcing. FO-DTS can measure temperature along a fiber optic cable at fixed intervals (e.g. 0.5 m/span>) based on the temperature sensitivity of the backscattering of a light signal (Selker et al., 2003). In the last 20 years, actively heated FO-DTS techniques, for which the cable operates as both a heat source and a thermal sensor, have been developed to measure soil moisture (i.e. Weiss 2003).

The advantages of active FO-DTS is that it is a flexible sensing apparatus that can be deployed over large areas with relative ease and for indefinite periods of time. It has been shown to accurately measure temperature across a fiber optic cable over 30 km (Ciocca et al., 2012) and help delineate groundwater flow systems (Briggs et al., 2012). While active FO-DTS has been shown as an effective method to assess soil moisture, there are only few instances of the technology being used in applied industry settings (i.e. Weiss 2003; Benitez-Buelga et al., 2014). This technology is presently in use at an experimental waste rock pile, as part of an ongoing field monitoring program conducted by the authors and collaborators (Bréard Lanoix 2017; Martin et al., 2017).

This paper presents a laboratory experiment using active FO-DTS to measure temporal and spatial variability of aggregate and soil moisture in a large column. The main objective is to assess the applicability of active FO-DTS to resolve volumetric water (moisture) content, θ, in a controlled system that encourages the formation of a capillary barrier, much like the conditions created by a CCBE. This objective is achieved by using a large experimental column for which environmental conditions are controlled. In this study, the heating profiles of a fiber optic cable are used directly to infer volumetric moisture contents rather than the common approach of integrating the heating profiles to infer thermal properties soil to then estimate the moisture content through an empirical calibration curve. In other words, the approach discussed in this paper circumvents the need to determine the soil specific thermal properties (i.e. heat capacity, specific heat) to estimate θ and builds upon earlier studies developing semi-empirical approaches to evaluate the moisture content (Sayde et al., 2010). This technique is beneficial when working with heterogeneous and granular (cohesionless) media where thermal properties can vary greatly with grain size distribution and grain contact with the fiber optic cable.

2.3. Methods

Fiber optic distributed temperature sensing (FO-DTS)

FO-DTS uses fiber optic technology with nonelastic Raman backscattering. In Raman backscattering, a change in the intensity of the reflected light occurs when incident light strikes the fiber optic glass wall and causes backscattering at two frequencies, which are referred to as Stokes and anti-Stokes (Selker et al., 2006). The intensity of backscatter at the anti-Stokes frequency is dependent on the temperature of the cable, thus temperature can be calculated from the ratio of the intensity of the anti-Stokes to Stokes (Grattan and Sun 2000; Ciocca et al., 2012). The precision of this measurement is proportional to the square root of the integration period or the square root of the time in a one-step interval assuming no errors in temperature drift (Selker et al., 2006; Sayde et al., 2010; Ciocca et al., 2012).

FO-DTS systems are portable and can be used for various environmental and hydrologic applications (e.g., Selker et al., 2006; Briggs et al., 2012; Bense et al., 2016). The rugged and compact nature of this tool makes it useful for evaluating soil characteristics in harsh conditions, such as inside a waste rock pile (Broda et al., 2017). FO-DTS systems are often jacketed with braided steel cabling and are resistant to heavy strain and weight but are still able to monitor rapid thermal responses in the surrounding environment.

Resolving volumetric water content with heat

The metal sheath that surrounds fiber optic cables generates heat when electrical current passes between two points on the cable. When the cable is buried in a porous medium (e.g., soil or waste rock), the change in temperature induced by the potential difference in the fiber optic cable is dependent on the thermal properties of the material surrounding the cable, including the porous material and its moisture content. If the thermal properties of the solid components of the porous media do not change with time during measurements, any changes in temperature when electricity is applied should be the result of changes in moisture content in the medium. As air has a very low thermal conductivity and density, it is assumed to have negligible effects on the bulk thermal properties of the medium (de Vries 1963; Kluitenberg 2002).

Several methods have been proposed to calculate the volumetric moisture content from active FO-DTS data based on classic equations in the heat diffusion literature. Carslaw and Jaeger (1959) provide an analytical solution to solve an infinite line heat source problem in a homogenous and isotropic medium using an integrated form of Fourier's law (de Vries 1963; Bristow et al., 1994; Ciocca et al., 2012; Benítez-Buelga et al., 2014). The change in temperature, ΔT, in response to a constant heating strength per unit length of cable, Q (W/m), during a prolonged heating cycle (>10 min) can be expressed as follows (Blackwell 1954; Li et al., 2016):

$$\Delta T(t) = \left(\frac{Q}{4\pi\lambda}\right)\ln(t) + B \tag{2.1}$$

where t is the heating pulse duration (s), Q is the source heating strength (W/m), λ (W/(m·°C)) is the thermal conductivity of the medium, and constant B is a bulk parameter (°C) that functions as the intercept when ΔT is plotted against ln(t). For active FO-DTS moisture analysis, Equation 2.1 is the most common solution for the single probe method in which the fiber optic cable metal sheathing acts as the infinite line source probe with known heating power and duration (Weiss 2003). Fitting temperature data to the cooling phase after the heating cycle has been shown to also work as well for thermally conductive media (see Kluitenberg et al., 1993; Weiss 2003; Ciocca et al., 2012; Benítez-Buelga et al., 2014).

Thermal conductivity and diffusivity can be obtained by fitting a linear regression between the temperature data and the natural logarithm of the heating duration if the integration period is long. The thermal conductivity is inferred from the slope of that regression (i.e., slope = $Q/(4\pi\lambda)$, see Equation 2.1) (Carslaw and Jaeger 1959; Kluitenberg et al., 1993; Bilskie 1994; Bristow et al., 1994; Weiss 2003). After obtaining λ, θ can be calculated using empirical models (i.e., Johansen 1975; Côté and Konrad 2005; Lu et al., 2007) or by calibrating θ–λ relationships with in situ probes (Sayde et al., 2010; Gil-Rodríguez et al., 2013).

A disadvantage of this approach arises when distinguishing small changes (<0.05) in volumetric water content during a short-duration heat pulse (Weiss 2003; Perzlmaier et al., 2004). Ciocca et al. (2012) obtained accurate θ values in wet media with a precision of 0.01–0.035 m3/m3 using a time correction applied to this method. However, to maintain a good relationship in drier media that are less thermally conductive than those considered by Ciocca et al. (2012), longer integration periods are required for the temperature profile to become asymptotic in the thermal response analysis. Dong et al. (2017) demonstrated that such a method results in a weak function of soil moisture by using the cooling phase of the heating response, and that the approach may return implausible values for moisture contents if inefficient electric power is used. As such, this method may be impractical for resolving relatively rapid changes in θ due to water movement.

The dual probe heat method is an alternative approach that resolves volumetric heat capacities as opposed to thermal conductivity. The method is outlined by Campbell et al. (1991), following Carslaw and Jaeger (1959). One probe (i.e., a fiber optic cable) is heated uniformly and the thermal response is measured with a separate cable. The temperature response recorded by the unheated cable is, in part, a function of volumetric moisture content. The temperature rise, ΔT, is a function of the volumetric heat capacity of the material, C (J/(m3·°C)), and the radial distance, r (m), between the heating source and the sensing probe (Carslaw and Jaeger 1959; Campbell et al., 1991; Bristow et al., 1994; Benítez-Buelga et al., 2014):

$$\Delta T = \frac{q}{e\pi r^2 C} \tag{2}$$

where q is the heat input per unit of length (J/m) and e is Euler's constant (i.e., the base of a natural logarithm). For a porous media, C is expressed as a volumetrically weighted arithmetic mean of the heat capacities of the medium constituents (de Vries 1963; Kluitenberg 2002; Benítez-Buelga et al., 2014):

$$C = \rho_b c_s + \rho_w c_w \theta \tag{3}$$

where ρb and ρw are, respectively, the bulk medium and water densities (g/m3); and cs and cw are the specific heat capacities of the solid medium and water, respectively (J/kg·°C). This formulation ignores the very minor influence of air and water vapor on bulk heat capacity and assumes that the pore water is entirely unfrozen.

Equations 2.2 and 2.3 can be combined to infer moisture contents from the temperature rise due to heating. However, a major disadvantage of this method is the need for very accurate probe spacing. Equation 2.3 shows that small changes in radial distance, r, can have large impact on estimations of C, and thereby influence θ estimates. In cases where the medium contains coarse and angular particles, the contact between the fiber optic cable and the medium and the distance between cables may shift during the construction, rendering r inaccurate. Another disadvantage of this approach is that the dry bulk density and heat capacity of the medium must be known. This again can be problematic when the material is heterogeneous and coarse-grained.

Sayde et al. (2010) developed a semi-empirical approach to estimate θ using active FO-DTS. Instead of deriving thermal properties of the soil medium, the heating profile is integrated directly from FO-DTS results and extrapolated from a rating curve to fit dry and saturated conditions using an empirical model. The calculated error associated with this method is less than 0.05 m3/m3 in wet soil (Sayde et al., 2010). The results can be obtained using a cumulative temperature rise over time, T_{cum} (°C s), in the cable:

$$T_{cum} = \int_{t}^{t_0} \Delta T dt \tag{4}$$

where t_0 is the duration of the heating cycle. This method assumes that the integral rise in temperature for a given heating strength is solely controlled by the bulk material properties, so the relationship between T_{cum} and θ holds for a constant heating profile and fiber optic cable specification (Sayde et al., 2010; Gil-Rodríguez et al., 2013). The error associated with the changes in temperature using this method is minimized because the DTS recordings are based directly on measured temperature and do not rely on thermal properties of the material.

Zubelzu et al. (2019) compared potential (i.e., Farfan et al., 2017), exponential (i.e., Gil-Rodríguez et al., 2013), and polynomial (i.e., Benítez-Buelga et al., 2014) Tcum–moisture fitting functions. Their findings suggest that all curves could present a nonGaussian pattern during the heating phase despite high coefficients of determination. To reduce this behaviour, the cumulative temperature profile can be integrated over a long integration period with a low sampling rate. Cable-specific properties account for little of the experimental error due to the rapid increase in temperature, and these properties are obtained with a lower sampling rate during the initial temperature rise (Sayde et al., 2010; Gil-Rodríguez et al., 2013). When a higher sampling rate is used, the input amperage can be decreased so that the maximum temperature is easier to obtain. Dong et al. (2017) showed that this method can yield similar results using higher power during a shorter duration and lower power over a longer integration period. This is useful where input amperage is limited in low-conductivity media. Striegl and Loheide (2012) provided a similar method to obtain temperature token values where the change in temperature is assumed constant and averaged over a period of 380–580 s. The token values were then related to nearby moisture sensor values to generate a temperature–moisture curve that was calibrated to collect soil moisture data.

The relationship between λ and θ for a given system follow a specific shape with a shallow slope at low water contents and steeper slope at higher water contents (i.e., Johansen 1975; Campbell et al., 1991; Lu et al., 2007). The shape of the curve is a function of several specific parameters of the material. This study proposes a modified time cumulation approach to relate thermal conductivity to temperature response to obtain θ. This modified approach combines the usefulness of the Tcum approach (Equation 2.3 and surrounding text) with the theoretical rigor of the Blackwell (1954) approach (Equation 2.1). Integrating Equation 2.1 yields the cumulative temperature change over the heating period

$$T_{cum} = \frac{Q}{4\pi\lambda} t[\ln(t) - 1] + Bt \tag{5}$$

To account for pore and thermal variability, a Kersten number, Ke (Kersten 1949; Johansen 1975; Halloran et al., 2016) is commonly used to normalize λ (W/(m·°C)) to soil-specific dry and saturated values:

$$Ke = \frac{\lambda - \lambda_{dry}}{\lambda_{sat} - \lambda_{dry}} \tag{6}$$

The degree of saturation, Sr, can then be calculated using one of many empirical models found in literature. The Lu et al. (2007) model is used here for its versatility in accurate approximations of thermal conductivity in a wide range of soils:

$$S = (1 - \frac{\ln(Ke)}{\gamma})^{\frac{1}{\gamma - 1.33}} \tag{8}$$

where γ is a soil texture–dependent parameter, with 0.96 and 0.27 as the values for coarse- and fine-textured soils, respectively (Lu et al., 2007). θ is then calculated from the average porosity of the material, *n*:

$$\theta = S_r n \tag{9}$$

2.4. Experimental Setup and Measurements

2.4.1. Column and Helices

The fiber optic cable was wrapped into three helixes held together with plastic rod scaffoldings (Figure 2.1). The helixes had internal radii of 0.15, 0.25, and 0.35 m. The cables were bent into a helical pattern to allow the FO-DTS cable to record temperatures at a vertical resolution of 0.05, 0.03, 0.02 m in the smallest, intermediate, and largest helices, respectively. The fiber optic cable passed through two cold and one warm calibration baths (Figure 2.2).

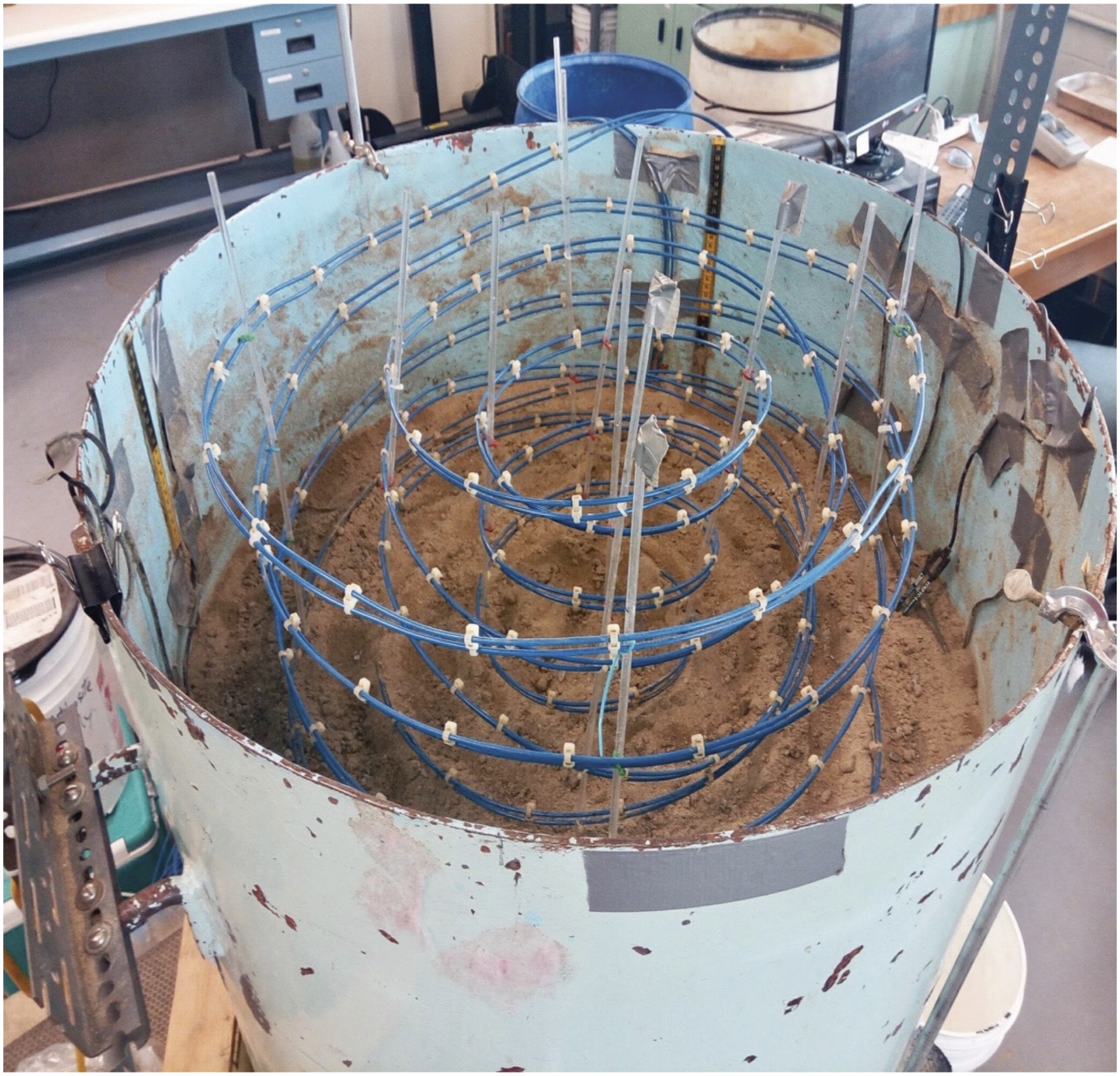

Figure 2.1: Column helices exposed in upper sand layer, prior to emplacement of remaining sand layer. Two adjacent fiber optic cables are tied together 1 cm apart; however, only one cable is used for the experiment.

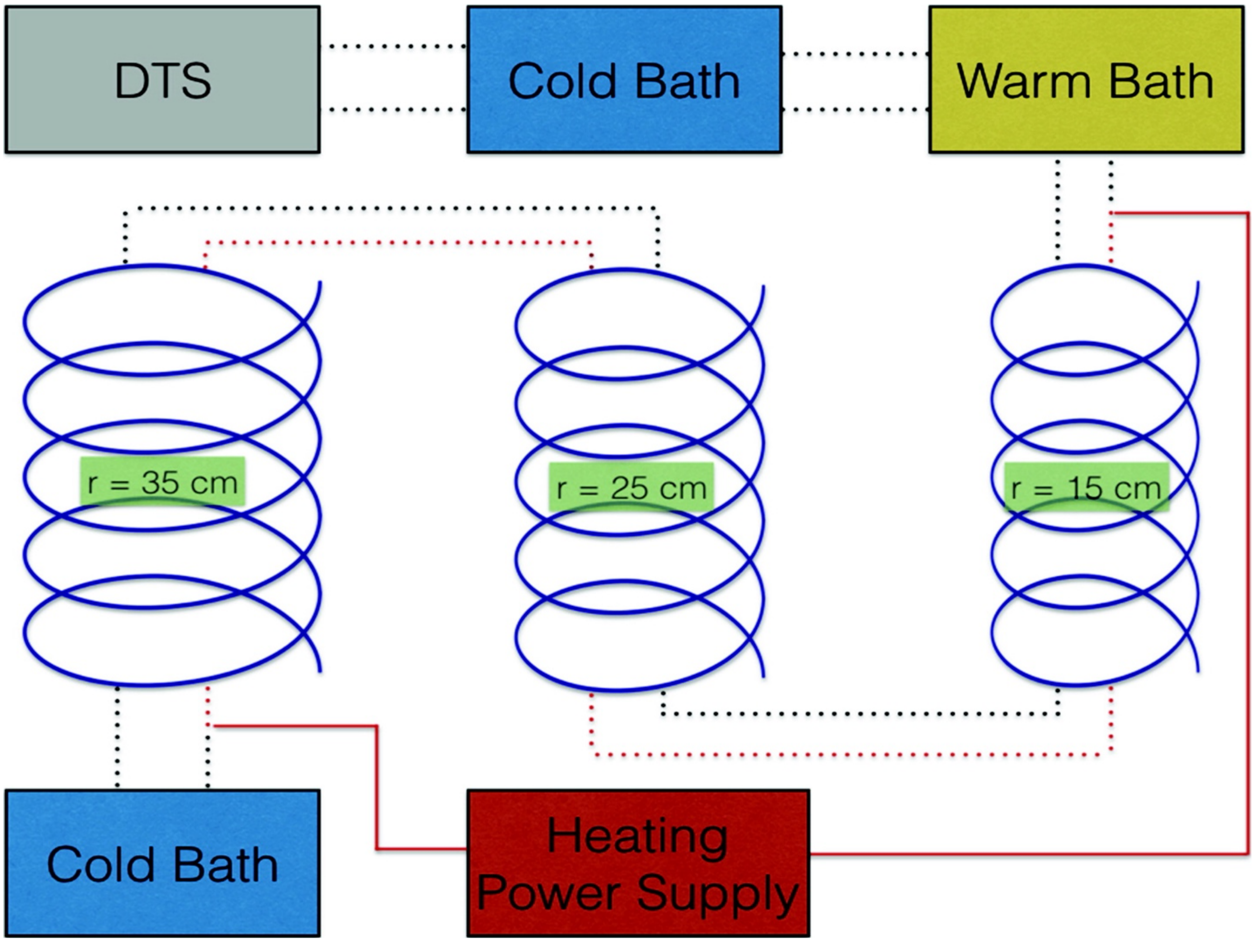

Figure 2.2: Fiber optic cable path (dotted lines continue into helical structures). Red dotted line is heated portion of fiber optic cable through which 15 W/m of power was applied.

The helical coils were placed in a metal cylinder that is 0.80 m in height and has a radius of 0.80 m. The bottom of the cylinder contained a cobble layer overlain by a geotextile to promote drainage without loss of finer particles. The column includes an outflow drain discharged into tipping bucket lysimeters (1 mm/tip) to measure effluent discharge rate. Once the cables were placed in the empty cylinder, 0.50 m of screened anorthosite (<5 mm) was poured into the column (on the geotextile) via spiral deposition to limit particle segregation and compacted layering. A homogenous sand layer (0.20 m thick) was then added on top of the anorthosite using the same deposition method (Figure 2.3). The sand had a maximum grain size of 0.5 mm and is considered a poorly graded fine sand (SP), while the screened anorthosite had a maximum grain size of 10 mm and is considered a well-graded sand with silt and gravel (SW-SM) according to Unified Soil Classification System (USCS; ASTM 2017) classification (anorthosite data from Lévesque 2015).

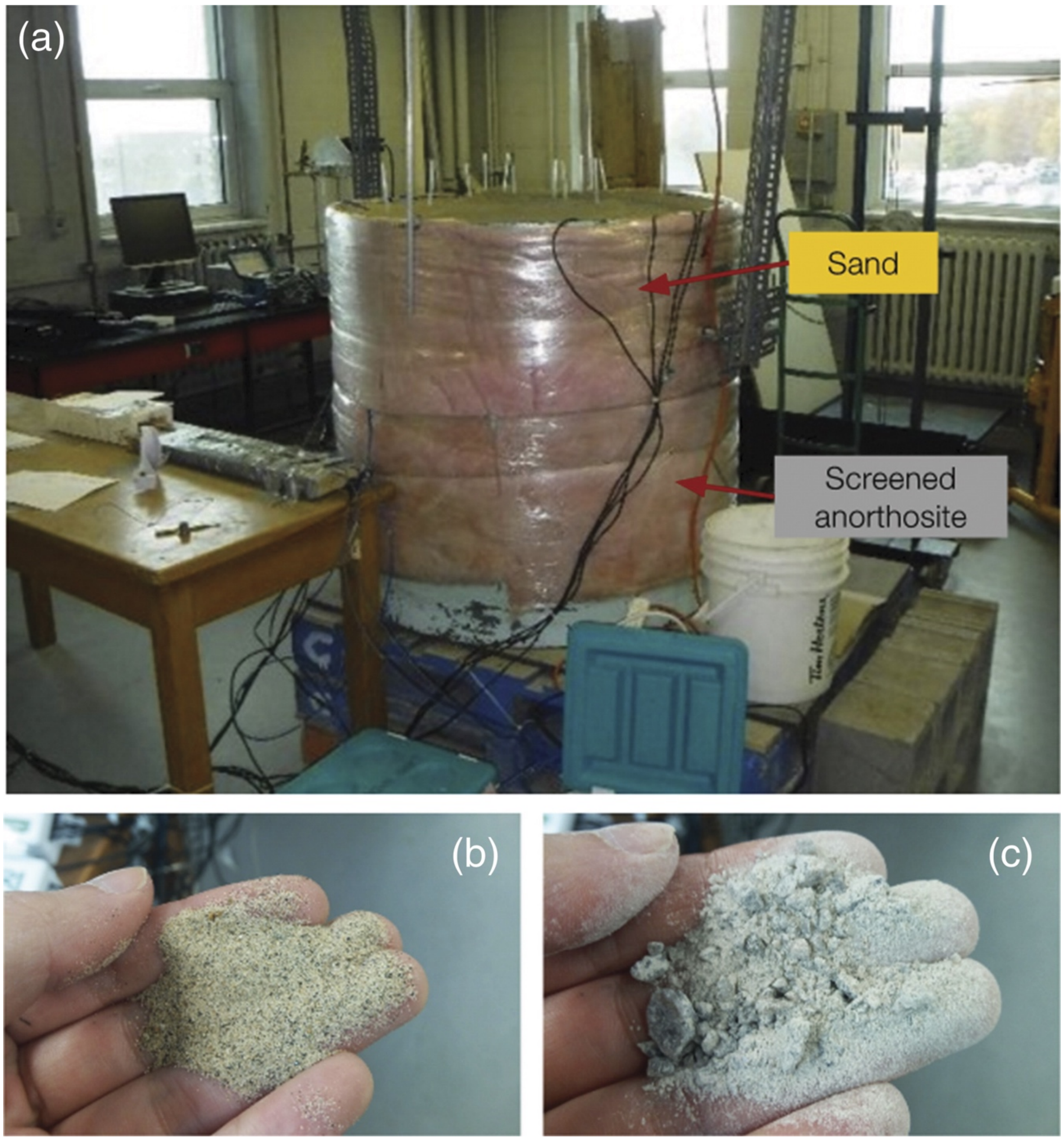

Figure 2.3: (a) Experimental column containing (b) fine sand and (c) coarse screened anorthosite.

The DTS resolves temperature to within ± 1.0 °C in each material using 20 s dual-ended measurements. To improve the accuracy of the FO-DTS measurements, data were corrected for temperature offsets and instrument drift using two reference baths with water at approximately 0 and 40 °C. Van Essen Micro-Diver pressure transducers (±0.1 °C accuracy, 0.01 °C resolution) were placed in the baths to record the calibration temperatures. The warm bath was kept at constant temperature and well-mixed with an aquarium heater, while the cold bath contained a slush mixture.

A sprinkler affixed 40 cm above the top of the column released 2.6 L/min of water during an infiltration test. Care was taken to use a sprinkler nozzle that evenly irrigated the top of the column without water droplets becoming too fine (misty) and to avoid droplets from adhering to and flowing down the rain jacket surrounding the column. Heterogeneity in spatial results within the column may nonetheless be caused by uneven irrigation (see Results section).

2.4.2. Instrumentation

The FO-DTS instrument used in this experiment was an AP Sensing N4388A GeoDTS with a manufacturer spatial resolution of 1.0 m (vertical resolution is higher due to the helixes), sampling interval of 0.5 m, and a minimum data integration time of 20 s in dual-ended measurements. The fiber optic cable was the Brugg BRUsteel LLK-BST 2FG5, which has two fiber optic strands encased within a galvanized steel tube and wrapped with braided steel wire and a waterproof nylon jacket.

Four Decagon EC-5 soil moisture sensors were buried in the sand layer, at 5 and 15 cm depths, and four were buried in the anorthosite waste rock layer, 30 and 50 cm depths, to compare θ results with the DTS and parameter γ values with Lu et al. (2007). The EC-5 sensors have a manufacturer's stated accuracy of ±0.03θ in mineral soil (Decagon 2015). The sensor measures the dielectric constant of the media using the capacitance and frequency of the soil domain.

The probes utilized in the experiment were individually calibrated with material-specific calibration curves. The experiment sensors were calibrated using samples from the column and yielded an accuracy of ±0.06θ in the sand and crushed anorthosite, which revealed that the accuracy of the probes was lower than the manufacturer's stated error. Although the crushed anorthosite is texturally more complex, the EC-5 accuracy in this material was the same as homogenous sand. This suggests that ±0.06θ may be the highest accuracy achievable with the probes used in the experiment.

2.4.3. Calibration and Determination of Protocol Parameters

Endmembers of Tcum were measured independently of the infiltration test. Dry T_{cum} values were obtained before water was added into the column. Dry measurements were taken for 10 cycles to ensure the power supply provided consistent heating under dry conditions. Consecutive measurements were repeated after the infiltration test, at saturation, to ensure the power was sufficient to allow the DTS to record changes in temperature when wet. The material in the column was saturated upwards with a Mariotte bottle to ensure most of the voids were filled with water. Near-saturation conditions were expected using a low hydraulic gradient to ensure that the upward movement of finer particles had negligible influence on homogeneity.

The EC-5 soil moisture sensors essentially measure porosity under saturated conditions, assuming all pores are filled with water. The volumetric water content at saturation measured by the EC-5 sensors was 0.44 and 0.26, respectively, for the sand and anorthosite. Porosity was calculated from column samples and yielded porosity of 0.42 and 0.27, respectively, for the sand

and anorthosite. The obtained γ was 0.26 and 0.92 for the cover sand and (screened) anorthosite, respectively, which is close to the suggested values provided by Lu et al. (2007). The B term in eq. (5) is calculated as the intercept in each heating cycle between ΔT and ln(t).

2.4.4. Active Fiber Optic Measurements

Figure 2.4 presents the vertical temperature profile obtained during a typical heating cycle for a dual-ended FO-DTS configuration, in which the end of the fiber optic cable returns to the DTS and measurements are collected through both ends of this cable. Dual-ended measurements integrate temperature readings averaged from both ends of the cable, decreasing the chance for signal loss in longer fiber optic cables.

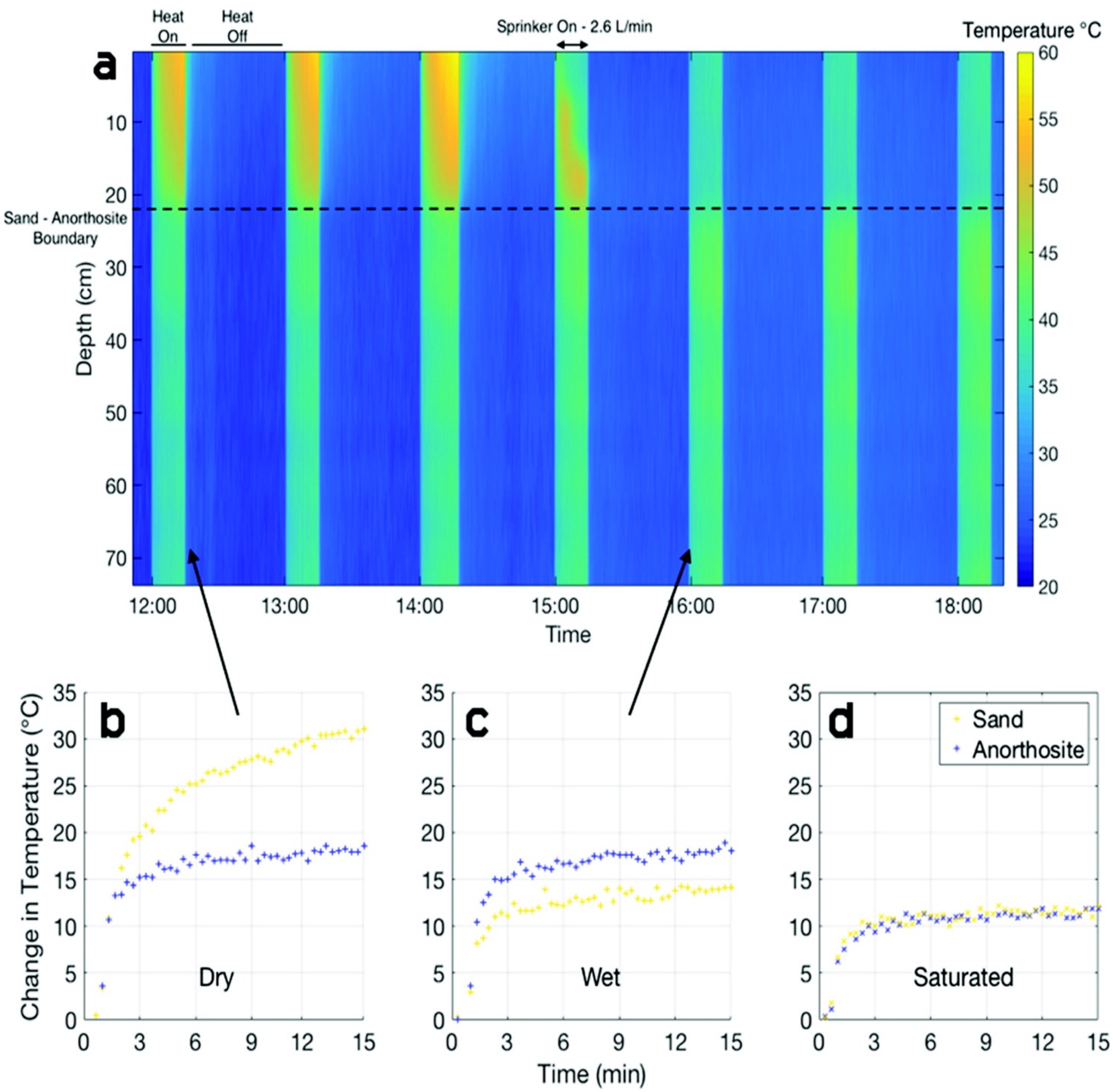

Figure 2.4: (a) Temperature profile along depth of column, as measured in the outer helix through time. Rain infiltration starts at 15:00. Change in temperature due to heating for (b) dry, (c) wet, and (d) saturated conditions in sand and anorthosite, measured in outer helix. (Note: saturated conditions are not represented in Figure 2.4a.)

A heating cycle is 1 h long; for the first 15 min the cable was actively heated by applying an electrical current across the cable followed by 45 min of no heating during which the system cools. A DC power supply with a voltage regulator to maintain 15 W/m was used throughout the heating cycles and adapted to changing resistance in the cable due to heating. The resistance of the cable was 17 Ω at room temperature, and the length of heated cable was 46 m. The power used in this experiment is higher than in previous published studies (Sayde et al., 2010; Striegl and Loheide 2012; Benítez-Buelga et al., 2014) because the temperature response in the thermally low-conductive screened anorthosite was not sufficient at lower electrical power. Higher power settings also enabled measurement of smaller changes at low volumetric soil moisture levels (<0.06%) as the uncertainty in the θ error analysis is inversely proportional to the value of θ (Weiss 2003).

2.5. Results

Fifteen minute heating cycles were performed every hour (Figure 2.4a) for 190 cycles or 7.9 days. The change in temperature during the first cycle is shown in Figure 2.4b. In dry conditions, the sand reached a ΔT of 35 °C during heating, while the anorthosite had a ΔT of 20 °C. The sprinkler was turned on at the start of the fourth cycle for 15 min to apply water to the experimental column Thirty-nine liters of water, equivalent to 19.4 mm of rain, were applied across 15 min to simulate a short, but intense precipitation event. Within 1 h after the onset of infiltration, the temperature of the sand layer decreased by 21 °C (ΔT decrease from 35 to 14 °C) during the heating phase (Figure 2.4c). The anorthosite unit did not exhibit a change in temperature, maintaining a temperature of 45 °C during the infiltration period. When the sand and waste rock were highly saturated, the ΔT of both materials was reduced to 10 °C (Figure 2.4d).

The relationship between T_{cum} and θ assumes that the overall density and texture of the material remain constant. Using the relationship defined by Lu et al. (2007) with specific parameters obtained here (see "Experimental setup and measurements section), the variation of θ with depth within the column was calculated. Figure 2.5 shows 1 week of results after a 15 min wetting test (equivalent to 19.4 mm of rain). The test starts with three heating cycles prior to wetting to establish baseline conditions, and the infiltration event occurs during the fourth heating cycle. Volumetric water content (VWC) increases in the cover sand layer during the fourth cycle in the top 10 cm of the column. During infiltration, the highest θ in the sand was obtained in the interior helix and the lowest θ was in the exterior helix. Once the infiltration event ended, the exterior helix recorded the highest moisture content value post-infiltration in the sand (0.42 m3/m3), while the interior recorded the lowest (0.36 m3/m3). The highest volumetric water content was measured in the lower section of the sand layer following the infiltration test, as expected in a capillary barrier system. There was no corresponding increase in moisture in the anorthosite layer (Figure 2.5).

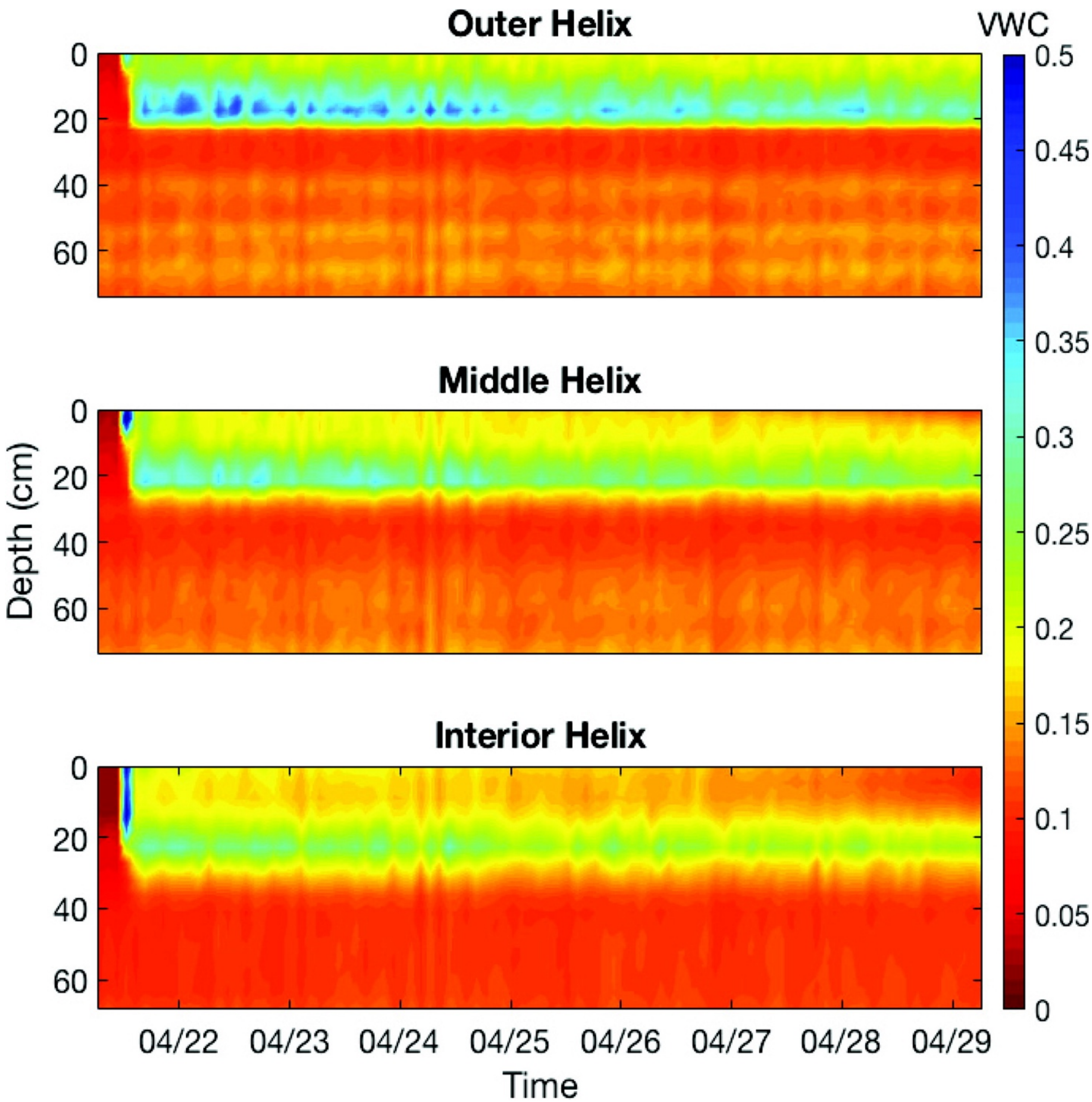

Figure 2.5: Volumetric water content calculated over time from FO-DTS set up in the (35 cm radius, 2 cm resolution), middle (25 cm radius, 3 cm resolution), and interior helix (15 cm radius helix, 5 cm resolution).

Over the course of the week, the value of θ in the upper sand layer decreased slowly, while the θ remained effectively unchanged in the anorthosite unit. By the end of the test, the θ near the interior helix in the upper sand layer approached antecedent residual θ values (0.09 m3/m3). No discharge was recorded from the column's outflow drain over the course of the experiment.

The coefficient of determination, R2, between the active FO-DTS measurements and the EC-5 soil moisture probes in the cover sand layer is 0.90, with a root mean square error (RMSE) of 0.06. The DTS-based measurements are more sensitive to small changes in θ than the four EC-5 soil moisture probes in the sand. For example, the comparison between the DTS and probe values at around θ = 0.20 is poor as changes in DTS readings do not correlate to changes recorded by the moisture probe (Figure 2.6). Higher θ values tend to produce larger variations as the uncertainty in the measurements is proportional to the degree of saturation.

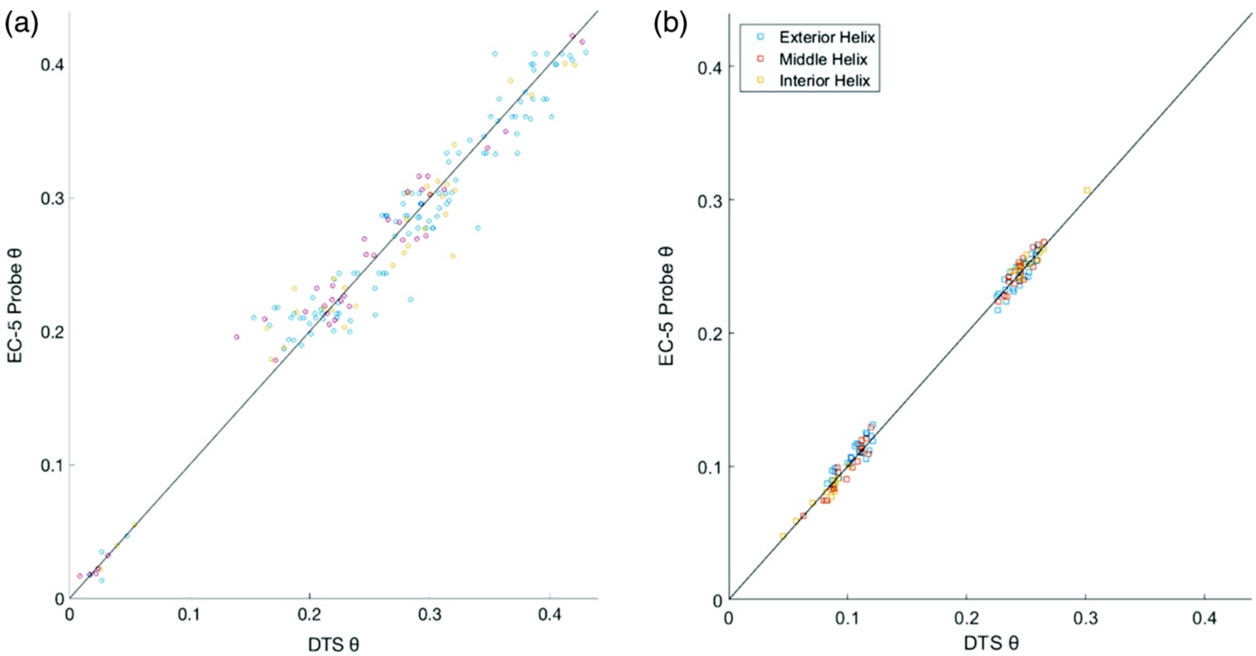

Figure 2.6: Scatterplot comparison of measured moisture, θ, from FO-DTS and EC-5 θ in the (a) sand and (b) anorthosite layer of each helix.

The EC-5 moisture probes recorded θ increases in water content in less than 5 min after the onset of the infiltration event. Quick increases in θ values could not be recorded during the early part of the 15 min infiltration test, so no θ values in the 0.05–0.20 range were observed in the sand layer. The error associated with calculating θ should increase with θ. However, results obtained here indicate that the largest uncertainty exists around 0.20 for this infiltration test (Figure 2.6).

Comparison of volumetric water content values during the infiltration test measured by the active FO-DTS and moisture probes yielded a value of approximately 0.15 and a mean absolute error (MAE) of 0.07 in the anorthosite waste rock. Using both the θ values during the infiltration test and during saturation, a R2 of 0.94 was obtained. It was difficult to assess the accuracy of the active FO-DTS moisture data in the anorthosite layer because there was only a small range of θ values (e.g., 0.10–0.18). During the entirety of the infiltration test, the value of θ in the anorthosite layer remained relatively constant (Figure 2.5), so only dry, slightly wet, and saturated values were obtained for that layer.

2.6. Discussion

The results obtained from the FO-DTS suggest that water was confined to the fine sand layer, which may have been caused by inherent water retention (capillary) capabilities between the sand and anorthosite (Figs. 4 and 5). The post-infiltration water content in the sand did not reduce suction, at the interface between the layers, below the water-entry value of the anorthosite layer. Thirty-nine litres of water was not sufficient to induce drainage into the anorthosite layer in an estimated 47 L void space. More water was not added due to observed ponding on the top of the sand layer at the given infiltration rate. In earlier tests, 52 and 73 L of water were applied to the column in 20 and 30 min, respectively. These tests were disregarded as there was water ponding on the surface of the cover sand unit that flowed out towards the edge of the column. However, the DTS resolved water flowing through the interface from the sand and into the anorthosite. In both cases, water discharged from the outflow drain approximately 35 min after the start of infiltration, but the outflow quantity was too much for the tipping bucket rain gauge to record.

The difference in ΔT of the anorthosite between dry and saturated conditions was only 5–10 °C. This suggests using a high-power output was warranted as less power may not have resolved the difference in dry and saturated conditions in this layer. Figure 2.7 shows a two-dimensional (2D) integration of temperature using all three helices; see Supplementary Material videos S1 and S2 to view temperature changes during the infiltration test.1 Spatial and temporal temperature differences in the sand and anorthosite are easily distinguished; however, it is difficult to quantify the impact of these factors on the irregularities in this figure. Note that the laboratory environment was humid; a drier environment may have produced more pronounced decreases of θ in the upper sand.

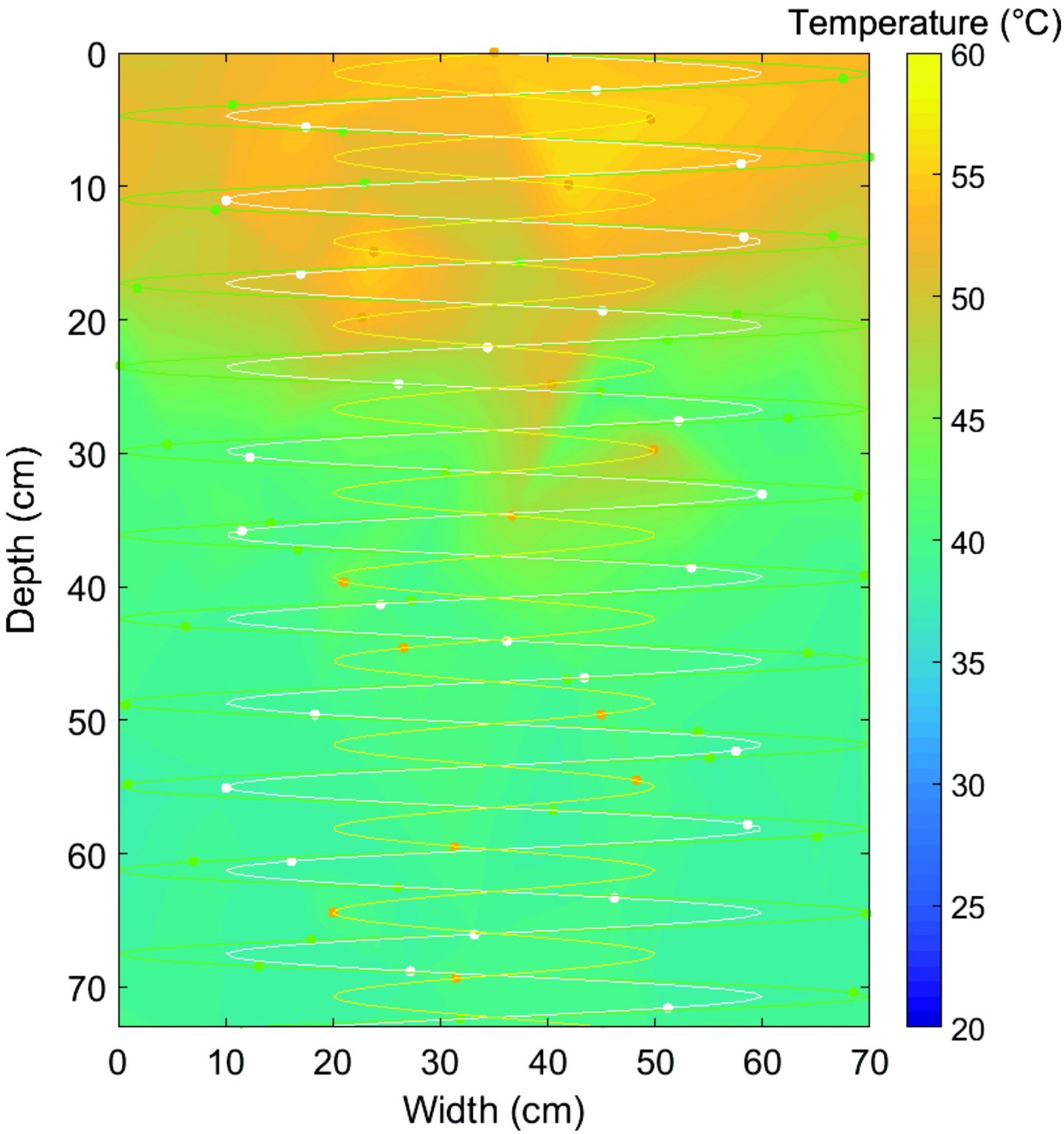

Figure 2.7: Two-dimensional temperature representation of column during dry conditions. Paths of the three helices are outlined with their sampling points (dots are spatially averaged by 1 m).

The results show that much of water appears to enter the near the centre of the column during the start of the infiltration test (Figure 2.5). Water then migrates towards the exterior of the column after the infiltration test as water content was highest in the outer helix. The outer helix had the smallest vertical resolution that resolved finer vertical changes in θ. The unevenness in temperature in the sand layer may have been due to physical phenomena such as local compaction of the material and the amount of contact between the cable and the medium. It could also have been due to interpretive methods when designing the helical data in 2D space. Decisions such as the type of interpolation used (i.e., linear, spline, cubic) for the figure and how the helical path is represented in 2D affect each respective helix (i.e., sine, cosine). The heated profile was not uniform throughout the column. Bends in the helical structure cause changes in DTS intensity ratio, and limitations in temperature resolution due to molecular vibrations causing broadening of Raman peaks, instrument noise due to transmission loss, and local moisture pockets. Sand particulates may have moved into the pore spaces of the anorthosite layer during the compaction and infiltration process. It is likely that the uneven results were caused by a combination of these factors.

The anorthosite layer was not completely dry before the onset of the week-long infiltration test due to conditions from previous experiments. Figure 2.5 shows pronounced horizontal layering in the underlying anorthosite unit (see between depths 22 and 72 cm). This distinctive pattern may be due to density differences in the anorthosite from layering during the construction phase. It could also be due to small unwarranted bends in the helical structure causing interpretive errors during measurement. The spatial resolution of the DTS system is 1 m; a system with a higher resolution might be able to better identify whether this patterning is from bedding or instrument artefact.

Volumetric water content in the anorthosite remained constant throughout the experiment, but not across the helical path (Figure 2.5). This character may be produced by preferential flow paths that carried finer particles in clumps and formed layers resistant to pore water flow.

However, irregularities in the helical path and differences in bulk densities could also contribute to the source of error. The column was filled by means of spiral deposition to minimize the degree of horizontal layering, but given the dimensions of the experiment, such irregularities are inevitable. Although the anorthosite is coarser than the sand, it compared more favourably with the EC-5 sensors than the sand.

Increasing power applied to the cable was effective in reducing error of the measurements (Sayde et al., 2014; Dong et al., 2017). However, although the anorthosite had a much lower thermally conductivity and thus temperature change (ΔT of 20 °C when dry) than the sand (ΔT of 35 °C when dry), it maintained accurate results (Figure 2.6). All three helices exhibited similar temperature and moisture values where the largest helix had the highest spatial resolution (Figure 2.5). However, given the proximity of the outer helix to the metal wall of the column, there may have been interference to the thermal response. The possibility of heat escaping through the sides of the metal enclosure or ambient air affecting readings near the column wall were not significant sources of error for the following reasons:

- Ambient temperatures near the helices were all within 1.0 °C of each other, indicating that there was no significant temperature difference between the column wall and centre.
- Seven centimetres of fiberglass insulation was wrapped around the outer wall of the column to isolate the soil from the outside environment.
- The process to calculate Tcum does not change if the ambient air and soil temperatures remain above 0 °C.

Like previous studies (e.g., Sayde et al., 2010; Ciocca et al., 2012; Gil-Rodríguez et al., 2013; Striegl and Loheide 2012; Dong et al., 2017), the error associated with measuring θ increases with θ magnitude (Figure 2.8). The relationship between Tcum and θ follows an exponential function (eq. (7)) where small changes in Tcum at high θ affect results more than at low θ. A potential source of error may be overheating because the uncertainty along the saturated profile is greater than the dry profile (Figure 2.8). However, if an excess of power is the cause of this error, the result should be proportional to its magnitude, where the error associated with θ should appear largest during dry conditions. Given the mean absolute error of the DTS compared to the EC-5 sensors (RMSE of 0.06 in the sand unit and MAE of 0.07 in the anorthosite unit), the agreement of the results to moisture probes is good. As the moisture sensors measured θ at a single location, the comparison between the sensors and the DTS only exists in eight places within the column (four in the sand and four in the anorthosite layer). The DTS system also has a large spatial average (1 m) that integrates temperature readings from a very large section of soil versus the EC-5's precise measurement area.

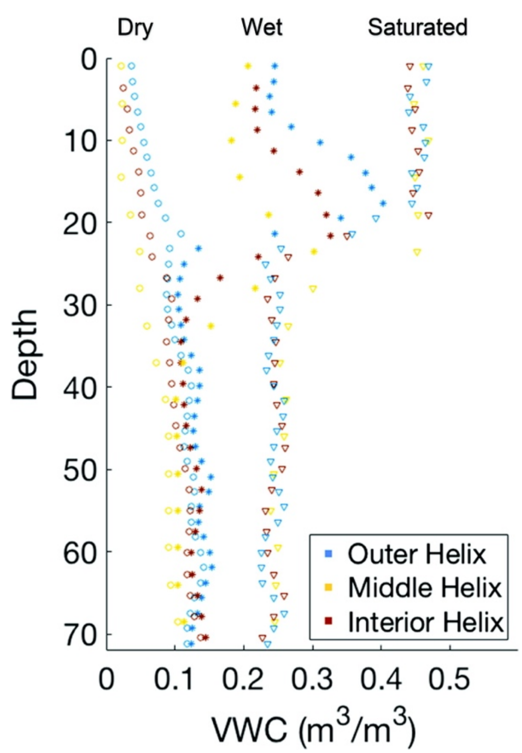

Figure 2.8: Depth versus volumetric water content in each helix during dry (circle), wet (star), and saturated (triangle) conditions.

Note that the EC-5 sensors were not highly accurate for the materials used in the column. In an independent test, two EC-5 sensors (that were used in this experiment) were placed into a small container, with 10 cm spacing. The container was filled with screened anorthosite. The two sensors differ in readings by 0.07θ under dry conditions in anorthosite and 0.05θ in wet conditions; no calibration was imparted on these values for the test. This test provides an assessment of the potential error in sensor measurements. Dong et al. (2017) investigated the relationship between EC-5 readings to measurement depth and orientation. Their study concludes a bias in the EC-5 sensors regarding proximity and orientation to the surface of the medium against DTS readings. The difference in measurement volume between the EC-5 and DTS can also be attributed to contact resistance to the medium, which could allow air to act as an isolating layer that exists in the soil's macropores.

In a water balance exercise for the infiltration period, 39 L of water was estimated to have been infiltrated into the sand layer of the column. The volume of water added during the infiltration test estimated by spatially integrating values obtained by the three helices is 32.6 L. Thus, the FO-DTS method underestimates the amount of infiltrated water by 16% in the column. The capacity of the sand to hold the water, assuming homogenous porosity and no change in pore fraction due to infiltration, is 47.3 L. There are methodological variables that may explain the difference between the infiltration volume and measured soil moisture in the sand layer. The measurement of infiltration water may be overestimated. Small amounts of water may have infiltrated into the anorthosite, although not enough to be observed with the DTS. Furthermore, some water may have flowed preferentially along the column walls or in macropores (without being detected). The interior helix in Figure 2.5 has low vertical resolution and showed that water may have penetrated the sand–anorthosite interface, but it is difficult to quantify the actual impact of the low-resolution reading and seepage.

With each consecutive hourly heating cycle (15 min of active heating followed by 45 min of cooling), the ambient temperature within the column increased by nearly 1 °C. However, the increase in temperature during each heating phase remained constant. Weiss (2003) and Sayde et al. (2010) showed that heating cycles do not affect soil compaction. Similarly, the experiment described herein showed no changes in Tcum between cycles indicating that there were not any significant distortions affecting the soil due to cumulative heating effects.

The purpose of using a long integration period is to decrease error of the initial temperature rise in case it is influenced by characteristics of the cabling (a concern for thicker cables) rather than the soil medium. There are few studies detailing the relationship between hollow gauged wires and resistive heating under electrical load. In past studies, researchers did not integrate the initial phase in case the cable material was a unique variable in the integration step (Striegl and Loheide 2012; Broda et al., 2013). A long integration period reduces this error of the initial temperature rise as it becomes only a small part of the total temperature integration period.

Researchers have noted that using an asymptotic relationship during heating cycles offers the advantage of not needing to account for the effects of the confining fiber optic cable material if the heating cycle is long enough (Ciocca et al., 2012). Tests described herein show that longer integration times are needed for low-conductivity materials (i.e., crushed anorthosite). However, longer integration periods may mask quicker changes in water content that could take place in short periods of time. With the ΔT and power settings used herein, the impact of a long integration period using a time cumulating approach also does not seem to be due to instrument fatigue; however, this should be considered on an individual case basis. The temperature of the fiber optic cable in the experimental medium should be within manufacturer's guidelines, and one should also ensure the temperature at the fiber optic and heating cable connection is also within limits. Temperature readings at the connection may not be accurate, so the data should not be integrated from within the spatial averaging distance of the connection.

Several other models also follow this trend when relating λ and θ (e.g., Johansen 1975; Chung and Horton 1987; Cote and Konrad 2005; Sayde et al., 2014; Barry-Macaulay et al., 2015). The Lu et al. (2007) model relates λ and θ for a wide range of soils; this technique is considered here to be the most appropriate for screened anorthosite as the majority of other models target for quartz sand or loam layers. With the calibrated γ parameters, the methods presented in this study yielded θ with errors of 0.06 in the sand and 0.07 in the anorthosite. Although earlier methods have obtained more precise moisture estimations in different materials (see He et al. (2018) for a record of moisture estimations using DTS), the purpose of this paper is to highlight the potential to use DTS as a standalone measurement tool without using an empirically calibrated soil moisture response curve.

2.7. Recommendations and Conclusion

By using the active FO-DTS method to measure soil moisture, the authors were able to vertically delineate θ during an infiltration test. Over the course of 1 week, the feasibility of using a fiber optic helical network to observe a system that favours the formation of a capillary barrier was tested. This is the first study that does not use an empirically derived calibration curve to obtain soil-specific moisture contents. This is ideal for coarse and heterogenous materials where thermal properties are not easily derived. This active FO-DTS method utilizes the relationships between Tcum and Ke and between Ke and θ in the Lu et al. (2007) model of saturation. Using Tcum offers advantages over other methods that involve thermal properties of the medium, because the precision of this calculation is solely a function of temperature measured from the DTS and does not rely on inferring properties for site-specific soils. All soils follow the same general shape regarding time integration of temperature, Tcum, and θ, so site-specific calibration curves can be adjusted from this general model. Comparison of θ is completed with eight EC-5 probes with satisfactory agreement — R2 value of 0.90 in the sand and 0.94 in the anorthosite. One hour measurements indicate that the sand layer could retain and hold 39 L of infiltration (at 2.6 L/min). The FO-DTS measured a slow drying–evaporation event following the infiltration event in each of the helices.

Results presented herein demonstrate that FO-DTS can continuously resolve changes in θ, even across fine boundaries created by a capillary break. Calibrating active FO-DTS data through Tcum presents some challenges even in laboratory conditions as methods rely on models that fit data to characteristic shapes based on behaviour of a selection of soil types. A prominent difficulty in using this method for consecutive cycles comes from the reliability of the power source. The resistance, and thus power requirement, of a metal wire depend on the temperature of the wire. It is thus necessary that the power supply be maintained regardless of temperature, especially if the experiment will be duplicated in field conditions where the ambient temperature can change diurnally and seasonally. Balancing the right amount of power to the soil properties is a challenge. This challenge was overcome by applying sufficient power to enable the lowest conductivity material (crushed anorthosite) to maintain a constant ΔT of 10 °C. However, this approach was compromised where such power made it difficult for the sand unit to return to its initial ambient temperature following several consecutive heating cycles. Each succeeding heating cycle raised the ambient temperature in the sand by nearly 1 °C. Also, due to the long heating cycles, the methods presented herein were not able to resolve rapid changes in θ in the sand layer as water migrated to the bottom of the sand within 5 min from the onset of infiltration. Future experiments in thermally conductive materials should use shorter heating periods with a higher sampling rate. However, quicker sampling rates decrease the accuracy of the measurement, so integration time and sampling rate should be managed based on the DTS system specification.

Longer tests would also need to account for hysteresis caused by repeated heating and drying cycles. This phenomenon along with soil healing adds to complexity during cable installation. Vibratory compaction methods can cause lateral soil displacement and create low hydraulic conductivity zones (Sourbeer and Loheide 2015). This can be problematic where heavy machinery is commonly used during the construction process for large active DTS experiments. New methods are needed to estimate contact resistance and account for long-term soil moisture calculations in fine materials.

The resistance of the fiber optic cable is an important factor when creating a DTS protocol. Low-resistance cables can be difficult to heat due to their low electrical resistance. In contrast, resistive cables require more voltage to generate and sustain power. Generating constant voltage is critical and a voltage and power regulator may be needed to account for changes in the resistance of the cable during heating cycles. Deciding on the type of fiber optic cable may be difficult if the thermal properties of the medium are not known. Further assessment will be required to understand how hysteresis will affect soil conditions during repeated cycles in field conditions where diurnal and seasonal changes can influence results. A future endeavor for this method is to detect water flux in transient environments. As Tcum is a function of flow around DTS cables, a high-density DTS network could be able to detect rapid changes in high-intensity environments.

This study encourages future field work where FO-DTS can be used as a new tool to observe the internal hydrogeology of potential capillary action, e.g., CCBE waste rock pile covers. The helical design is ideal for laboratory-scale experiments where vertical resolution is more important than horizontal; however, this may not the case for large field experiments. The most important locations to measure moisture in a water-retaining portion of the waste rock pile is immediately above and below the cover. Waste rock piles have a flat rectangular top; thus, an ideal shape to install a fiber optic system would be in a grid pattern for low-powered tests or a stripe-like pattern for high-powered tests. These patterns would ideally be placed above and below the capillary barrier as one single, continuous cable, although two cables may be used if the resistance of the cable is too high due to the length of cable (Martin et al., 2017).

Independent soil moisture values must be taken at the field site if the compaction of the soil differs from laboratory settings. Site-specific Tcum values at dry and saturated conditions may be required as well if the material is not homogenous and well-graded. Saturated values could be taken after a large infiltration event in the field, while dry values can be taken in a controlled area possibly close to the surface of the waste rock pile. This method is also limited to temperatures above 0 °C as below-freezing conditions could create complications regarding melting ice and the latent heat effect.

This experiment preceded a mesoscale test on an experimental waste rock pile. The engineered structure was designed based on numerical simulations to assess control approaches to water drainage in waste rock piles (see Martin et al., 2017). Knowledge of FO-DTS behaviour from this experiment will be transferred to this large field project. More than 1 km of fiber optic cable was installed in the cover, waste, and bottom layer of the pile to observe the efficiency of the flow control layer (FCL). This FCL was inclined at 5° to promote waterflow downslope to the toe of the pile where it is expected to drain. FO-DTS provides insight on the performance of the top FCL by providing information on the water content in the pile to observe if water is diverted to the toe or if it infiltrates into the waste rock.

2.8. Acknowledgements

The authors would like to thank the Research Institute on Mines and Environment (RIME) for their support. Special thanks to Lukas Cheung (McGill University), Noura El-Harrak (Polytechnique Montréal), and Thomas Pabst (Polytechnique Montréal) for their invaluable contributions to this project. This work was funded by the Natural Sciences and Engineering Research Council of Canada (NSERC), Rio Tinto, and partners of RIME.

2.9. References

Aubertin, M., Bussière, B., and Bernier, L. (2002). Environnement et gestion des rejets miniers [CD-ROM] Montréal, Québec, Les Presses Internationales de Polytechnique

Aubertin, M., Fala, O., Bussière, B., Martin, V., Campos, D., Gamache-Rochette, A., Chouteau, M., and Chapuis, R.P. (2002). Analyse des écoulements de l’eau en conditions non saturées dans les haldes à stériles, in Défis et perspectives: Symposium 2002 sur l’Environnement et les Mines, [CD-ROM] Rouyn-Noranda, Canada

Aubertin, M., Cifuentes, E., Apithy, S. A., Bussière, B., Molson, J., and Chapuis, R. P. (2009). Analyses of water diversion along inclined covers with capillary barrier effects. Canadian Geotechnical Journal, 46(10), 1146-1164. doi:10.1139/t09-050

Aubertin, M. (2013). Waste rock disposal to improve the geotechnical and geochemical stability of piles. In Proceedings of the world mining congress, Montreal, Canada.

Barry-Macaulay, D., Bouazza, A., Wang, B., and Singh, R. M. (2015). Evaluation of soil thermal conductivity models. Canadian Geotechnical Journal, 52(11), 1892-1900.

Bense, V. F., Read, T., Bour, O., Borgne, T. L., Coleman, T., Krause, S., Selker, J. S. (2016). Distributed Temperature Sensing as a downhole tool in hydrogeology. Water Resources Research, 52(12), 9259-9273. doi:10.1002/2016wr018869

Benítez-Buelga, J., Sayde, C., Rodríguez-Sinobas, L., and Selker, J. S. (2014). Heated Fiber Optic Distributed Temperature Sensing: A Dual-Probe Heat-Pulse Approach. Vadose Zone Journal, 13(11).

Bilskie, J. R. (1994). Dual probe methods for determining soil thermal properties: Numerical and laboratory study

Bonan, G. B. (2008). Forests and Climate Change: Forcings, Feedbacks, and the Climate Benefits of Forests. Science, 320(5882), 1444-1449. doi:10.1126/science.1155121z

Bristow, K.L., G.J. Kluitenberg, and R. Horton. (1994). Measurement of soil thermal properties with a dual-probe heat-pulse technique. Soil Sci. Soc. Am. J. 58:1288–1294

Briggs, M. A., Lautz, L. K., & McKenzie, J. M. (2012). A comparison of fiber-optic distributed temperature sensing to traditional methods of evaluating groundwater inflow to streams. Hydrological Processes, 26(9), 1277-1290.

Broda, S., Sayde, C., J. Selker, M. Aubertin, and D. Blessent (2013), Using temperature as a tracer for analyzing the response of a capillary barrier in waste rock, paper presented at GeoMontreal 2013: Geosciences for Sustainability, 66th CGS Conference, Montreal, Que.

Bussière, B., Aubertin, M., and Chapuis, R. P. (2003). The behavior of inclined covers used as oxygen barriers. Canadian Geotechnical Journal, 40(3), 512-535. doi:10.1139/t03-001

Campbell, Gaylon & Calissendorff, C and& Williams, J.H.. (1991). Probe for Measuring Soil Specific Heat Using A Heat-Pulse Method. Soil Science Society of America Journal. 55. 291-293.

Carslaw, H. S., and Jaeger, J. C. (1959). Conduction of heat in solids. Oxford: Clarendon Press

Chi, X., Amos, R. T., Stastna, M., Blowes, D. W., Sego, D. C., & Smith, L. (2013). The Diavik Waste Rock Project: Implications of wind-induced gas transport. Applied Geochemistry, 36, 246-255. doi:10.1016/j.apgeochem.2012.10.015

Chung, S.-O., and R. Horton (1987), Soil heat and water flow with a partial surface mulch, Water Resources. Res., 23(12), 2175–2186

Ciocca, F., Lunati, I., Giesen, N. V., and Parlange, M. B. (2012). Heated fiber optic for Distributed Soil-Moisture Measurements: A Lysimeter Experiment. Vadose Zone Journal, 11(4), 0. doi:10.2136/vzj2011.0199

Côté, Jean & Konrad, Jean-Marie. (2005). A generalized thermal conductivity model for soils and construction materials. Canadian Geotechnical Journal. 42. 443-458. 10.1139/t04-106.

de Vries D.A.: Thermal properties of soil. In: Physics of Plant Environment (ed. W.R. van Wijk) North-Holland, Amsterdam, 210-235, 1963

Dobriyal, P., Qureshi, A., Badola, R., and Hussain, S. A. (2012). A review of the methods available for estimating soil moisture and its implications for water resource management. Journal of Hydrology, 458, 110-117.

Dong, J., Agliata, R., Steele-Dunne, S., Hoes, O., Bogaard, T., Greco, R., & van de Giesen, N. (2017). The Impacts of Heating Strategy on Soil Moisture Estimation Using Actively Heated Fiber Optics. Sensors (Basel, Switzerland), 17(9), 2102. http://doi.org/10.3390/s17092102

Fala, O., Aubertin, M., Bussière, B., and Chapuis, R.P . (2002). Analyses numériques des écoulements non saturés dans des haldes à stériles, in 55th Canadian Geotechnical Conference - 3rd Joint International Association of Hydrogeologists-Canadian National Chapter-Canadian Geotechnical Society (IAH-CNC/CGS) Conference: Ground and Water: Theory to Practice, [CD-ROM] Niagara Falls, Canada.

Gil-Rodríguez, M., Rodríguez-Sinobas, L., Benítez-Buelga, J., and Sánchez-Calvo, R. (2013). Application of active heat pulse method with fiber optic temperature sensing for estimation of wetting bulbs and water distribution in drip emitters. Agricultural Water Management, 120, 72-78. doi:10.1016/j.agwat.2012.10.012

Grattan, K. T. V., and Sun, T. (2000). Fiber optic sensor technology: An overview. Sensors and Actuators, A: Physical, 82(1), 40-61. doi:10.1016/S0924-4247(99)00368-4

Halloran, L. J., Rau, G. C., & Andersen, M. S. (2016). Heat as a tracer to quantify processes and properties in the vadose zone: A review. Earth-Science Reviews, 159, 358-373. doi:10.1016/j.earscirev.2016.06.009

Herasymuik, G .M. (1996). Hydrogeology of a sulfide waste rock dump, Master's Thesis in Civil Engineering, University of Saskatchewan, 184 pp

Johansen, O. (1975). Thermal conductivity of soils. Ph.D. thesis. Trondheim, Norway (CRREL Draft Translation 637, 1977) ADA 044002

Kluitenberg, G. J., Ham, J. M., and Bristow, K. L. (1993). Error Analysis of the Heat Pulse Method for Measuring Soil Volumetric Heat Capacity. Soil Science Society of America Journal. Soil Science Society of America, 57(6), 1444.

Kluitenber, G. J. (2002). Thermal Conductivity. In: J.H. Dane and G.C. Topp, editors, Methods of soil analysis. Part 4. Physical methods. SSSA Book Ser. 5. SSSA, Madison WI. P. 1201-1209.

Lu, S., Ren, T., Gong, Y., and Horton, R. (2007). An Improved Model for Predicting Soil Thermal Conductivity from Water Content at Room Temperature. Soil Science Society of America Journal,71(1), 8. doi:10.2136/sssaj2006.0041

Martin V., Aubertin, M., Zhan, J., Bussière, B., and Chapuis, R.P. (2005). An investigation into the hydrological behaviour of exposed and covered waste rock dumps. Society of Manufacturing Engineers Transactions 318: 139-146

Morin, K.A.; Gerencher, E.; Jones; C.E., and Konasewich, D.E., (1991). Critical literature review of acid drainage from waste rock, MEND Report 1.11.1

Newman, L.L., Herasymiuk, G.M., Barbour, S.L., Fredlund, D.G., and Smith, T. (1997). The hydrogeology of waste rock dumps and a mechanism for unsaturated preferential flow, in Proceedings ICARD 1997, pp. 551-564

Perzlmaier, S., Aufleger M., and Conrad, M., (2004), Distributed fiber optic temperature measurements in hydraulic engineering—Prospects of the heat-up method, in Proceedings of the 72nd Annual Meeting—Workshop on Dam Safety Problems and Solutions-Sharing Experience, p. 31, Korean Natl. Comm. on Large Dams, Seoul

Sayde, C., Gregory, C., Gil-Rodriguez, M., Tufillaro, N., Tyler, S., Giesen, N. V., and Selker, J. S. (2010). Feasibility of soil moisture monitoring with heated fiber optics. Water Resources Research, 46(6). doi:10.1029/2009wr007846

Sayde, C., Buelga, J.B., Rodriguez-Sinobas, L., Khoury, L.E., English, M., Giesen, N.V., and Selker, J. S. (2014). Mapping variability of soil water content and flux across 1-1000 m scales using the Actively Heated Fiber Optic method. Water Resources Research, 50(9), 7302-7317. doi:10.1002/2013wr014983

Striegl, A.M. and Loheide II, S.P. (2012), Heated Distributed Temperature Sensing for Field Scale Soil Moisture Monitoring. Ground Water, 50: 340–347. doi:10.1111/j.1745-6584.2012.00928.x

Weiss, J.D. (2003). Using Fiber Optics to Detect Moisture Intrusion into a Landfill Cap Consisting of a Vegetative Soil Barrier. Journal of the Air & Waste Management Association, 53(9), 1130-1148. doi:10.1080/10473289.2003.10466268

Wilson, J.A., Wilson, G W., and Fredlund, D.G. (2000). Numerical modeling of vertical and inclined waste rock layers, in Proceedings of 5th International Conference on Acid Rock Drainage. Denver, Colorado, pp. 257-266

3. Fiber Optic Measurements of Soil Moisture in a Waste Rock Pile

Authors: Robert Wu, Vincent Martin, Jeffrey M. McKenzie, Stefan Broda, Bruno Bussière, John S. Selker, and Michel Aubertin

3.1. Abstract

The design and construction of a waste rock pile influences water infiltration and may promote the production of contaminated mine drainage. The objective of this project is to evaluate the use of an active fiber optic distributed temperature sensing (aFO-DTS) protocol to measure infiltration and soil moisture within a flow control layer capping an experimental waste rock pile. Five hundred meters of fiber optic cable were installed in a waste rock pile that is 70 m long, 10 m wide, and was covered with 0.60 m of fine compacted sand and 0.25 m of non-reactive crushed waste rock. Volumetric water content was assessed by heating the fiber optic cable with 15-minute heat pulses at 15 W/m every 30 minutes. To test the aFO-DTS system 14 mm of recharge was applied to the top surface of the waste rock pile over 4 hours, simulating a major rain event. The average volumetric water content in the FCL increased from 0.10 to 0.24 over the duration of the test. The volumetric water content measured with aFO-DTS in the FCL and waste rock was within ± 0.06 and ± 0.03, respectively, compared with values measured using 96 dielectric soil moisture probes over the same time period. Additional results illustrate how water can be confined within the FCL and monitored through an aFO-DTS protocol serving as a practical means to measure soil moisture at an industrial capacity.

3.2. Introduction

The occurrence and flow of groundwater through unprocessed mine waste stored in waste rock piles is a potential environmental hazard if not properly managed. Waste rock piles are large structures, with heights sometimes exceeding several hundred meters and with areas covering dozens of hectares (Aubertin et al., 2002). Piles have naturally steep side slopes (>37°) and may contain millions of cubic meters of waste rock (McCarter, 1990; Morin et al., 1991; McLemore et al., 2009; Blight, 2010). They should be designed to remain stable indefinitely (Morin et al., 1991). Each waste rock pile configuration has a unique hydrogeologic system that is a function of numerous factors, including the material and machinery available at a specific mine site, dumping techniques, compacted low-permeability layers due to vehicle traffic, particle segregation along the slope of the pile, and the physical characteristics of the materials (Aubertin et al., 2002; Bussière et al., 2003, 2011; Fala et al., 2005).

Environmental contamination from waste rock piles, such as contaminated mine drainage (contaminated neutral drainage, CND, or acid mine drainage, AMD), depends on several factors including the lithology and mineralogy of the waste rock produced, the movement of fluid (air, water and water vapor), and temperature through the pile (Wilson et al., 2000; Lefebvre et al., 2001; Fala et al., 2005, 2006; Molson et al., 2005, Plante et al., 2010). Environments with high precipitation create favorable conditions for oxygen and water to react with waste rock within the pile (Lefebvre et al., 2001). There is now emphasis for the design of waste rock piles to pivot towards mitigating the formation of contaminants. New waste rock pile design can potentially reduce contamination drainage by controlling the movement of water and vapor through the pile (Aubertin et al., 2002, 2005; Fala et al., 2003, 2005, 2006; Broda et al., 2014) during and after the mining operation.

Controlling water infiltration into waste rock piles could be achieved, in principle, by constructing a soil cover system on the pile at the end of surface deposition (Morin et al., 1991; Zhan et al., 2000; Bussière et al., 2003; MEND 2004; Martin et al., 2006; INAP, 2017). It is also possible to use an alternative construction method for the entire pile, based on the addition of inclined flow control layers (FCL) to prevent fluid percolation into the reactive waste work (Aubertin et al., 2002; Fala et al., 2003). The FCL can be constructed with a sandy soil or with non-reactive waste rock crushed to relatively fine-grained texture and compacted on each raise and bench of the waste rock pile. The compacted surfaces are inclined towards the edge of the pile to help promote runoff and limit surface recharge into the waste rock pile interior. The FCL material must have a specific particle-size distribution to induce a significant hydrogeological property contrast with the coarse waste rock underneath to divert water laterally. Water flows in the finer granular layer under unsaturated conditions due to the capillary barrier effect that develops at the interface with the underlying coarse waste rock (Aubertin et al., 2002, 2005, 2009; Aubertin, 2013; Martin et al., 2005, 2017). In an inclined system, water will move along the interface until suction reaches at the interface the water entry value of the waste rock located below. In the inclined FCL, water will remain in the FCL until the capillary forces (i.e suction) is reduced to the water entry value of the underlying waste rock. Finer grained material has high retention capacity, mitigating against percolation flow into the waste rock layer and maximizing runoff and lateral flow within the moisture retaining layer because of the waste rock low hydraulic conductivity under low VWC and S_r (degree of saturation) values (Aubertin et al., 2009). Water accumulates at the FCL and waste rock interface until surface tension reaches the water entry value of the waste rock. This pressure corresponds to the residual water content of the waste rock. Once water moves across the interface, it progressively increases the VWC and unsaturated hydraulic conductivity of the waste rock. Water will then drain into the waste rock layer beyond the lateral diversion length, at the Down-Dip limit (DDL). This is the capacity of the FCL to control water infiltration before being reduced significantly (Aubertin et al., 2009).

This will reduce the effectiveness of the capillary barrier and allow downward flow into the waste rock pile.

While new waste rock pile with FCL and cover designs open the possibility for mitigating environmental damage, it is important to measure and assess their effectiveness. Monitoring the waste rock, FCL and surface cover through time to understand how fluids move through the material is a challenge. Traditional monitoring methods (e.g. soil moisture probes) provide a low-spatial-density monitoring network (Vereecken et al., 2008). The installation of in-situ probes is difficult because the grain size distribution of waste rock is widely graded and includes particles ranging from clay to boulder fractions, with sand and gravel fractions dominating (Barbour et al., 2001, Nichol, 2002, Aubertin 2013, Martin et al., 2017). The primary challenge is obtaining spatially representative data from spot measurements provided by individual probes. For instance, large pore spaces between the coarser grains may result in loss of contact between the material and the probe, which s can reduce the accuracy or negate the effectiveness of in-situ sensors. Better monitoring methods are required in order to acquire distributed data that is relevant at the site scale, given the coarse and heterogeneous nature of waste rock materials.

Fiber optic distributed temperature sensing (FO-DTS) provides the potential to measure soil moisture spatially at a scale relevant for a waste rock pile (with an FCL) and overcome the limitations of point soil moisture sensors. Fiber optic distributed temperature sensing (FO-DTS) allows for temperature measurements along a fiber optic cable utilizing Raman backscattering (Selker, 2006). A change in intensity occurs when incident light strikes the fiber optic glass wall, which causes Raman backscattering at two frequencies, referred to as Stokes and anti-Stokes. The anti-Stoke intensity is dependent on the ambient temperature where the light is reflected, and thus temperature can be calculated from the ratio of anti-Stokes to Stokes peak intensity (Selker et al., 2006). The error on this technique follows the law of large numbers whereby the noise level of the anti-Stoke intensity is inversely proportional to the sampling interval (Sayde et al., 2010, 2014). The intensity of light follows a Gaussian distribution with its standard deviation inversely proportional to the square root of the intensity (van de Giesen et al., 2012). Temperatures measured using FO-DTS can be used to assess the moisture conditions that exist immediately adjacent to the buried cable (e.g. Briggs et al., 2012).

The active FO-DTS (aFO-DTS) method provides an indirect measure of the soil moisture (volumetric water content, VWC). The approach is based on applying an electrical current across the metal casing of a fiber optic to induce temperature changes in the casing and surrounding medium. By measuring the temperature response, soil moisture can be calculated (see Methods Section). Active FO-DTS methods provide an advantage over point measurement systems for soil moisture, as measurements can be made along the fiber optic cable every 1.0 m or less (depending on the technical capabilities of the system).

The first presentation of the use (with strengths and limitations) of active FO-DTS at an industrial capacity was a field-scale detection of dry, wet, and saturated soil in a landfill liner (Weiss, 2003). This pioneering work suggested that volumetric water content can be inferred from a heated cable using the classical probe method described by Carslaw and Jager (1959). Several publications have since proposed empirically derived calibration curves to infer VWC estimates from the thermal properties of the soil around the cable (e.g. Sayde et al., 2010, Ciocca et al., 2012, Benitez-Buelga et al., 2015). Talon et al. (2013) applied DTS to a mine reclamation soil cover to investigate the spatial and temporal scale of variations within the cover layer and revealed heterogeneity in spatial differences using this technique.

While focused on an applied mine site, results and protocol development have broader applications, particularly for precision and industrial agriculture (e.g. vineyards and crop-fields). The distributed nature of aFO-DTS can allow farmers to observe heterogeneity in precipitation wetting and drying rate patterns in soil at high spatial resolutions, possibly providing them the comprehensive information to adjust crop management at a more localized scale and shorter timescale. To date, there is no peer-reviewed literature detailing the use of aFO-DTS to measure VWC in soils at field scale that we are aware of. We believe the proposed protocol highlighted in this paper has potential to be utilized in other commercial capacities as well as in research focused on recharge, soil science, and other cases with designed and natural surfaces.

The authors previously tested the applicability of active FO-DTS with a lab scale column experiment (see Wu et al., 2020). The lab experiment consisted of a column of screened waste rock (< 10 mm diam.) overlain with a sand layer (< 5 mm diam.) in a 400 litre container. It served as a small-scale experiment for the feasibility of using fiber optic cables to detect changes in VWC in a layered system. The measurement protocol in the experiment inferred VWC at 2 cm vertical resolution through the column and the results correlated closely with point measurements of soil moisture (R^2 of 0.90 and 0.94 for the sand and screened waste rock respectively). Results from this study encouraged the placement of fiber optic cable at field scale capacity.

An experimental waste rock pile was built at the Lac Tio Mine in Eastern Quebec with a cover system that acts as an FCL (Martin et al., 2017). The purpose of the experimental waste rock pile was to evaluate the performance of the FCL in preventing moisture drainage into the waste rock. This paper presents the experimental investigation with key results and discusses the feasibility and accuracy of utilizing active FO-DTS technique to assess the VWC distribution within a constructed waste rock pile. To the knowledge of the authors, it is one of the first attempt to assess in situ water movement into a layered waste rock pile.

3.3. Study Area and Experimental Waste Rock Pile

The Lac Tio mine is located ~40 km north of Havre-Saint-Pierre, Quebec, Canada. The average local annual air temperature is 1 °C, and the average annual total precipitation is 1007 mm, with 226 cm of snow-water-equivalent (Climate Change Canada, 2019). The open pit mine, which has been operational since the 1950s, extracts a hemo-ilmenite deposit producing iron and titanium. It has generated 72 Mt of low-grade ilmenite and anorthosite waste rock deposited in surface waste rock piles (Martin et al., 2017). Trace sulphides and nickel exist in the ilmenite while the anorthosite is predominantly non-reactive (Plante 2010, 2014, Poaty, 2018). The waste rock effluent pH is near neutral and nickel concentrations are sometimes higher than local regulation criteria indicating the potential for contaminated neutral drainage, CND. Geochemical analyses showed that the oxidation of Lac Tio hemo-ilmenite can result in leaching elemental nickel into the pile effluent (Plante et al., 2014).

Construction of the experimental waste rock pile to investigate the effectiveness of a surface FCL began in 2014 on the Lac Tio mine site (Martin et al., 2017). The experimental waste rock pile is 70 m long, the top of the pile is 10 m wide, and the base of the pile is 35 m wide (Figure 3.1). The top surface of the pile is covered with a 0.85 m thick flow control cover layer (FCL) inclined at 5% to promote lateral drainage. Broda et al. (2014) estimated using unsaturated numerical modelling that a fine-grained FCL layer inclined at 5% could decrease infiltration into the waste rock by up to 90% and divert most of the surface recharge to the edge of the pile. The waste pile is separated into a reactive core containing predominantly hemo-ilmenite and a non-reactive exterior of predominately anorthosite. The 0.85 m FCL is constructed with sand layer overlain by crushed anorthosite. The sand, brought from a nearby quarry in Havre-Saint-Pierre, is a well-graded sand classified as SW-SP according to the Unified Soil Classification System (Bréard Lanoix et al., 2017, 2020). The anorthosite was crushed onsite and has a clean sand (SP-SW) classification (Martin et al., 2017). The porosity, measured with a Troxler 3440 nuclear density probe, is 0.30 in the FCL sand and 0.26 in the crushed anorthosite (Bréard Lanoix et al., 2020). The porosity of the ilmenite and anorthosite waste rock is assumed to be 0.25 (Peregoedova et al., 2013). The saturated hydraulic conductivity measured using double ring infiltrometers is between 2×10^{-6} m/s and 2×10^{-5} m/s for the sand and assumed to be similar for the crushed anorthosite (Bréard Lanoix et al., 2020). More information on the design, construction, and monitoring results of the Tio experimental waste rock pile can be found in Martin et al. (2017), Dimech et al. (2017), Dubuc (2018) and Bréard Lanoix et al. (2020).

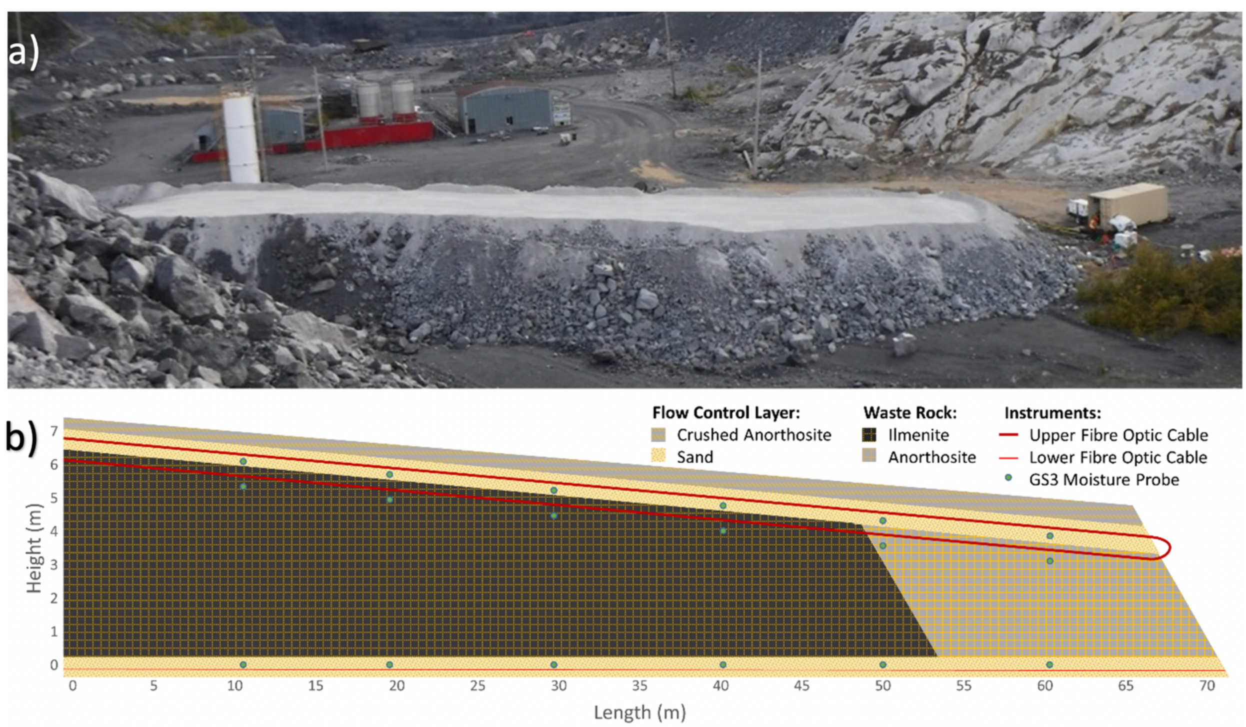

Figure 3.1: a) Photograph of the experimental waste rock pile at the Tio Mine. b) Longitudinal cross-section of the experimental waste rock pile showing the design of the flow control layer,

the location of the fiber optic cable used to measure moisture content, and the waste rock below the FCL.

3.4. Materials and Methods

3.4.1. Active FO-DTS

A total of 1300 m of fiber optic cable was deployed in the FCL (sand and upper crushed waste rock layers) and within the waste rock. The cable, placed 0.5 m above and below the FCL/waste rock interface, is 0.7 cm in thickness. This cable consists of optical fibers encased in a galvanized steel tube surrounded with steel braids and bounded with a polyurethane sheath. It spanned the 70 m length of the pile 8 times (Figure 3.2). The cable was laid 40 cm from the top and bottom of the waste rock and FCL sand layers respectively. The material was compacted around the cable using a vibratory plate compactor. The cable passes through containers with temperature sensors to correct for temperature drifts and to improve precision in the FO-DTS data. The containers are filled with insultation foam and ice water for the warm and cold baths respectively. The containers are repurposed commercial chest freezers, chosen for their large size and insulation. An AP Sensing N4388A GeoDTS was utilized for the active FO-DTS protocol in this experiment. The spatial resolution is 1.0 m, with a sampling interval of 0.5 m, and a minimum dual-ended measurement interval time of 20 s. Raw DTS data was transferred and parsed through a MATLAB function. The function performs a transit correction of the temperature value to the bath temperatures.

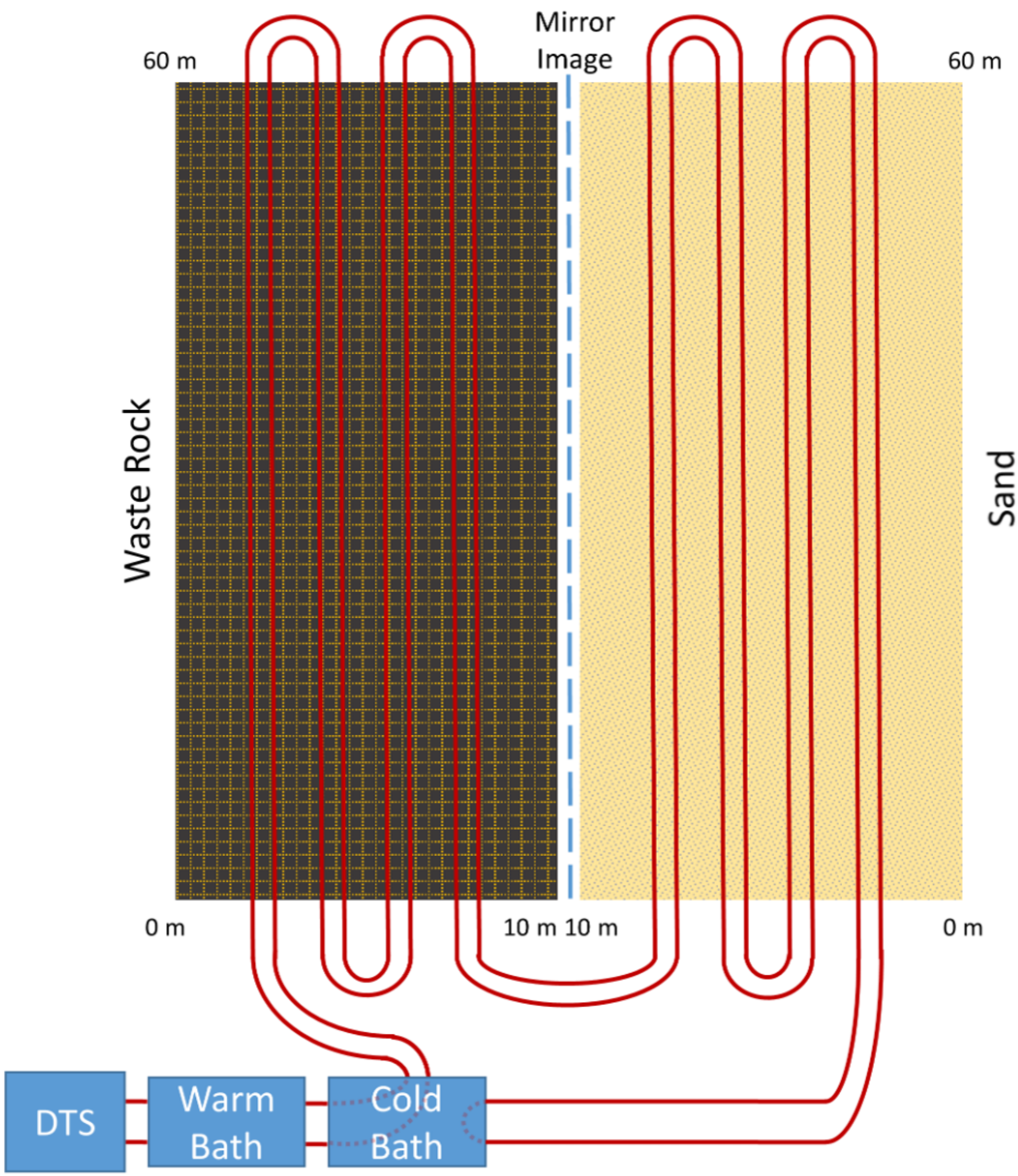

Figure 3.2: Transverse map sectional view of the fiber optic cable distribution within the experimental setup. The sand (Flow Control) layer lies directly above the waste rock.

Heating of the fiber optic cable was performed with a Control Concepts Fusion SCR power controller which delivered 5.6 kW of power across 537 m of the 1300 m cable buried in the FCL sand cover and waste rock layer. This power supply was chosen for its ability to maintain constant power in response to changing resistance in the cable caused by the heating protocol. A 15 kW Kubota SQ1210 generator supplied power to the controller. This generator has a current rating of 85 A and 45 continuous hour fuel consumption. The protocol applied 7.8 kW - 65 A, 120 V at ambient air temperature to maximize joule heating for power efficiency (see Discussion). This power combination is needed to heat the cable at least 10 °C under saturated conditions for the given length and resistance of the cable. A Raspberry Pi 3 micro-computer controlled an OMRON Electronics G9EA-1-CA-DC12 solid-state relay to cycle the heating protocol of the power controller. The protocol involved a 15-minute heating every hour, with 136 cycles over 6 days. The water infiltration test (see below) started several hours after the first heating cycle.

3.4.2. Soil Moisture Probe

Decagon GS3 VWC dielectric probes (Meter, 2016) collected data concurrently in the FCL and upper waste rock layer (Figure 3.1). The GS3 measures the polarity of the medium induced by a weak charge and measures the dielectric permittivity of the medium (Topp et al., 1980). The volumetric water content (VWC) can then be obtained from the calibration on specific samples (Ullrich and Bechtold, 2018). The probes were placed every 10 m along the length of the pile within the FCL and waste rock. The probes measured volumetric water content in the experimental pile every 15 minutes with Decagon EM50 dataloggers. Precision of the GS3 probes is ± 0,03 (Meter, 2016) and the soil specific calibration was the measured value less 0.16 and 0 for the sand and waste rock respectively (Dubuc, 2018).

3.4.3. Infiltration Test

To better understand water flows in to the FCL and the underlying waste rock pile under heavy precipitation, a water truck with a horizontal spray system was used to apply water onto the surface of the experimental waste rock pile (Figure 3.3). An estimated 17 m^3 of water was applied on the pile over a period of 4 hours to simulate a large precipitation event. Due to the mine site shift schedule, the spraying truck ran for 2 hours and 17 minutes followed by a 48 minute break, before a second run of 57 minutes. Each pass of the truck was driven at 3 to 5-minute intervals to minimize surface runoff. The amount of water applied on the FCL was estimated to 38 mm of total recharge during the course of the 4 hour infiltration test (i.e. 9.5mm/hour). This amount of water is quite typical for a heavy rain event in the Havre-Saint-Pierre region of Quebec.

Figure 3.3: Artificial precipitation was applied with a water truck to simulate short duration, large volume precipitation events.

3.4.4. Inferring VWC from FO-DTS Measurements

Our calculation of soil moisture follows the methodology presented by Wu et al. (2020) in determining VWC from active FO-DTS measurements. By applying electrical current to the cable during a specified period, the VWC of the cable can be inferred from the resulting change in temperature. When a current is applied across the metal casing surrounding the fiber optic cable, the cable heats up during this time period (Sayde et al., 2010) due to the inherent electrical resistance of the cable:

$$T_{cum} = \int_0^{t_0} \Delta T dt \tag{1}$$

where T is the temperature at time t (s), and T_{cum} (°C s) is the cumulative heat up cycle from period 0 to t_0 (s).

Benitez-Buelga et al. (2016) presents a similar method to relate thermal conductivity to change in temperature over time. This approach integrates the natural log time during the heat up period as an algebraic relationship to the thermal conductivity of the medium. The rise in temperature, and therefore, T_{cum} can be expressed as a function of thermal conductivity, which is in part a function of soil moisture (Wu et al., 2020):

$$T_{cum} = \frac{Qt}{4\pi\lambda_k}[ln(t) - 1] + Bt \tag{2}$$

where Q is the source heating strength (W/m), t is the heating pulse duration (s), and λ (W/(m °C)) is the thermal conductivity of the medium, and constant B is the bulk parameter of the soil texture (°C). The thermal conductivity is influenced by the VWC of the material. For example, a dry soil would cause the cable to rise to a higher temperature (compared to a saturated soil) since water has a higher thermal conductivity compared to dry media (800 J/kg °C and 1632 J/kg °C for dry and saturated sand respectively).

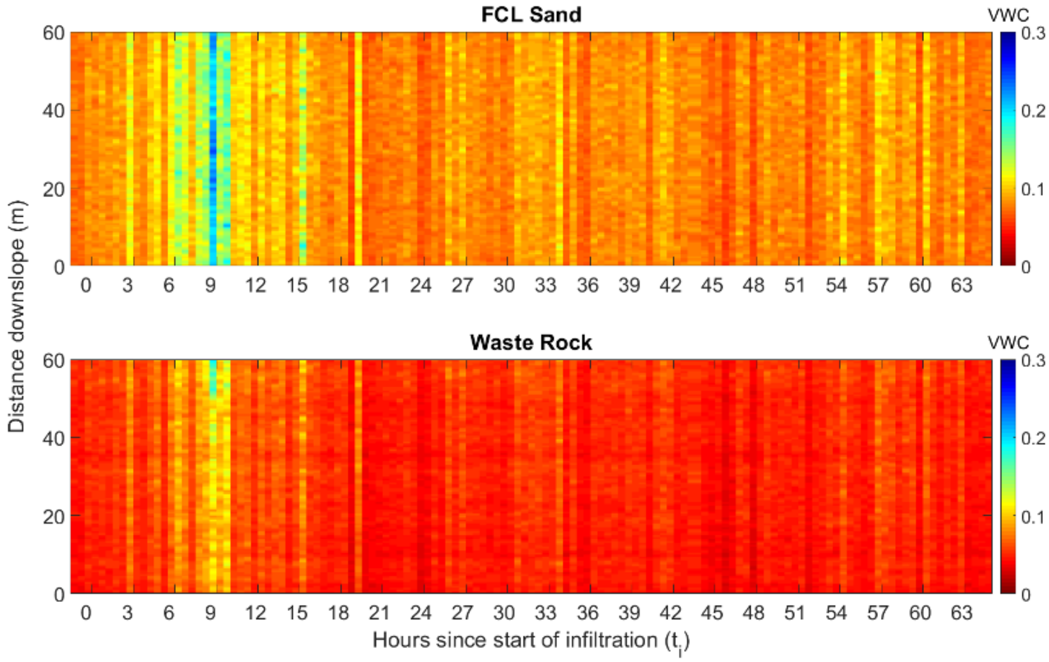

Figure 3.4: Volumetric water content in the Flow Control (sand) Layer and waste rock underneath after the start of the infiltration test; the values are averaged from the four adjacent pairs of cable. The longitudinal dimension of the experimental waste rock pile is represented on the y-axis.

Parameter λ_k is the Kersten number (Kersten, 1949; Johansen, 1975; Halloran et al., 2016) normalized to the thermal conductivity of the medium when it is dry λ_{dry} and saturated λ_{sat}:

$$\lambda_k = \frac{\lambda - \lambda_{dry}}{\lambda_{sat} - \lambda_{dry}} \tag{3}$$

It is assumed here that the change in moisture content in the medium is the only cause for the variation in the rate of temperature rise during a heating cycle. If the heat up values are known for the medium under dry and saturated conditions, a numerical or analytical model can be applied to infer the degree of saturation. The Lu et al. (2017) equation was used in this project:

$$S_r = [1 - \frac{ln(\lambda_k)}{\gamma}]^{\frac{1}{\gamma - 1.33}} \tag{4}$$

where γ is a soil texture dependent parameter. The volumetric water content (θ or VWC) can then be calculated from the porosity, n (0.30 and 0.26 for the FCL and waste rock respectively. This equation is applied to each measurement point along the cable.

$$\theta = S_r \times n \tag{5}$$

3.5. Results

The four adjacent FO-DTS cables detected similar VWC values along the width of the pile in the FCL sand and waste rock layers during the infiltration period. The measured VWC difference between the four cables in the FCL were small: i.e. maximum difference of the VWC of 0.06, average difference of 0.02. The average VWC of the four cables combined in each layer is represented in Figure 2.4. Each color plot in the figure represents the average VWC each hour since the start of the infiltration test (i.e. the first pass of the watering truck). Distance from the head to the toe of the pile is represented by the y-axis.

Similar values between the four cables in the FCL were expected as the saturated hydraulic conductivity of the crushed anorthosite and sand is close to 10^{-6} m/s (Bréard Lanoix et al., 2020). The estimated time for water to reach the bottom of the FCL is at about 10 hours considering this same value of the saturated vertical hydraulic conductivity for both materials (i.e. 10^{-6} m/s for anorthosite and sand).

The FO-DTS reading indicated that the majority of water appeared in the FCL sand layer approximately 8 hours after the start of the infiltration test (Figure 3.4). Highest VWC values along the cables appears at location between 20 m and 35 m, 8 hours into the test, at variably saturated levels. Drainage into the waste rock during the same period indicated that the vast majority of water flowed sideways, towards the edge of the pile. The average FCL VWC was 0.07 ± 0.01 at the start of the infiltration test, and 0.12 ± 0.06 12 hours after the start of the infiltration test.

The statistical distribution of VWC in the FCL is represented in Figure 3.5. The distribution appears gaussian before the start of the infiltration test (Figure 3.5a). Homogenous VWC was also measured widthwise across the pile (with $P < 0.05$, where P is the calculated probability). This normal distribution indicates that there are minimal differences between VWC across the four cables during pre-infiltration period. The distribution of VWC became negatively skewed twelve hours after infiltration started at t_i (Figure 3.5b). The skewness is also represented in Figure 3.6c where higher VWC exist in the second, third, and fifth quintans at t_i+12h. However, the widthwise distribution of water remains uniform.

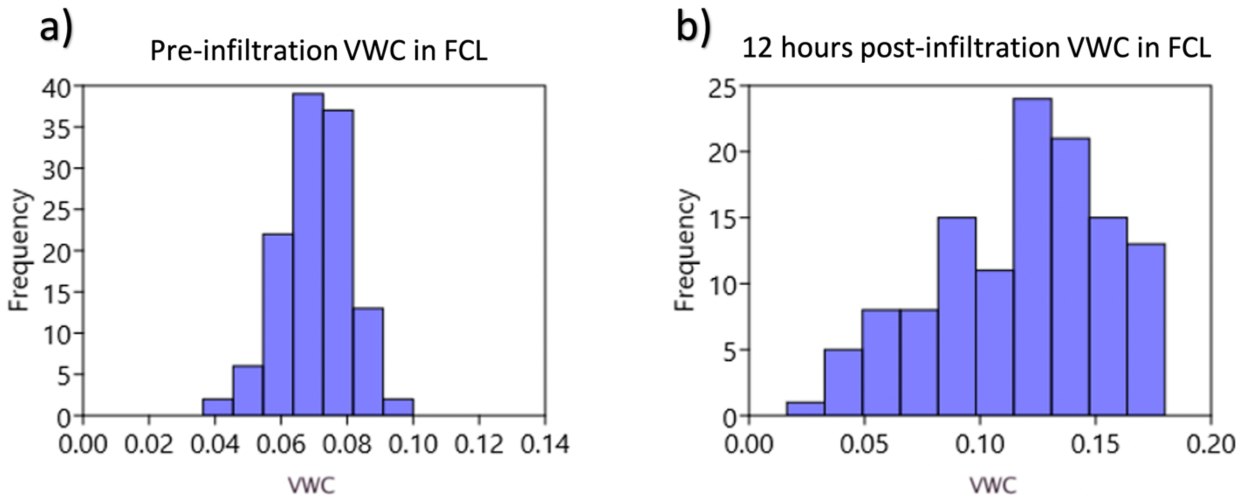

Figure 3.5: Distribution of volumetric water content in the flow control (sand) layer before (pre) and after (post-) the infiltration test.

Distribution of VWC at select times is shown in Figure 3.6. The average downslope VWC is represented for each FCL and waste rock sublayer. At the start of the infiltration test, t_i, the DTS measures VWC of 0.10 and 0.05 averaged across the length of the pile in the FCL and waste rock layers respectively. Following four hours of artificial infiltration, the VWC in the FCL and waste rock layers increased to 0.11-0.18 and near 0.08 in the waste rock beneath. Eight hours following the beginning of infiltration, the FCL reached near saturation between 20-35 m and 55m downslope. Other areas in the FCL are above 0.20 for the VWC. Volumetric water content in the waste rock peaks at a location near 55 m downslope with increases in VWC also observed between 20-35 m to a lower degree.

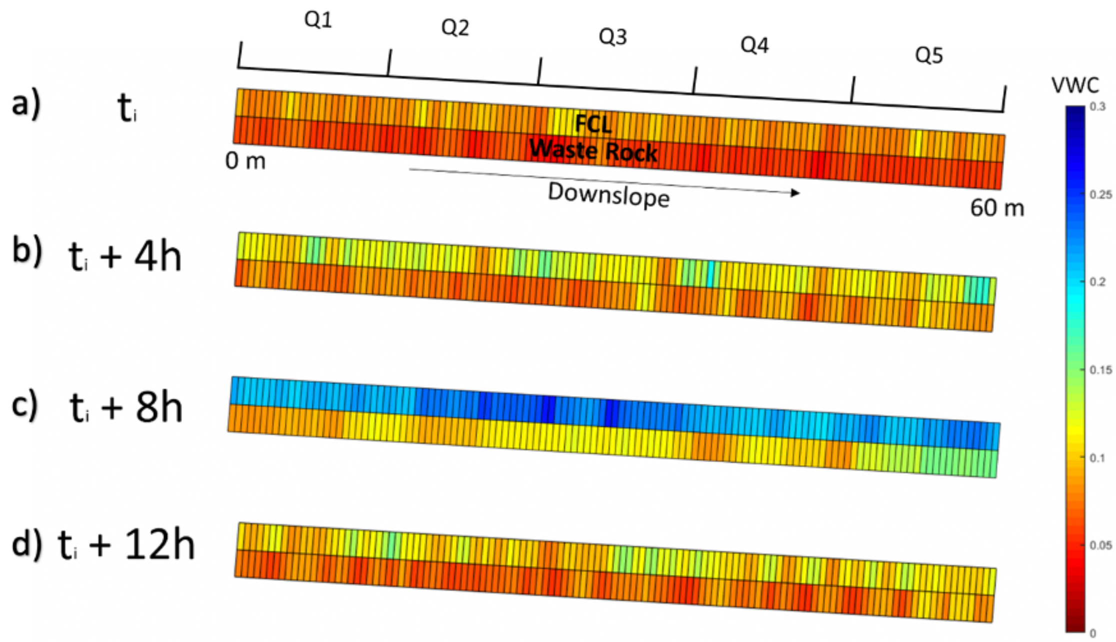

Figure 3.6: Volumetric water content prior to, and after 4, 8, and, 12 hours after the infiltration test has started, separated into 5 quintans.

The results of the active FO-DTS moisture measurements follow similar temporal patterns and trends as the GS3 moisture probes, but the two systems do not give the same absolute values (Figure 3.7). The grey bar around the GS3 measurement represents the manufacturer calibration precision of ±0.03. The fiber optic measurements overestimate the GS3 probe data in the majority of cases. Exceptions are seen at 25 m downslope and 5 m downslope locations in the FCL and waste rock respectively.

The DTS protocol has longer integration time than the GS3. For example, the rise the VWC is seen earlier in the GS3 than the DTS at 25 m downslope in the FCL (Figure 2.7) due to the higher measurement interval of the GS3 probe. The measurement interval of the GS3 is 5 minutes and it is 15 minutes with the active FO-DTS protocol. The distributed nature of the FO-DTS protocol identifies VWC changes undetectable by the GS3 as shown at 55 m downslope in the waste rock below the FCL. One of the main advantages of the DTS protocol is the continuous representation of the entire measurement area. However, the local precision may not be as accurate as spot measurements such as those with the GS3 probes.

3.6. Analysis and Discussion

3.6.1. Assessment of the FCL

The main objective of the experimental pile design with the FCL was to favor horizontal flow towards the toe of the pile. The lateral flow within the FCL is related to the capillary barrier effect at the interface with the coarse waste rock, which induces a retention force wherefore water tends to remain in the overlying sand layer and flow laterally towards the toe of the pile. The degree of saturation in the FCL would naturally be higher downslope, when approaching the toe, with minimal vertical drainage to the waste rock underneath (Fala et al., 2005; Aubertin et al., 2009).

Pre-infiltration test, the FCL was not saturated and had a maximum average VWC of 0.10. The effective of the FCL is dictated by the contrast in grain size and hydraulic properties of the FCL and waste rock (MEND 2004). A dry FCL could also exhibit hydrophobic properties, aiding the diversion capacity of the cover. Infiltration rates may be reduced on order of magnitudes in water repellent soils (Brandt 1969a; Wallis and Horne 1992). Wallis et al. (1991) demonstrated that the hydrologic balance is affected by water repellency of dry soils under heavy rainfall in irrigation systems. The effect of an increased degree of saturation in the FCL would hinder the effectiveness of the cover, however, it could provide a more natural initial condition for the experiment. The initial VWC at the start of the experiment was not controlled as part the experiment design, rather as a result of precipitation event weeks prior to the test.

The VWC was measured using active FO-DTS in the FCL and waste rock prior to, during, and after the 4-hour water infiltration test. Temperature was measured every 0.5 m across the four cable lanes along the pile in the sand layer and waste rock below, for a total of 968 spatial-distributed measurement points. The point density is thus one measurement per 1.25 m^2 along the surface of the experimental pile.

A gradual increase of VWC from the head downslope towards the toe of the pile was expected based on numerical simulations (e.g. Fala et al., 2005; Broda et al., 2014). The highest VWC in the FCL was measured near the middle (second and third quintans of the pile (Figure 3.6c). The water retained in this area of the FCL does not appear to drain into the waste rock below, with a VWC remaining near 0.11 in the waste rock, with exception of the fifth quintan where the VWC exceeds 0.15. Water thus appears to be held in FCL by capillary forces with some moving laterally towards the toe of the pile where it accumulates and drains into the waste rock (as indicated by the low VWC in the first 4 quintans below the FCL)

The limited downslope variability of moisture content in the FCL sand uphill of the fifth quintan appears to be related, at least in part, to its higher than anticipated density (due to heavy compaction), which reduced hydraulic conductivity and increased the VWC by capillary retention (before and during the infiltration test). The FCL allowed some lateral drainage during the infiltration test but held water strongly, as shown by the relatively large VWC, which did not flow laterally as quickly as expected towards the toe of the pile despite the inclined angle of the layer (compared with the preliminary simulation results of Broda et al., 2014, conducted before the pile construction). A more rapid and efficient drainage in the sand layer would have resulted in the upper and core sections of the FCL to be at lower VWC than near the toe. Both the active FO-DTS protocol and GS3 soil moisture probes results confirm that this did not occur as well as initially planned (Figure 3.4). The post-infiltration field measurements shown in Figure 3.6c indicates that a higher quantity of water moved and was stored downslope, near the longitudinal center of the pile. Thus, the FCL had a shorter diversion length than expected for this artificial precipitation event, due to the in-situ material properties that differed somewhat from the original design.

Strong crosswind during the infiltration test may also have played a role by angling some of the sprayed water towards a side of the pile, as shown in the darker coloration of the sand ramp (Figure 3). Despite the crosswind and some localized surface ponding near the side of the pile, the similarity of the data between the four cables over the entire pile surface suggest that this factor didn't influence significantly the horizontal spread of water which appears evenly distributed across the FCL width when it reaches the FO-DTS cables at the bottom of the FCL.

3.6.2. Assessment of Active FO-DTS Data

Active FO-DTS measurements gave higher VWC values compared with the moisture probes at the field site. The difference in the VWC values obtained from active FO-DTS was more pronounced in the FCL than in the waste rock of the pile. Both types of VWC values generally follow the same trend in the FCL, but the GS3 moisture probes did not detect VWC changes in the waste rock (see Figure 3.7, 55 m downslope). This is likely caused by the finer sampling interval of the FO-DTS at every 0.5 m against the very small scale (local) measurements used to represent the VWC at 10 m sampling interval with the GS3 layout. In addition, the GS3 probes are influenced by many factors, such as mineralogy, electric conductivity of the water, and contact between the soil and the probe (Son et al., 2017). As the volume of measurement of this probe is small, large particles (and pores) near the probe could affect significantly the output.

The active FO-DTS results have lower temporal resolution than the GS3 probe measurements (1 hour versus 10 minutes respectively). However, the active FO-DTS measurements can resolve finer spatial changes in VWC than the GS3 moisture sensors at a distributed scale, but at the expense of noisier results. For example, at the field experimental site, there were 30 GS3 probes installed in the FCL compared to 480 measurement locations for the active FO-DTS in the same unit. Nonetheless, the active FO-DTS protocol can detect drainage into the waste rock pile at the toe of the pile, at the resolution applied in the experiment.

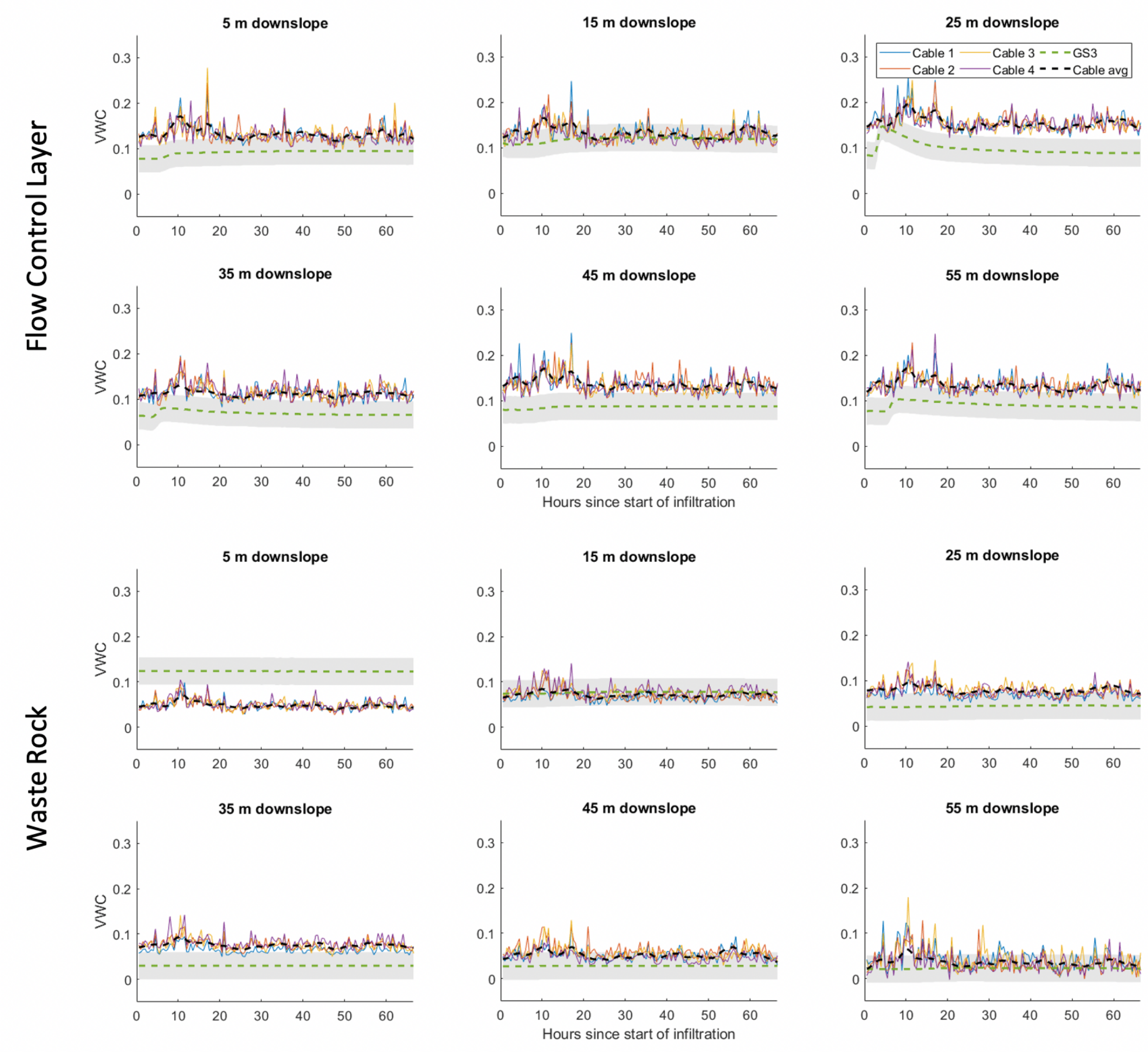

Figure 3.7: Comparison of volumetric water content measured by the active distribute temperature sensing and the GS3 moisture probes in the Flow Control (sand) Layer and the waste rock underneath, at different distances along the pile. The grey bar represents the manufacturer stated accuracy of ± 0.03.

The GS3 probe values in the FCL used in this experiment were corrected to values obtained with a nucleodensimeter (Bréard Lanoix, 2017, Dubuc, 2018). The nucleodensimeter is an industry standard device that uses gamma rays for precise in-situ VWC measurement in field settings

(Susha Lekshmi et al., 2014). The nucleodensimeter was used adjacent to one GS3 probe, and the difference in values between the two probes, a soil moisture of 0.16, was then applied to all the GS3 values from the FCL (Dubuc, 2018). Nucleodensimeter tests could not be completed in the buried waste rock layer.

In-situ moisture probes are prone to measurement challenges. Due to the heterogeneity and range of pore sizes in a waste rock pile, the accuracy of moisture measurements must be interpreted with care. The FO-DTS measurements resolve VWC from the degree of saturation (see Equation 5), as a function of porosity. For both the FO-DTS and GS3 moisture probe results, porosity becomes a constraint for accurate measurements. The comparison of water content between the FO-DTS and the GS3 moisture probes is thus dependent on the accuracy of the (average) porosity determination. The sand layer (FCL) is well compacted along the fiber optic cable, although the presence of flowing water and the active heating protocol may disrupt soil pore structure and contact resistance to the cable (Sourbeer and Loheide, 2015). This loss of compaction may grow over several freeze and thaw cycles, thus could disrupt the average porosity along the cable. Compactness to the cable may interfere with accurate calculations of VWC during the heating protocol as well.

The waste rock below the FCL is more heterogeneous than the sand layer due to the coarse particles and cobles. Such coarse-grained material has a lower water retention capacity (i.e lower moisture contents), and the accuracy of the FO-DTS measurement can be comparable to the GS3 in the waste rock (Figure 3.7) with an advantage to the former with a highly distributed sensing network. This accuracy decreases at higher moisture contents (Wu et al., 2020), but the waste rock with its relatively large pore spaces allow VWC to remain low during the infiltration test.

3.6.3. Protocol improvements

Future work should be conducted to revise power inputs to improve the signal to noise ratio in active FO-DTS results, improve data interpretation, and allow the implementation to be more economical. The active FO-DTS measurements required line or generated power to the cable to perform measurements. A 15kW generator was used to apply 15 W/m to 537 m of cable. The generator needed to be refueled every two to three days. The cost associated with line electric power or generator fuel may be a limiting for some operations. Therefore, the electrical resistance of the fiber optic cable metal must be taken into account to minimize the energy required to run the FO-DTS protocol. Although a 15kW generator was needed, only 7.8 kW of power was used in the protocol. This discrepancy is explained by the need for nearly 65 A to achieve adequate heating due to the length and resistance of the cable.

An efficient FO-DTS protocol maximizes joule heating for the given resistance and length of cable in a project. Heat is produced in a metal conductor proportional to the square of the current multiplied by the resistance Joule (1843). Therefore, amperage and cable resistance may be a more comprehensive indicator of active FO-DTS protocol. A higher gauge cable can joule heat more efficiently than a thicker gauge cable with the same voltage rating. The length of the cable must be taken into account as resistance it is proportional to length.

The GS3 sensors provided difficult readings in the waste rock because the capacitance of crushed ilmenite was similar to water (~80 at 20 °C) (Topp et al., 1980). This similarity in values requires more work to interpret the GS3 results (Martin et al., 2019). In normal operations, the GS3 assumes there is a large contrast between the dielectric permittivity of the soil (~10) and the water (~80).

Assuming the corrected GS3 values accurately replicate the actual VWC values in the FCL, the active FO-DTS results have a higher volumetric VWC at all locations. The average active FO-

DTS value at all FCL locations is ± 0.06 greater than the average GS3 values, averaged over all time steps in the FCL (Figure 3.7). The VWC given by the FO-DTS cables in the waste rock layer are all within the accuracy margins of the GS3 measurements (± 0.03).

A higher resolution FO-DTS can improve the ratio and can be more cost effective for large scale operations. Installing fiber optical cables to better match the heating strategy for the given environment and cable length would also improve the signal to noise ratio and reduce costs. We suggest a 10-15°C change in temperature in near saturated conditions to be optimal for modern DTS units. A lower wattage and cheaper power supply can produce similar heating requirements if an adequately resistive fiber optic cable is installed to maximize joule heating. If these systems are concurrently optimized, FO-DTS can serve as a useful standalone tool to monitor VWC in waste rock material in full scale waste rock pile.

3.7. Conclusion

The application of active FO-DTS to monitor an experimental waste rock pile shows that an FCL can limit infiltration by storing water and diverting part of this moisture along the FCL and towards the toe of the waste rock pile. The layered cover system induced a capillary barrier effect along the inclined 5% interface and prevented the vertical drainage of water into the waste rock layer. A portion of the water retained in the inclined FCL flowed laterally towards the end of the pile, as expected, and drained down the toe of the waste rock pile. The active FO-DTS protocol measured VWC in a large volume of the waste rock pile and was able to show the diversion capacity of the FCL after an artificial wetting event. VWC assessed during 15-minute heat cycles at 15 W/m every half hour show that water remained confined to the FCL. These results indicated that FO-DTS is practical to monitor moisture changes in waste rock and in a cover layer.

Active FO-DTS is a new potential tool for measuring distributed moisture at the scale of field sites. This study in a constructed environment demonstrates that the technique can be used to measure VWC and unsaturated water movement in mine waste rock and in a sandy soil. The active FO-DTS system can infer VWC comparable to that of GS3 moisture probe values, but heating profiles (along with fiber optic cable properties) could be further optimized to reduce the signal to noise ratio.

The field experiment presented here demonstrates the potential utility in using distributed soil moisture measurements to evaluate the effectiveness of an engineered geotechnical system, such as a waste rock cover system. The results also indicate that careful selection of material (e.g. hydrological properties) is essential for an effective cover layer. By using a system such as active FO-DTS, that is built into the design and installed during construction, we were able to monitor how the system worked post-construction. The field data is now being used to assess if the FCL had the optimum inclination, was made with appropriate materials, and created the required hydrologic contrast between the FCL and waste rock below. This type of monitoring system can be particularly useful for large scale events that may lead to localized processes within the cover system, which might not be identified by a few discrete soil moisture probes.

This paper has thus shown that single source active FO-DTS measurements can capture changes in soil moisture in a field setting. A fiber optic cable can be cost effective and efficient in making distributed VWC measurements in coarse and low thermally conductive soils over a large spatial context. Active FO-DTS has the potential to be utilized in additional industrial applications.

Areas of high-water content in landfills and precision agriculture sites where infiltration is a potential concern are other potential subsurface applications of the technique. Particularly for precision agriculture, good agricultural yields, especially in irrigated areas, is limited by soil moisture and its availability for crops. VWC measurements for irrigation management are commonly obtained from point sensors. Although work in literature has tried proper sensor placement techniques (Dabach et al., 2015), progress for VWC spatial variability and its associated impact on VWC distribution has been minimal. Fiber optic cables provide large amounts of data with high spatial and temporal resolution and can fill the gap of point moisture sensors by monitoring vadose zone hydrology for agricultural yield frameworks. The low temperature rise in aFO-DTS monitoring provides minimal disruption to the medium and allows VWC capture several times per hour, at high spatial resolution which is beneficial to both short- and long-term monitoring.

3.8. Acknowledgement

The authors would like to thank the Research Institute on Mines and Environment (RIME) for their support. Special thanks to the employees of the Rio Tinto and the effort of the technicians, students and interns whom contributed to the construction and monitoring of the waste rock pile. This work was funded by the Natural Sciences and Engineering Research Council of Canada (NSERC), Rio Tinto, and the partners of RIME. The authors would also like to thank CTEMPs, funded by the National Science Foundation (EAR awards 1832109 and 1832170), for provision of experimental design support, logistical support and equipment for the project.

3.9. References

Aubertin, M. 2013. Waste Rock Disposal to Improve the Geotechnical and Geochemical Stability of Piles. 23rd World Mining Congress, Montreal, QC, Canada.

Aubertin, M., O. Fala, B. Bussière, V. Martin, D. Campos, A. Gamache-Rochette, M. Chouteau, and R.P. Chapuis. 2002. Analyse des écoulements de l'eau en conditions non saturées dans les haldes à stériles. Symposium Rouyn-Noranda: L'Environnement et les Mines, Canadian Institute of Mining, Metallurgy and Petroleum, Rouyn-Noranda, QC, Canada.

Aubertin, M., O. Fala, J. Molson, A. Gamache-Rochette, B. Lahmira, V. Martin, G.W. and Wilson. 2005. Évaluation du comportement hydrogéologique et géochimique des haldes à stériles. Symposium Rouyn-Noranda: L'Environnement et les Mines, Canadian Institute of Mining, Metallurgy and Petroleum, Rouyn-Noranda, QC, Canada.

Aubertin, M., E. Cifuentes, V. Martin, S. Apithy, B. Bussière, J. Molson, and A. Maqsoud. 2006. An Investigation of Factors that Influence the Water Diversion Capacity of Inclined Covers with Capillary Barrier Effects. Unsaturated Soils 2006. doi:10.1061/40802(189)47

Aubertin, M., E. Cifuentes, S. Apithy, B. Bussière, J. Molson, and R.P Chapuis. 2009. Analyses of Water Diversion along Inclined Covers with Capillary Barrier Effects. Canadian Geotechnical Journal, 46: 1146-1164.

Barbour, S. L., M.J. Hendry, J.L. Smith, R.D. Beckie, and G.W. Wilson. 2001. A research partnership program in the mining industry for waste rock hydrology. University of Saskatchewan, Canada.

Benitez-Buelga, J., C. Sayde, L. Rodríguez-Sinobas, and J.S. Selker. 2014. Heated Fiber Optic Distributed Temperature Sensing: A Dual-Probe Heat-Pulse Approach. Vadose Zone Journal, 13(11).

Benitez-Buelga, J., L. Rodríguez-Sinobas, R. García-Calvo, M. Gil-Rodríguez, C. Sayde, and J. Selker. 2016. Calibration of soil moisture sensing with subsurface heated fiber optics using numerical simulation. Water Resour. Res. 52.

Blight, G.E. 2010. Geotechnical Engineering for Mine Waste Storage Facilities, CRC.

Brandt, G.H. 1969. Water movement in hydrophobic soils. Proc. Symp. Water Rep. Soils, Univ. Calif., Riverside.

Bréard Lanoix, M., Pabst, T. and Aubertin, M. 2020. Field determination of the hydraulic conductivity of a compacted sand layer controlling water flow on an experimental mine waste rock pile. Hydrogeol J (2020). https://doi.org/10.1007/s10040-020-02129-7.

Broda, S., M. Aubertin, D. Blessent, E. Hirthe, and T. Graf. 2014. Improving control of contamination from waste rock piles. Environmental Geotechnics, 4(4): 274-283.

Bussière, B., S. Apithy, M. Aubertin, and R.P. Chapuis. 2003. Diversion capacity of sloping covers with capillary barrier effect. In Proceedings of the 56th Annual Canadian Geotechnical Conference, Winnipeg, Man., 28 September – 1 October 2003. [CD-ROM]. BiTech Publishers Ltd., Richmond, B.C.

Bussière, B., I. Demers, I. Dawood, B. Plante, M. Aubertin, A. Peregoedova, G. Pepin, G. Lessard, R. Intissar, M. Benzaazoua, J.W. Molson, M. Chouteau, G.J. Zagury, M. Monzon, and D. Laflamme. 2011. Comportement géochimique et hydrogéologique des stériles de la mine Lac Tio. Symposium sur l'environnement et les mines, Canadian Institute of Mining, Metallurgy and Petroleum, Rouyn-Noranda, QC, Canada.

Carslaw, H. S., and J.C. Jaeger. 1959. Conduction of heat in solids. Oxford: Clarendon Press.

Chi, X., R.T. Amos, M. Stastna, D.W. Blowes, D.C. Sego, and L. Smith. 2013. The Diavik Waste Rock Project: Implications of wind-induced gas transport. Applied Geochemistry, 36, 246-255. doi:10.1016/j.apgeochem.2012.10.015

Ciocca, F., I. Lunati, N.V. Giesen, and M.B. Parlange. 2012. Heated fiber optic for Distributed Soil-Moisture Measurements: A Lysimeter Experiment. Vadose Zone Journal, 11(4). doi:10.2136/vzj2011.0199.

Climate Change Canada. 2019. HAVRE-SAINT-PIERRE A - Historical Data. Climate - Environment and Climate Change Canada. http://climat.meteo.gc.ca/historical_data/search_historic_data_stations_e.html?searchType=stnName&timeframe=1&txtStationName=havre&searchMethod=contains&optLimit=yearRange&StartYear=1840&EndYear=2019&Year=2019&Month=9&Day=16&selRowPerPage=25.

Dabach, S., U. Shani, and N. Lazarovitch. 2015. Optimal tensiometer placement for high-frequency subsurface drip irrigation management in heterogeneous soils. Agricultural water management, 152, 91-98.

Dettmann, U., and M. Bechtold. 2018. Evaluating Commercial Moisture Probes in Reference Solutions Covering Mineral to Peat Soil Conditions. Vadose Zone Journal, 17(1), 0. doi:10.2136/vzj2017.12.0208

Dimech, A., M. Chouteau, E. Chou, M.V. Aubertin, B. Martin, B. Bussière, and B. Plante. 2017. Monitoring water infiltration in an experimental waste rock pile with time-lapse ERT and multi-parameter data collection. In Symposium on the Application of Geophysics to Engineering and Environmental Problems 2017 (pp. 195-203). Society of Exploration Geophysicists and Environment and Engineering Geophysical Society.

Dimech, A., M. Chouteau, V. Martin, M. Aubertin, B. Bussière, and B. Plante. 2018. 3D Time-Lapse Geoelectrical Monitoring of Moisture Content In An Experimental Waste Rock Pile:

Validation Using Hydrogeological Data. Symposium on the Application of Geophysics to Engineering and Environmental Problems 2018. doi:10.4133/sageep.31-009.

Dubuc, J. 2018. Étude du comportement hydrogéologique d'une couche de contrôle des écoulements placée à la surface d'une halde à stériles expérimentale (Doctoral dissertation, École Polytechnique de Montréal).

Fala O., J. Molson, M. Aubertin, and B. Bussière. 2005. Numerical modelling of flow and capillary barrier effects in unsaturated waste rock piles. Mine Water and the Environment, 24(4), 172-185.

Halloran, L. J., G.C. Rau, and M.S. Andersen. 2016. Heat as a tracer to quantify processes and properties in the vadose zone: A review. Earth-Science Reviews, 159, 358-373. doi:10.1016/j.earscirev.2016.06.009.

International Network for Acid Prevention (INAP). 2017. Prevention and Mitigation. Global Acid Rock Drainage Guide. O'Kane Consultants Inc., (Eds).

Joule, J. P. 1843. XXXII. On the calorific effects of magneto-electricity, and on the mechanical value of heat. The London, Edinburgh, and Dublin Philosophical Magazine and Journal of Science, 23(152), 263-276.

Kersten, M.S. 1949. Thermal properties of soils. Bulletin 28. Minneapolis: Engineering Experiment Station, University of Minnesota.

Johansen O. 1975. Thermal conductivity of soils. PhD thesis. University of Trondheim, Norway (CRREL Draft Translation 637, July 1977, ADA 044002).

Lefebvre, R., D. Hockley, J. Smolensky, and A. Lamontagne. 2001. Multiphase transfer processes in waste rock piles producing acid mine drainage. Journal of Contaminant Hydrology, 52(1-4), 165-186. doi:10.1016/s0169-7722(01)00157-7

Lu, S., T. Ren, Y. Gong, and R. Horton. 2007. An Improved Model for Predicting Soil Thermal Conductivity from Water Content at Room Temperature. Soil Science Society of America Journal,71(1), 8. doi:10.2136/sssaj2006.0041.

Martin, V., M. Aubertin, G. Zhan, B. Bussière, and R.P. Chapuis. 2006. Investigation into the hydrological behavior of exposed and covered waste rock dumps. Transactions-society for mining metallurgy and exploration incorporated, 318, 139.

Martin, V., B. Bussière, B. Plante, T. Pabst, M. Aubertin, F. Medina, M. Bréard-Lanoix, A. Dimech, J. Dubuc, B. Poaty, R. Wu, J. McKenzie, S. Broda, and D. Chen. 2017. Controlling water infiltration in waste rock piles: Design, construction, and monitoring of a large-scale in-situ pilot test pile. In GeoOttawa 2017 - 70th Canadian Geotechnical Conference, Ottawa, ON, Canada

Martin, V., T. Pabst, B. Bussière, B. Plante, and M. Aubertin. 2019. A new approach to control contaminated mine drainage generation from waste rock piles: Lessons learned after 4 years of field monitoring. Geo-Environmental Engineering 2019, Montreal, Canada, May 30-31, 2019.

McCarter, M.K. 1990. Design and Operating Considerations for Mine Waste Embankments. Surface mining, Society of mining, metallurgy and exploration, Littleton, CO, USA, 890-899.

McLemore, V. T., Fakhimi, A. van Zyl, D. Ayakwah, G. F., Anim, K. Boakye, F. Ennin, P. Felli, D. Fredlund, L.A.F. Gutierrez, S. Nunoo, S. Tachie-Menson, and V.C. Viterbo. 2009. Questa Rock Pile Weathering Stability Project - Literature review of other rock piles: characterization, weathering, and stability. Open-file Report OF-517, New Mexico Bureau of Geology and Mineral Resources.

Mine Environment Neutral Drainage (MEND). 2004. Design, Construction and Performance Monitoring of Cover Systems for Waste Rock and Tailings. Report 2.21.4, Natural Resources Canada.

Meter Environment. 2016. GS3 water content, EC and temperature sensors, operator's manual. Decagon Devices, Pullman, WA.

Morin K. A., E. Gerencher, C.E. Jones, and D.E. Konasewich. 1991. Critical literature review of acid drainage from waste rock. MEND Report 1.11.1, Natural Resources Canada.

Nichol, C. F. 2002. Transient flow and transport in unsaturated heterogeneous media: field experiments in mine waste rock (Doctoral dissertation, University of British Columbia).

Peregoedova, A. M. Aubertin, and B. Bussière. 2013. Laboratory Measurement and Prediction of the Saturated Hydraulic Conductivity of Mine Waste rock. GeoMontreal 2013, Canadian Geotechnical Society, Montreal, QC, Canada.

Plante, B., M. Benzaazoua, B. Bussière, M.C. Biesinger, and A.R. Pratt. 2010. Study of Ni sorption onto Tio mine waste rock surfaces. Applied Geochemistry, 25(12), 1830-1844.

Plante, B., B. Bussière, and M. Benzaazoua. 2014. Lab to field scale effects on contaminated neutral drainage prediction from the Tio mine waste rocks. Journal of Geochemical Exploration, 137, 37-47.

Poaty, B, B. Plante, B. Bussière, M. Benzaazoua, T. Pabst, M. Aubertin, V. Martin, M. Thériault, and P. Nadeau. 2018. Geochemical behavior of different waste rock configurations from the Lac Tio mine: Comparison between column tests and experimental waste rock pile results. In Proceedings of Tailings and Mine Waste Conference, Keystone, CO. Vol. 30, pp. 811-821.

Ross, B. 1990. The diversion capacity of capillary barriers. Water Resources Research, 26: 2625–2629.

Sayde, C., C. Gregory, M. Gil-Rodriguez, N. Tufillaro, S. Tyler, N.V. Giesen, and J.S. Selker. 2010. 663 Feasibility of soil moisture monitoring with heated fiber optics. Water Resources Research, 46(6). doi:10.1029/2009wr007846.

Sayde, C., J.B. Buelga, L. Rodriguez-Sinobas, L. El Khoury, M. English, N. van de Giesen, and J.S. Selker. 2014. Mapping variability of soil water content and flux across 1–1000 m scales using the Actively Heated Fiber Optic method. Water Resources Research, 50(9), 7302-7317.

Selker, J., L. Thévenaz, H. Huwald, A. Mallet, W. Luxemburg, N. van de Giesen, M. Stejskal, J. Zeman, M. Westhoff, and M.B. Parlange 2006, Distributed fiber optic temperature sensing for hydrologic systems, Water Resour. Res., 42, W12202

Selker, J., N.V. Giesen, M. Westhoff, W. Luxemburg, and M.B. Parlange. 2006. Fiber optics opens window on stream dynamics. Geophysical Research Letters, 33(24). doi:10.1029/2006gl027979.

Son, J., W. Shin, and J. Cho. 2017. Laboratory and Field Assessment of the Decagon 5TE and GS3 Sensors for Estimating Soil Water Content in Saline-Alkali Reclaimed Soils. Communications in Soil Science and Plant Analysis, 48(19), 2268-2279. doi:10.1080/00103624.2017.1411501

Sourbeer, J. J. and S.P. Loheide. 2015. Obstacles to long-term soil moisture monitoring with heated distributed temperature sensing. Hydrological Processes, 30(7), 1017-1035. doi:10.1002/hyp.10615

Susha-Lekshmi S.U., D.N. Singh, and M. Shojaei-Baghini. 2014. A critical review of soil moisture measurement. Journal of the International Measurement Confederation. Vol. 54, pp. 92-105

Tallon, L. K., M. O'Kane, B.C. Si, and S.L. Barbour. 2013. Distributed temperature observations reveal the scale of spatial variability in unsaturated soil covers. Okane. https://www.okc-sk.com/new/wp-content/uploads/2015/04/Tallon-et-al-2013-Distributed-temperature-observations-reveal-the-scale-of-spatial-variability-in-unsaturated-soil-covers.pdf

Topp, G.C., J.L. Davis, and A.P. Annan. 1980. Electromagnetic determination of soil water content: Measurements in coaxial transmission lines. Water Resources Research, 16(3): 574-582, doi: 10.1029/WR016i003p00574.

Van De Giesen, N., S.C. Steele-Dunne, J. Jansen, O. Hoes, M.B. Hausner, S. Tyler, and J. Selker. 2012. Double-ended calibration of fiber-optic Raman spectra distributed temperature sensing data. Sensors, 12(5), 5471-5485.

Vereecken, H., J.A. Huisman, H. Bogena, J. Vanderborght, J.A. Vrugt, and J.W. Hopmans. 2008. On the value of soil moisture measurements in vadose zone hydrology: A review, Water Resour. Res., 44, W00D06, doi:10.1029/2008WR006829.

Wallis, M.G., D.R. Scotter, and D.J. Horne. 1991. An evaluation of the intrinsic sorptivity water repellency index on a range of New Zealand soils. Aust. J. Soil Res. 29: 353–362.

Wallis M.G. and Horne D.J. 1992. Soil Water Repellency. In: Stewart B.A. (eds) Advances in Soil Science. Advances in Soil Science, vol 20. Springer, New York, NY. https://doi.org/10.1007/978-1-4612-2930-8_2

Weiss, J. D. 2003. Using Fiber Optics to Detect Moisture Intrusion into a Landfill Cap Consisting of a Vegetative Soil Barrier. Journal of the Air and Waste Management Association, 53(9), 1130-1148. doi:10.1080/10473289.2003.10466268.

Wilson, J. A., G.W. Wilson, and D.G. Fredlund. 2000. Numerical modeling of vertical and inclined waste rock layers, in Proceedings of 5th International Conference on Acid Rock Drainage. Denver, Colorado, pp. 257-266.

Wu, R., V. Martin, J. Mckenzie, S.B. Broda, B. Bussière, M. Aubertin, and B.L. Kurylyk. 2020. Laboratory Scale Assessment of a Capillary Barrier using Fiber Optic Distributed Temperature Sensing (FO-DTS). Canadian Geotechnical Journal, 57(1), 115-126. doi:10.1139/cgj-2018-0283

4. Uncertainties in Measuring Soil Saturation with aFO-DTS

Authors: Robert Wu, Pierrick Lamontagne-Hallé, and Jeffrey M. McKenzie

4.1. Abstract

Active fiber optic distributed temperature sensing (aFO-DTS) measures soil saturation at sub-meter intervals across kilometres of fiber optic cable. The technology has great potential but presents challenges in calibration across field scales with variable soil conditions. To better understand and quantify the errors associated with aFO-DTS soil moisture measurements, we use a parametric numerical modeling approach to assess different error factors in a uniform sand medium. A SUTRA thermo-hydrogeologic, unsaturated model is used to simulate a 0.01 m by 0.01 m 2D domain with a fiber optic cable at the center. Observed measurements are compared to soil moisture values calculated using the T_{cum} calibration method. The model has a high accuracy value between measured and observed saturations in a homogeneous soil. We test the accuracy of commonly used protocol settings and the effects of parameters changes to calibration accuracy, including length of recharge and different heterogeneous scenarios. The accuracy decreases as the variability in soil properties and recharge events increases. Further, we demonstrate that the burial and compaction of the cable within a soil can potentially have a large impact on the quality of results. The results demonstrate the need for careful selection of calibration curve(s) for this emerging method of measuring soil moisture.

4.2. Introduction

Soil saturation is a critical component of a subsurface hydrologic budget. The movement of water through the vadose zone is important for larger groundwater recharge processes, hydrology hillslope response, and ecohydrology (Amin et al., 2020; Scanlon et al., 2002; Tyler &

Wheatcraft, 1989). Furthermore, the distribution of soil saturation is an important variable for agricultural applications (Hausner, 2010) and geoengineering (Wu et al., 2021). Soil saturation is often measured using technologies such as capacitance and electrical conductivity probes (Dorigo et al., 2011). With calibration, these methods can provide very accurate measurements of soil saturation but are limited in that they provide soil saturation at discrete points and may not capture the intrinsic variability of the subsurface. Recently there have been improvements in high resolution remote sensing of soil saturation but is limited to very shallow depths (Wigmore et al., 2019).

Active Fiber Optic Distributed Temperature Sensing (aFO-DTS) technology has great potential for the measurement of spatially distributed soil saturation. Fiber optic distributed temperature sensing has been traditionally utilized in hydrology to measure temperature and heat fluxes in rivers and streams, and in recent decades this technology has evolved into (active) soil saturation operations (Weiss, 2003). The aFO-DTS method is based on inferring soil water content from observing the thermal response of a soil to a controlled heat pulse (Sayde et al., 2010). A fiber optic cable is buried in the subsurface. An induced heat pulse is generated by applying an electrical current to the steel core of the fiber optic cable. The thermal response measured by the fiber optic cable in the soil is a function of the bulk thermal properties of the soil, which is in part a function of soil water content thereby allowing for the calculation of soil saturation.

Thermal response is achieved by employing aFO-DTS technology which allows a resolution of temperature measurements as fine as 0.125 m every 1 s along a fiber optic cable buried in soil. This measurement density and sampling interval has been achieved in cables over 10 km in length. The measurement of water content has great potential with aFO-DTS but presents challenges in calibration across field scale variable soil conditions (Benítez-Buelga et al., 2016; Sayde et al., 2014; Striegl & Loheide II, 2012; Weiss, 2003; Wu et al., 2021).

In a field scale deployment of aFO-DTS, the measurement of soil saturation is simultaneously taken at all locations along the fiber optic cable. The changes of thermal responses in all locations will not be only a function of variability in soil saturation but also the spatial heterogeneity of the bulk soil properties, the range in precipitation intensity and duration, and the effect of heat pulses on the soil. Thus, the calibration protocol relating the measured thermal response to the soil thermal properties and to soil water content must reflect the particularity of each location. This is challenging due to the limited available information on the spatial variability of soil thermal properties in field scale experiments and the challenge to measure these properties representatively.

Dong et al. (2016) provided one strategy for sites without active heating capability through an adaptive Particle Batch Smoothing algorithm in conjunction with Hydrus-1D modeling to assimilate DTS observations of soil temperature diurnal fluctuations and simultaneously reveal soil water content and key soil thermal and hydrological properties. This study is the first to assess variability of soil thermal properties at the scale needed for effective distributed calibration.

Bulk soil thermal properties can vary greatly spatially and temporally. Soil saturation has a major impact on this variation. Other factors such as bulk density, mineralogy, organic matter content and temperature contribute to the spatial variability of heat exchange in soils (de Vries, 1952). For instance, with an increase in soil compaction, porosity decreases and, as a result, particle contact increases (Sourbeer & Loheide, 2016). The increase in particle contact is important in mineral soils where grains have a higher thermal conductivity than water and air. Heat will preferentially travel through the connected mineral grains instead of the more insulating liquid and gas media. Soil mineralogy can also contribute to the variability of thermal conductivity. For example, quartz has a thermal conductivity three times higher than common soils (de Vries, 1952) and the proportion of quartz in the soil profile will greatly affect soil thermal conductivity.

The thermal response of soil to pulse heating can be calculated in the form of cumulative temperature increase, T_{cum} (s°C) as described in (Sayde et al., 2010):

$$T_{cum} = \int_0^{t_0} \Delta T \, dt \tag{1}$$

where t_0 (s) is the heat pulse integration period, and ΔT (°C) is the temperature change with respect to ambient conditions. As T_{cum} is used as a token term for thermal conductivity, all factors that affect thermal conductivity are expected to affect T_{cum}. In field deployments of aFO-DTS, a calibration protocol relating T_{cum} to soil saturation should account for the spatial variability of soil thermal properties, which is often non-linear. Variability in thermal conductivity can influence the relationship between T_{cum} and soil saturation, thus affecting the accuracy of the protocol. There are several ways to calibrate thermal properties to soil saturation:

- Model calibration curves from field samples at different soil water contents. Benítez-Buelga et al. (2016) collected undisturbed samples from the field and measured the thermal properties of the samples under varying soil saturation conditions to create a calibration function from thermal properties to soil saturation. The calibration function was employed in a heat transport model to generate another calibration function relating T_{cum} to soil saturation for the specific soil in the study.

- Field generated calibration curves based on soil saturation probe results. Cao et al. (2018) generated calibration curves relating the thermal response of the aFO-DTS cable to soil saturation content measured by soil saturation probes installed next to defined sections of the heated fiber optic cable.
- Laboratory generated curves from soil columns. Wu et al. (2020) packed soil into a column equipped with fiber optic cable. The water table in the column was controlled to impose different soil saturation conditions inside the soil column. The calibration curve relating T_{cum} to soil saturation was obtained by fitting a curve to the T_{cum}-soil saturation content collocated measurements.

The calibration protocols described above can be challenging to apply when large variability in the background soil thermal properties is observed. In a natural and heterogeneous environment, it is seemingly impractical to apply the calibration methods described above. Observations from different locations are required to cover the range of spatial variability of soil thermal properties and, even when the range of variability is known, there is little literature detailing the practicality and associated errors in assigning aFO-DTS measurements to a particular calibration function.

In this study, the authors use a coupled thermo-hydrogeologic numerical model, SUTRA (Voss & Provost, 2002), to assess potential errors in aFO-DTS measurements of soil saturation. This study is not intended to be a comprehensive model of aFO-DTS behaviour and conditions, but rather to identify and test common assumptions in heat pulse protocol and analysis of the potential errors in soil saturation calculations in field based experiments. Common untested assumptions, such as the effect of ambient soil saturation, amount of recharge, length of active heating, and the distribution of heterogeneities are assessed with the numerical model simulations. Using an analysis-based approach, we run a base scenario model with uniform parameters. We then vary parameters to test the commonly used assumptions, scenarios, and protocols used in field based aFO-DTS soil saturation studies.

4.3. Methods

4.3.1. SUTRA Model

SUTRA is a finite element model for saturated-unsaturated groundwater flow with energy and solute transport developed by the USGS (Voss & Provost, 2002). SUTRA uses a modified Richards equation coupled with a conductive-advective heat transport equation. The model includes temperature-dependent fluid density and the effects of soil saturation on the subsurface hydraulic and thermal properties. However, it does not simulate vapor or air flow nor vaporization of the pore water. See Voss and Provost (2002) for a detailed description of SUTRA's governing equations. In this study, unsaturated conditions are considered, thus the pores are only variably filled with some proportion of water and air. The soil saturation is calculated from the modelled pressure at each time step following the van Genuchten function.

As one of the most complete groundwater modelling tools (Deeds and Jones, 2011), SUTRA has been applied to numerous field settings (e.g. Bobba, 1993; Woods, 2003) including seawater intrusion (e.g. Gingerich and Voss, 2005; Smith, 2004), future water resources evaluation (e.g. Kurylyk et al., 2014; Oki et al., 2019), geothermal reservoirs (Burns et al., 2015; Burns et al., 2020), and permafrost thaw (e.g. Lamontagne-Hallé et al., 2018; McKenzie & Voss, 2013).

4.3.2. Modifications to the SUTRA Model

To adapt the model for use with aFO-DTS simulations, SUTRA was modified to include timed active heating conditions where simulated energy is applied into the model at set intervals. SUTRA calculates the subsurface bulk thermal conductivity with a weighted arithmetic mean from the thermal conductivities of every constituents of the porous matrix (i.e., soil particles and water) and ignores the air phase. However, the arithmetic mean does not always offer accurate estimates of bulk thermal conductivity (Buntebarth & Schopper, 1998) and ignoring the air phase may amplify these inaccuracies (Xie et al., 2020). To investigate the relationship between active heating and T_{cum}, the SUTRA bulk thermal conductivity equation, K, (Voss & Provost, 2002) was modified to integrate the air phase with a weighted harmonic mean:

$$K = 1/[\varepsilon(S_L/K_L + (1 - S_L)/K\_A) + (1 - \varepsilon)/K\_S] \quad (2)$$

where ε is porosity, S_L is water saturation, and K_L, K_A and K_S are the thermal conductivities of water, air phase and soil particles, respectively. The harmonic mean provided better estimates of bulk thermal conductivity compared to the arithmetic mean (Nield and Bejan, 1999).

The SUTRA source code was also modified so that the source of energy (active heating) is applied to all mesh nodes of the steel core of the fiber optic cable to cumulatively add to 10 W in the domain. This modification is necessary to provide a satisfactory heat pulse in saturated, low temperature conditions.

4.3.1. Model Setup

4.3.1.1. Domain and Mesh

The parameters and domain for the model are based on a field experiment presented in Wu et al. (2021). For the field experiment, aFO-DTS was used to measure soil moisture in a sand unit that is part of a constructed waste rock pile. This field experiment included careful measurement of many of the parameters required for calculating soil moisture from aFO-DTS and provides a reasonable starting point for the numerical modeling. In the numerical model, physical properties for the sand and cable are based on the system in Wu et al., (2021).

The model domain is a 2D cross-section containing a simulated fiber optic cable buried in homogenous sand. The default base material properties used in the simulations are given in Table 1. The 2D model domain dimension is 0.10 m x 0.10 m, and 1 m thick. The model mesh layout consists of 0.004 m x 0.004 m element spacing in the outer bands and 0.001 m x 0.001 m element spacing in the inner bands (Figure 4.1). A grid refinement study found that the inner grid spacing was sufficiently small for numerical accuracy. Although fiber optic cables are usually rounded, its rectangular representation in the model domain does not affect heat transfer during the simulations as energy is spreading radially at the sand-cable interface.

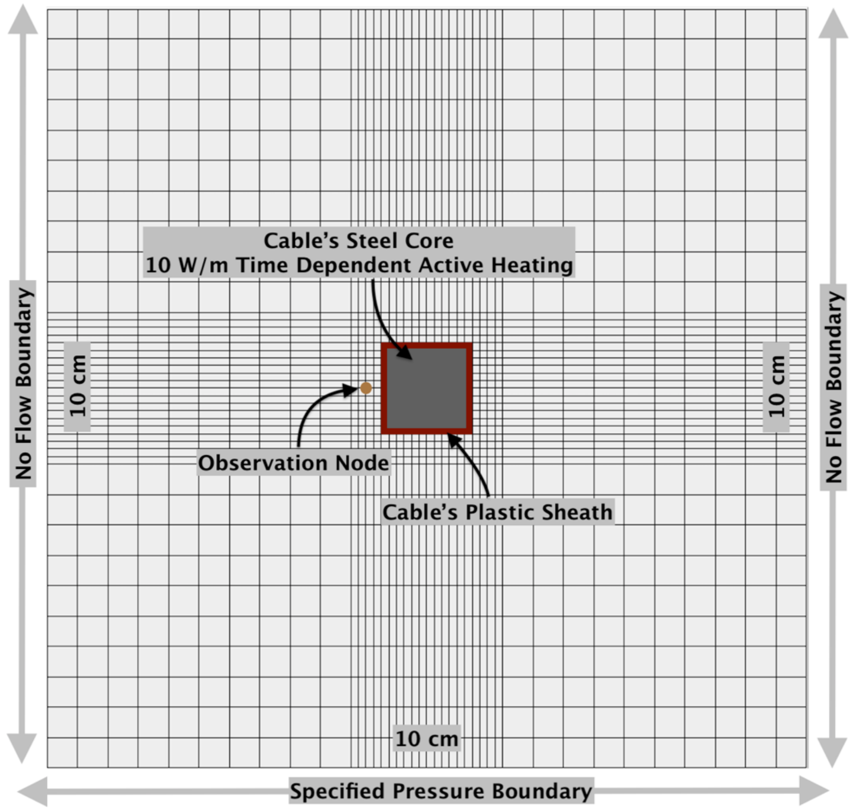

Figure 4.1: Model mesh domain. The domain is 0.10 m x 0.10 m and contains 0.004 m x 0.004 m elements and 0.001 m x 0.001 m elements in the outer and center areas, respectively. The mesh extends into the cable plastic and steel core as well. Soil moisture is measured at the observation node.

The default domain represents a homogeneous, medium-grained sand surrounding the fiber optic cable located in the center of the model domain. The fiber optic cable is represented by a 0.01 m x 0.01 m steel core square surrounded by a 0.001 m thick plastic sheathing. Each medium (sand, plastic and steel) have their own set of hydraulic and thermal properties (Table 1). The permeability of the steel core and plastic sheath have been set to be effectively impermeable (10^{-90} m^2) to avoid water flow inside the cable. The representation of the optical fiber is omitted from the simulations as the effects of the thin glass fiber are assumed to be negligible in energy transfer.

4.3.1.2. Boundary Conditions

The vertical sides of the model domain are no-flow boundaries. The top hydraulic boundary condition allows water to enter the model domain through a time-dependent specified recharge boundary condition. This boundary allows water to enter the domain at specified periods during the model run, with varying intensity and length of recharge. No water may flow out at the top boundary, meaning that all water must be drained at the bottom of the model domain. The hydraulic boundary condition across at the bottom of the domain is a specified pressure boundary condition of -65000 Pa (close to residual saturation) is specified along the bottom of the domain (Figure 4.1). This boundary condition allows water to exit the model to prevent pooling. The simplicity of this “drain” could induce unintended water flowing upwards from the bottom of the model domain, however the distance of the drain to the observation area (adjacent to the cable) of the model is sufficiently large to avoid such phenomenon. The thermal perturbations in the simulations did not reach the model boundaries and that the domain is sufficiently large so that the boundaries do not affect simulation results. The model timestep is one second, with an active heat pulse period of either 15 or 2 minutes. The energy source is applied to the cable steel at 15 W.

The vertical boundary sides of the model are isothermal, with no heat being conducted into or out of the model. Energy may enter the model at the top boundary with the inflowing water during a recharge event. Energy may excite the model via water removed from the specified pressure boundary at the bottom of the model. Along with the heat pulse in the cable’s steel core, this is the only input of heat to the model domain. The temperature of the inflowing water is 20

°C. Water being discharged from the model at the bottom boundary represents the only heat output.

Table 1. Base model parameters

Default Parameters	**Value**
Sand	
Porosity	0.44
Specific Heat of solid (J/kg°C)	840
Thermal Conductivity of solid (J/sm°C)	3.5
Absolute Permeability (m^2)	10^{-12}
Residual Saturation	0.045
Air Entry Value ($[kg/(s^2\ m)]^{-1}$)	0.00035
Pore Size Distribution	3.19
Density of solid (kg/m^3)	2,600
Cable Plastic Sheath	
Porosity	0.001
Specific Heat (J/kg°C)	1.67
Thermal Conductivity (J/sm°C)	0.026
Permeability (m^2)	10^{-90}
Cable Steel	
Porosity	0.001
Specific Heat (J/kg°C)	502
Thermal Conductivity (J/sm°C)	13.389

Permeability (m^2)	10^{-90}
Energy Source (J/s)	15
Additional SUTRA Parameters	
Water Specific Heat (J/kg°C)	4182
Water Thermal Conductivity (J/sm°C)	0.6
Water Compressibility ($[kg/(s^2\ m)]^{-1}$)	4.47×10^{-10}
Longitudinal and Transverse Dispersivity (m)	0.5
Air Thermal Conductivity (J/sm°C)	0.025

4.3.2. Calibration Curves

To use the T_{cum} method to calculate soil moisture, a calibration curve relating cumulative change in temperature to soil moisture conditions is required (Weiss, 2003). We use the model to develop a synthetic calibration curve. Static water conditions, whereby gravity is set to 0 m/s^2 and movement of water is negligible, are built from the default parameters listed in Table 1. The parameters, in theory, represent the ideal conditions for a synthetic aFO-DTS protocol due to the absence of recharge and groundwater flow. To test the protocol, we assume that the cable dimensions produce negligible effects on thermal properties. The static water cases are used to obtain T_{cum} values corresponding to each specific soil saturation condition for 10% soil moisture increments, from 10% to 100% saturation (see below). The heat pulse (i.e. rise in temperature) is calculated from the center of the steel core while soil saturation is recorded at a node in the sand that is 0.004 m to the left of the modeled cable (Figure 4.1). This node can be conceptualized as a point source moisture probe, however it is dimensionless and does not affect the model process during the simulation.

The calculation of T_{cum} as the sum of the temperature values is obtained from the integral of ΔT during the time interval of the heat pulse at the observation node. Initial conditions of temperature correspond to 1 s before the start of the heat pulse. Several studies suggest averaging several minutes before starting the heat pulse would produce a more accurate value of ambient temperature. However, Wu et al., (2021) has noted that this suggestion is impractical for repeating heat pulses because temperature fluctuation following a heat pulse may exceed 1 hour dependent on the soil and heat pulse properties.

The resulting T_{cum} relationship following a heat pulse is nonlinear. There are many suggestions in literature to calculate soil saturation from a heat pulse based on the specific experimental design and soil properties. For the purpose of our default scenario, we find that a cubic function fitted by the least squares method is the best function to calculate soil saturation from T_{cum}.

To compare the accuracy of the static calibration curve, two other calibration curves are built considering different recharge scenarios. These calibration curves are generated from runs following the same conditions as the runs used to generate the static calibration curve, but with three exceptions:

- The initial pressure of these runs was set to -65000 Pa.
- The gravity was set to 9.81 m/s^2
- The top hydraulic boundary condition was changed to a constant specified recharge for 15 and 2 minutes

These recharge rates were calculated to provide the model with enough water to reach the total saturation levels tested previously in the static runs (10% increment).

4.3.3. Protocol Evaluation

The performance of the aFO-DTS protocol to calculate soil saturation is evaluated in comparison to the observation node with respect to soil saturation and time. In the results and figures, the *Saturation Offset* is the difference between the aFO-DTS calculated results and that of the model simulations recorded at the observation node(s). The *Real Saturation* is the saturation measured by the observation node for a given simulation.

The Nash-Sutcliffe Efficiency (NSE; Nash & Sutcliffe, 1970) along with the coefficient of determination (R^2) is used as the performance metrics. The NSE is a useful metric in assessing the quality of time series in hydrological models by analyzing the protocol's ability to predict along a 1:1 comparison line. The NSE is calculated as:

$$NSE = 1 - \frac{\sum(\theta_{obs} - \theta_{calc})^2}{\sum(\theta_{calc} - \bar{\theta}_{obs})^2} \quad (3)$$

where $\theta_{obs}$the modelled observation node soil saturation, $\theta_{calc}$the protocol calculated soil saturation from T_{cum}, and $\bar{\theta}_{obs}$the mean of the soil saturation time series from the observation node. A value of 1 indicates no variance across the 1:1 line of the time series and that the protocol is perfectly reproducing modelled soil saturation at the sand interface. Conversely, a value of 0 suggests the variance in the time series is equal to the variance of the model. While the use of NSE in hydrology is predominantly used for time series stream flow analysis (e.g., Zipper et al., 2018), the use of this indicator on soil saturation allows us to evaluate the effects of long-term aFO-DTS deployment in time series analysis.

4.3.4. Modelling Scenarios

4.3.4.1. Static Water Calibration at every 10% Saturation

The default scenarios for the model are used to build the initial calibration curve, which represents the relationship between T_{cum} and soil saturation in static water. Gravity is set to 0 m/s^2 to prevent flow and all sides of the model are set as no flow boundaries to prevent drainage. In these scenarios, the hydraulic pressure in the model domain is homogeneous, constant, and set to its respective soil saturation content as calculated from the van Genuchten function (i.e. -65000 Pa at residual saturation; Van Genuchten, 1980). The initial temperature is 20 °C everywhere. The default heat pulse length lasts 15 minutes at 10 W/m (the model is 1 m thick). The resultant heat pulse measured in the fiber optic steel core is calculated from T_{cum} and a cubic function calibration is generated to curve-match soil saturation modelled at the observation node. Simulation runs were made from residual to full saturation at 10% increment of soil saturation. The changes and error associated with the protocol calculation should only change with soil saturation and thermal properties of water in the sand pores.

4.3.4.2. Static, Cold Water and 24 Heat Pulses using Static Calibration

To test the accuracy of the aFO-DTS protocol, different model scenarios with varying parameters are simulated using the same no-flow (static) conditions described above. The aFO-DTS protocol saturation offset, the difference between the values calculated with the protocol and modelled at the observation node, and R^2 is calculated for all static scenarios.

The initial temperature in the default scenario is 20 °C. To test the effect of bulk temperatures on protocol performance, initial uniform temperatures of 10 °C and 5 °C are simulated; there are no cases in the literature of using aFO-DTS at near or below freezing temperatures. The active nature of the protocol renders measurements in the presence of frozen ground impractical because the heat generated by the fiber optic cable would both melt pore ice and change the bulk thermal properties of the soil.

An assumption in the method is that the change in temperature under the induced heat pulse is not affected by the value of the initial temperature. Wu et al. (2020) observed that pre-heat pulse temperatures do not return to ambient conditions following successive succeeding heat pulses. A 24 hour test of 15-minute heat pulses every hour is used to assess the error associated with this assumption. This is performed for every 10% saturation.

4.3.4.3. 5 mm to 30 mm Recharge Events - 15 min Flowing Water Calibration

The effect of flowing water on the accuracy of the protocol calibration has not previously been well explored. Using the default static water calibration, simulations evaluated how flowing water may affect aFO-DTS measurements. Gravity is 9.81 m/s^2 for the all the following described runs. A new calibration curve replaces the static calibration based on general heat pulse curve characteristics observed. The saturation calculated by the protocol is now tested against the observation node in the sand adjacent to the cable. The heat pulses are 15 minutes every hour for 24 hours in initially dry (residual soil saturation) conditions and an NSE is reported for the entire time series. Recharge into the top of the model is then added after the first hour. The protocol is tested with cumulative 5 mm recharge increments (from 5 mm to 30 mm recharge). Water is recharged into the top of the model for one hour, during the second hour of the run.

4.3.4.4. 5 mm to 30 mm Recharge Events - 2 min Flowing Water Calibration

To test if heat pulse duration has an effect on accuracy, a shorter heat pulse period was tested to compare with the longer 15 minute integration period using the same recharge values of the previous simulations. A 2 minute heat pulse is used for comparison. All other parameters remain the same as the 15 min calibration runs.

4.3.4.5. 5 mm to 30 mm Recharge Events - 2 min, 20 mm/hr Flowing Water Calibration

The calibration is then recalculated based on values obtained from the 20 mm recharge test and compared with the accuracy from the 15 and 2 minute initial calibration. The purpose of a calibration with specified recharge rate is to test whether an increase in measurement accuracy is obtained when the recharge rate is specific to the calibration. The recharge rate of 20 mm/h is chosen simply because it is halfway between the lowest and highest rates tested, 5 mm/h and 30 mm/h respectively. All other parameters remain the same as the 2 min and 15 min calibration runs.

4.3.4.6. Varying Recharge Length and Soil Heterogeneity

With the *2 min, 20 mm/hr flowing water calibration*, the accuracy associated with the length of recharge is tested for 20 min, 40 min, 80 min, and at 100 min long recharge event while the recharge rate remains the same. The purpose of this test is to measure the accuracy of the protocol using a specified recharge rate calibration when the recharge length is not one hour. While the recharge rate remains the same, the total amount of water, thus the amount and velocity of the watering front is different from the one hour tests.

Heterogeneous changes of the matrix are then tested using this calibration. The sand domain's permeability is adjusted to a gaussian distribution with extremums of two orders of magnitude below and above the default permeability value of 10^{-12} m^2. The soil saturation measurements are compared at three locations with observation nodes above, to the left, and to the right of the cable. The left observation node is seen in Figure 4.1 and the above and right observation nodes are also 0.004 m from the edge of the cable.

A macropore was then added to the domain with a permeability value at 2, 4, and 6 orders higher than the default sand. A scenario in which the permeability of the same area is three orders of magnitude lower was also tested to represent a potentially compacted layer surrounding the cable. The porosity of the macropore is 0.90 and the compacted porosity remained at default values. The observation node stays within the sand layer at default parameters, outside of the macropore.

Three scenarios are simulated to test how a low permeability layer would affect results. This scenario is simulated with a 0.01 m thick horizontal low permeability layer above the cable. The porosity and other capillary properties of the low permeability layer are not altered. This layer is located 0.01 m above the cable and covers the entirety of the model domain along the horizontal axis (i.e., from the left vertical boundary to the right vertical boundary). However, a small 0.001 m wide opening with the default permeability is located right above, or 0.02 m to either side of the cable (either closer or further from the observation node compared to the default scenario). The low permeability zone is two orders of magnitude lower than the default value (10^{-14} m^2).

Table 2: Summary of simulations

Scenarios	Gravity (m/s^2)	Initial Temp (°C)	Saturation Comparison	Heat Pulse Duration (min)	Number of Hourly Cycles	Testing Specific Saturation or Time Series	Calibration	Range of Recharge Rate Used (mm/hr)
Static Calibration, Default	0	20	% of Water Specified in Pores	15	1	Saturation (R^2)	15 min static	0
Static Calibration, Low Initial Temp	0	10, 5	% of Water Specified in Pores	15	1	Saturation (R^2)	15 min static	0
Static Calibration, 24 Heat Pulses	0	20	Observation Node	15	24	Saturation (R^2)	15 min static	0
15 min Flowing Water Calibration	9.81	20	Observation Node	15	24	Time Series (NSE)	15 min flow	5 - 30
2 min Flowing Water Calibration	9.81	20	Observation Node	2	24	Time Series (NSE)	2 min flow	5 - 30
2 min - 20 mm /hr Flowing Water Calibration	9.81	20	Observation Node	2	24	Time Series (NSE)	2 min flow specified for 20 mm/hr	5 - 30
Heterogeneity Runs	9.81	20	Observation Node	2	24	Time Series (NSE)	2 min flow specified for 20 mm/hr	5 - 30
Macropore Runs	9.81	20	Observation Node	2	24	Time Series (NSE)	2 min flow specified for 20 mm/hr	5 - 30
Overlying Low Permeability Layer Runs	9.81	20	Observation Node	2	24	Time Series (NSE)	2 min flow specified for 20 mm/hr	5 - 30
Recharge Length Runs	9.81	20	Observation Node	2	24	Time Series (NSE)	2 min flow specified for 20 mm/hr	20

4.4. Results and Discussion

4.4.1. Static Runs

The static water cases are set at predetermined soil saturation levels, with water remaining stationary throughout the test (see Methodology above). Using a cubic function to calculate T_{cum}

to soil saturation yields an R^2 of 0.99 between the simulated and calculated soil moisture values for the default static water test.

The effect on accuracy of the aFO-DTS protocol by applying water colder than the ambient temperature of the bulk medium is negligible (Figure 4.2). The drop in water temperature to 10 °C and 5 °C from 20 °C produced a change in soil saturation value of ± 0.01%. R^2 remains 0.99.

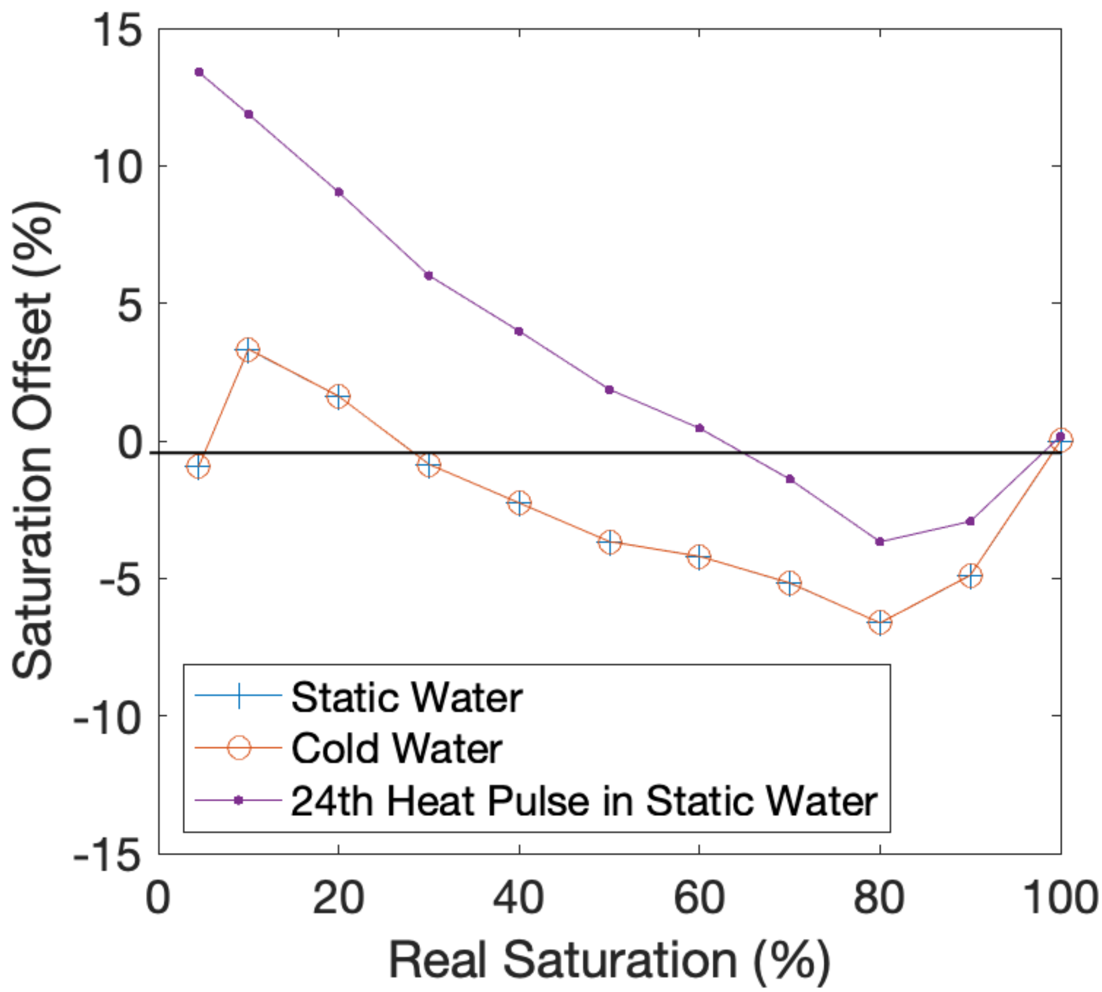

Figure 4.2: Static Simulations: Plot displaying the effects of cold water infiltration, and the cumulative effect of repeated hourly heat pulses on the accuracy of the protocol calculation. Real saturation refers to the saturation that is set with the model parameters.

The effect of 24 repeated 15 minute heat pulses at one hour intervals results in an R^2 of 0.99 when comparing the soil saturation at the observation node to the calculated protocol value at the end of the 24th cycle. The saturation offset (difference in protocol and node value) is within ± 4% at and above 40% saturation (Figure 4.3). Below 40% saturation, the aFO-DTS protocol has a saturation bias greater than +4%. The offset is 13.4% at residual saturation levels. This suggests that the error associated with repeated heating cycles at low saturation may hinder accurate calculation of soil saturation, although the offset drops with increasing soil saturation. The error in the calculation initially increases with each heat pulse but reaches a plateau by the 4th cycle. A shorter integration period may reduce the offset at lower saturations.

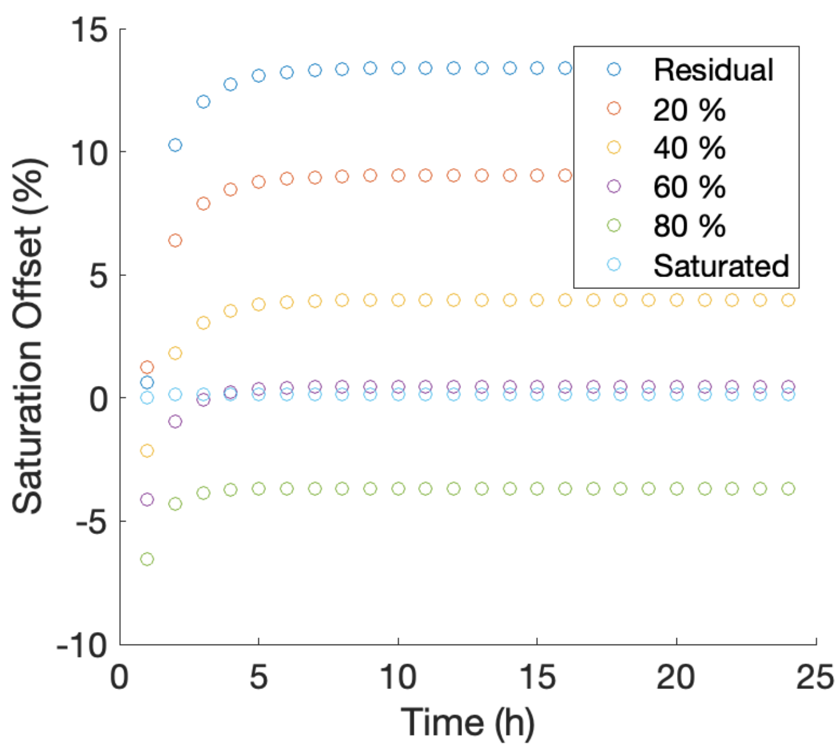

Figure 4.3: Effect on aFO-DTS protocol accuracy after repeated heat pulses (once an hour) for different saturation levels. Accuracy changes within the first 4 heat cycles after which becomes unaffected with subsequent heat pulses.

4.4.2. Simulations with 15 Minute Calibration

For more realistic boundary conditions, simulations are run with a range of recharge rates instead of specified saturation levels, and allow for percolation by setting the gravity to 9.81 m/s^2. Recharge rates from 5 mm/h to 30 mm/h are simulated to view the performance of the protocol in a broad spectrum of recharge intensities (Figure 4.4). The recharge period is one hour and starts at the beginning of hour two of the test. The saturation offset is calculated from the comparison with the 15 minute flow calibration curve.

The resulting saturation offset is much higher than the static cases. The NSE is 0.57 for 30 mm recharge, and 0.07 for 5 mm. The highest offset is during the second hour of the test when recharge is actively being applied to the model domain. The offset is 59% and 39% for 5 mm/h and 20 mm/h recharge respectively. The offset in the 30 mm/h test is reduced to below 12% by the fourth hour, while the offset in the 5 mm/h test does not drop below 28%.

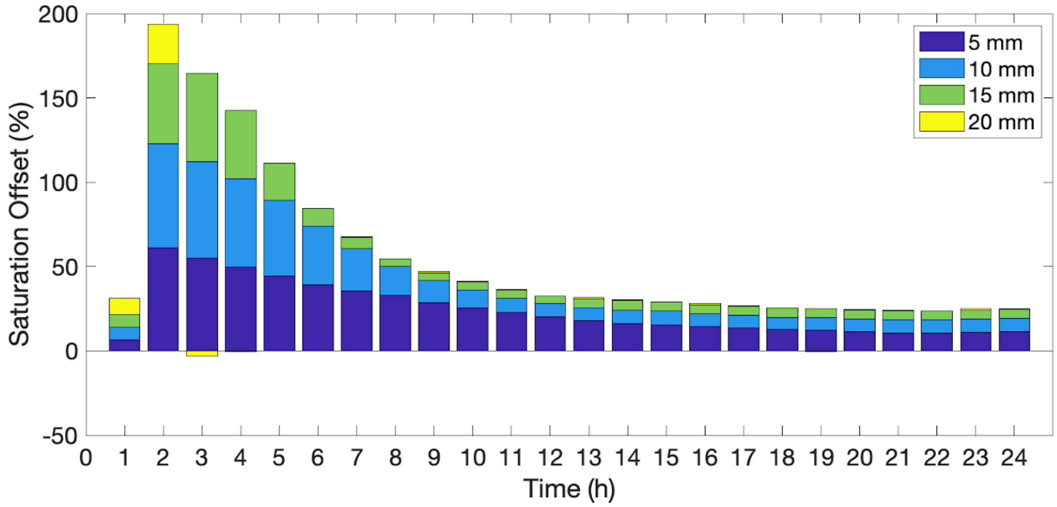

Figure 4.4: Run results, with 15 minute calibration, for 5, 10, 15, and 20 mm of recharge. (25 mm and 30 mm are not shown due to their low saturation offsets). Recharge occurs during the second hour of the test. The bar chart is not cumulative; for example, at 2 hours, the saturation offset for the 20 mm simulation is 39%.

The challenge for the protocol is to accurately measure saturation is associated with the calibration. T_{cum} is measured across 15 minutes during which it is assumed the saturation levels remain constant. With the introduction of flowing water, saturation levels will change regardless of the time when the heat pulse begins. Heat transfer not only increases through the wetting front, but additional cooler recharge water following the wetting front removes additional heat not experienced in the static simulations. The length of the heat pulse is also more sensitive at lower water contents due to the shape of the calibration curve where smaller differences in T_{cum} at lower saturations account for larger changes in soil saturation than at higher saturations. For example, the difference in T_{cum} between 10% and 20% saturation is 614 s°C and between 90% and 100% saturation is 1269 s°C. To improve on the accuracy of the protocol, a shorter integration period is tested.

4.4.3. Simulations with 2 Minute Calibrations

A 2 minute heat pulse resulted in a maximum offset of 41% in the 5 mm recharge test, a decrease of 18% compared to the corresponding 15 minute calibration case. The NSE is 0.63 for 30 mm recharge, and 0.57 for 5 mm. The results marginally improve from the 15 minute tests (Figure 4.5). To account for the effect of flowing water removing excessive heat, a new calibration curve was arbitrarily made for the 20 mm/hr recharge event from the previous 2 minute flow calibration. The calibration curve has a stronger relationship and results in an NSE of 0.99.

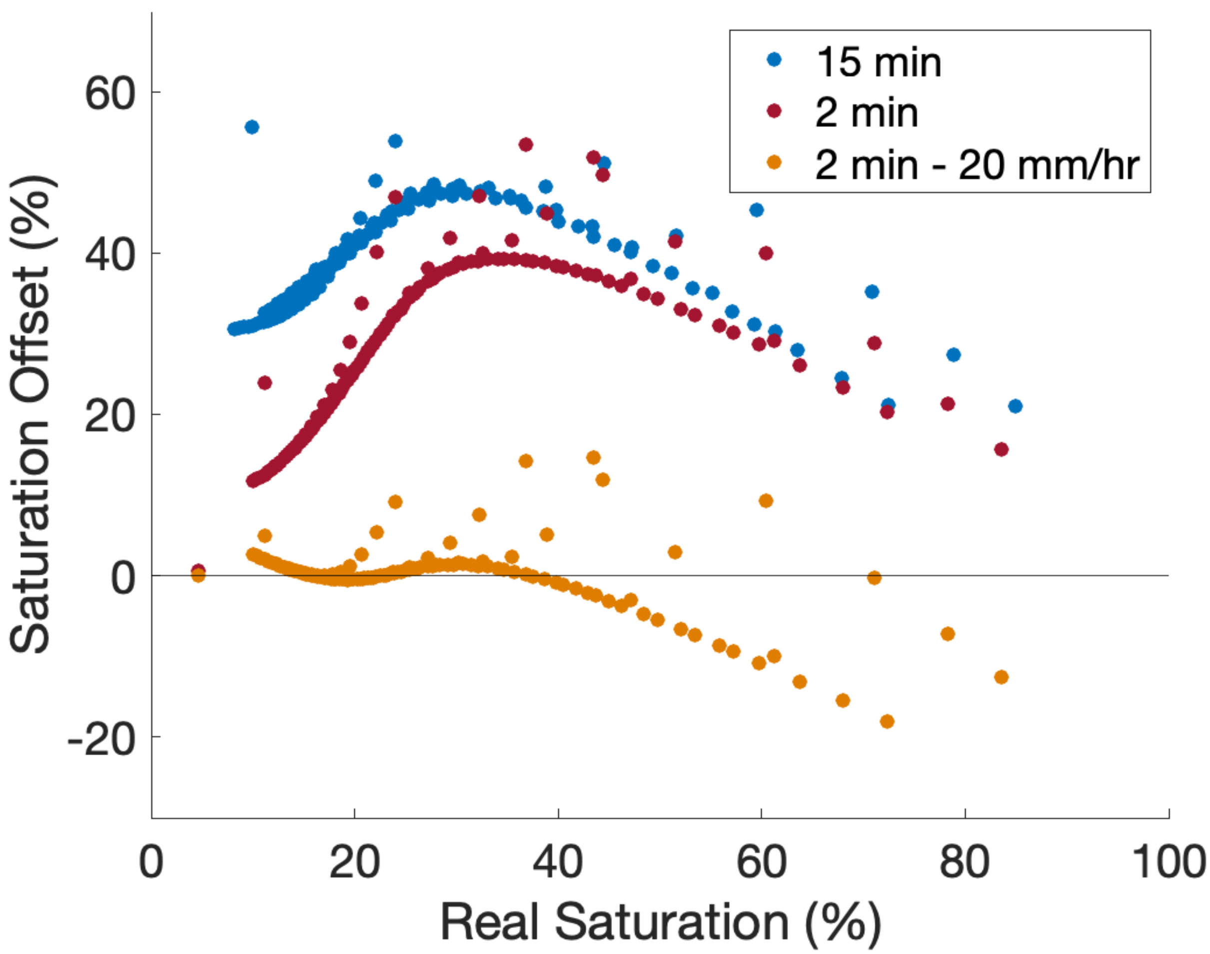

Figure 4.5: Comparison of 15 min, 2 min, and 2 min - 20 mm/hr calibration curves. Real Saturation refers to measurements from the observation node.

However, relationships at higher and lower recharge rates, even with the new calibration curve, are lower with the lowest agreement at 5 mm/hr with an NSE of 0.74 (Figure 4.6). This suggests that in a field test, specific calibrations curves should be built for the specified range of recharge expected at the site. The accuracy of the calibration can decrease if the range of recharge rates is high. In our model, a 50% change in recharge rate can cause the accuracy of the calibration to drift by 25%. The calibration accuracy is lower at higher saturations; the aFO-DTS calibration underestimates saturation at lower recharge rates and overestimates at higher rates.

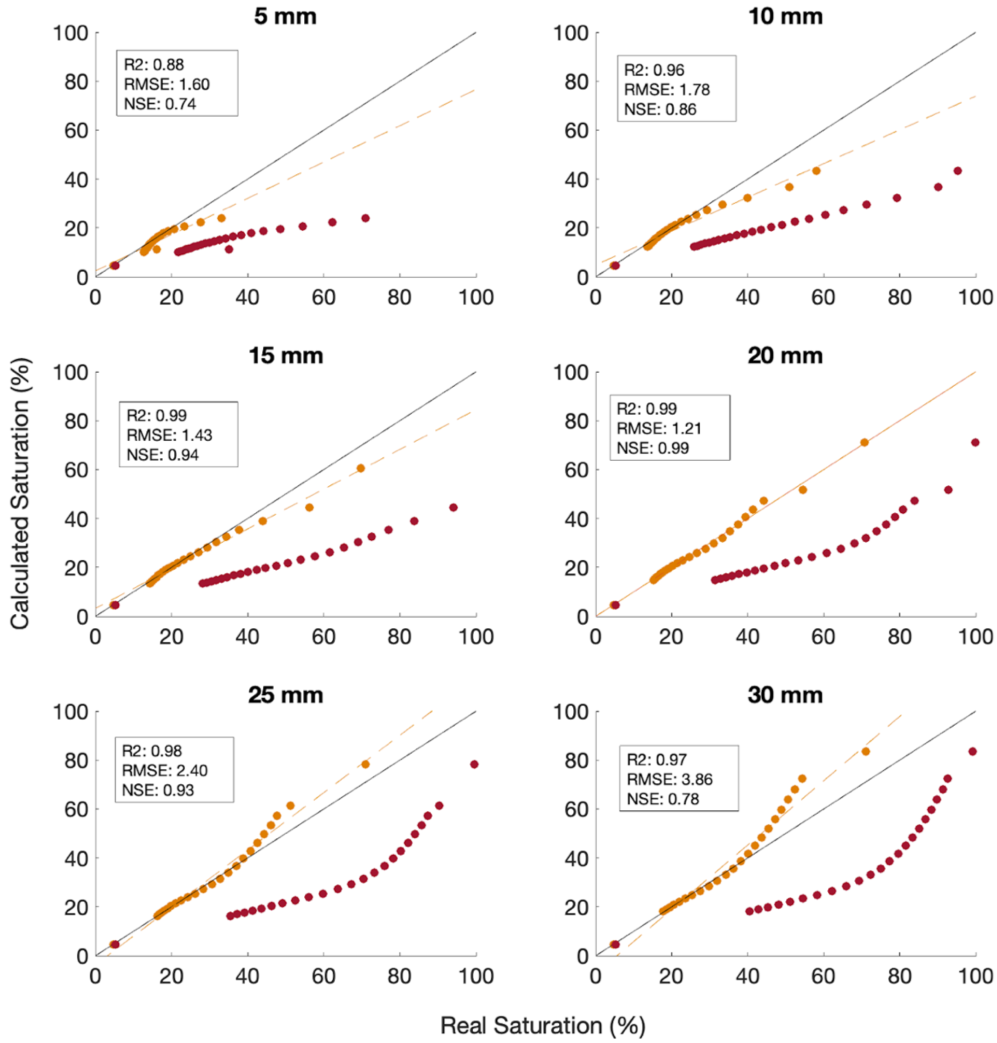

Figure 4.6: Simulations using the 2 min - 20 mm/hr calibration with recharge from 5 mm/h to 30 mm/hr (orange). The 2 min flow calibration (red) is displayed as reference.

4.4.4. Simulations with Variable Recharge and Soil Conditions

The new 2 minute calibration curve optimized for 20 mm/hr (2 min - 20 mm/hr calibration) may present accuracy challenges for different time lengths of recharge, particularly at low recharge durations. To reiterate, the length of recharge in the previous tests is one hour and occurs during the first hour for a 24 hour run. The protocol calibration was tuned to results following the one hour recharge over the course of 24 hours.

We examine the impact of time duration of the recharge event, the accuracy of the protocol calculation decreases when the recharge duration is not one hour. By lowering the recharge time to 40 minutes and to 20 minutes, the NSE is 0.90 and 0.79 respectively (Figure 4.7). Similarly, when increasing the recharge duration to 80 and 100 minutes, the NSE becomes 0.91 and 0.67 (Figure 4.7). The calibration tends to overestimate saturation at lower recharge time lengths and underestimate at higher durations. This could be due to recharge velocity of the watering front. The default recharge rate has a set velocity when the watering front reaches the cable. Deviation from this will result in fresh water removing heating from the medium surrounding the cable.

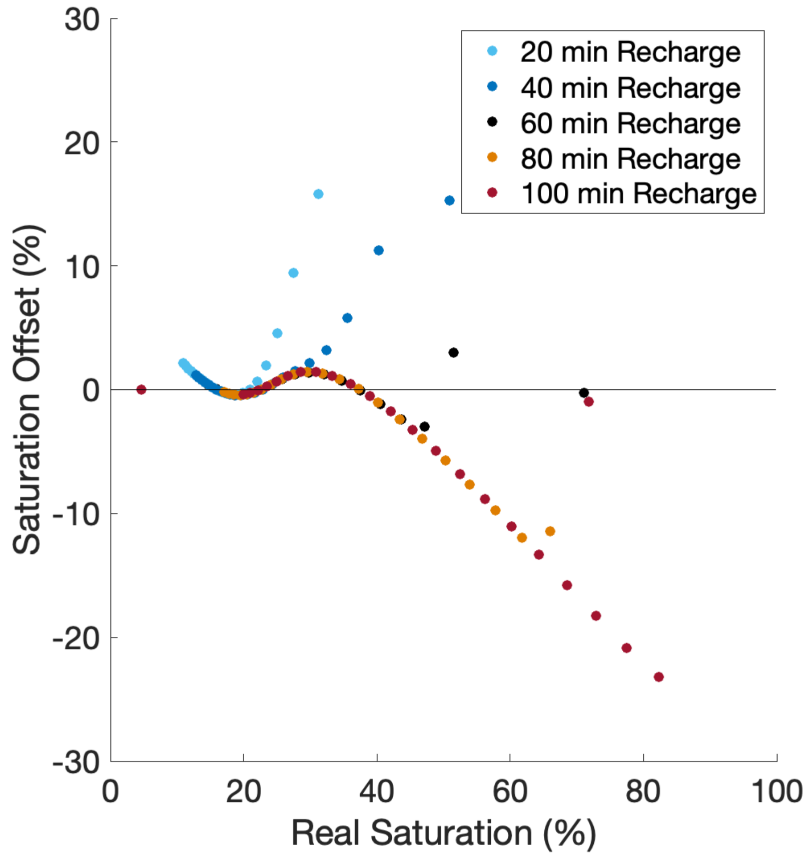

Figure 4.7: Testing the effect of shorter and longer recharge periods on the accuracy of the aFO-DTS protocol with the 2 min - 20 mm/hr calibration curve (while the recharge rate remains 20 mm/hr).

Simulations with variable permeability (see Methods) were used to test the effect of heterogeneity on the protocol. The distribution of heterogeneity follows a gaussian distribution of two orders of magnitude around the default permeability value. Three observation nodes are placed left, right, and top of the cable 0.02 m away from the perimeter of the cable. The recharge rate remained at 20 mm/hr for one hour. The placement of the observation node will measure the soil saturation, in a sense, inaccurately dependent on the permeability surrounding the node. The lowest NSE is 0.29 for an observation node with a permeability of 9.9×10^{-10} m^2 and the highest

NSE is 0.65 at 11.7×10^{-10} m^2. The calibration overestimated the saturation compared to that measured by the observation node in all cases. However, the NSE is 0.99 compared to the average areal saturation of the sand. This suggests that calibration and validation with in-situ probes in heterogeneous soils may be an unsuitable technique if the distribution of the soil is biased, highly heterogeneous, or poorly sorted. A laboratory calibration protocol may be needed in such instances because high variability in testing parameters will need specialized calibration tailored to the soils. Such variability may require a piecewise function dependent on the locale the cable is situated.

During burial of the fiber optic cable, soil texture is altered where the permeability does not represent natural conditions. To remediate soil disturbances, the first active FO-DTS test is often initiated weeks after the burial to allow time for the soil to compact and acclimate to its original conditions. There is evidence of studies using vibratory presses to accelerate these processes (Striegl & Loheide II, 2012). Nevertheless, porosity and permeability structure may be altered with the installation of the fiber optic cable. A lower permeability around the cable can be expected following a higher-than-natural compaction and the inverse is expected at lower compactions.

To test the effect of compaction around the cable, we simulate a 0.0002 m thick zone surrounding the cable with a permeability of 2, 4, and 6 orders of magnitudes lower and higher than the default value of 10^{-12} m^2. The simulation results for higher permeabilities yield a NSE of 0.64, 0.60, and 0.60 respectively (Figure 4.8). The lower permeability range yielded a NSE of 0.46, 0, and 0. The effect of repeated drying cycles can also cause a change in the contact between the cable and soil, and thus the permeability around the fiber optic cable (Sourbeer & Loheide, 2016). This is an important factor to consider as our model shows that a 2 order of magnitude difference in permeability can decrease the accuracy of a protocol by half. Care should be taken to minimize disturbances to the soil during burial and reduce excessive heating in long term field tests.

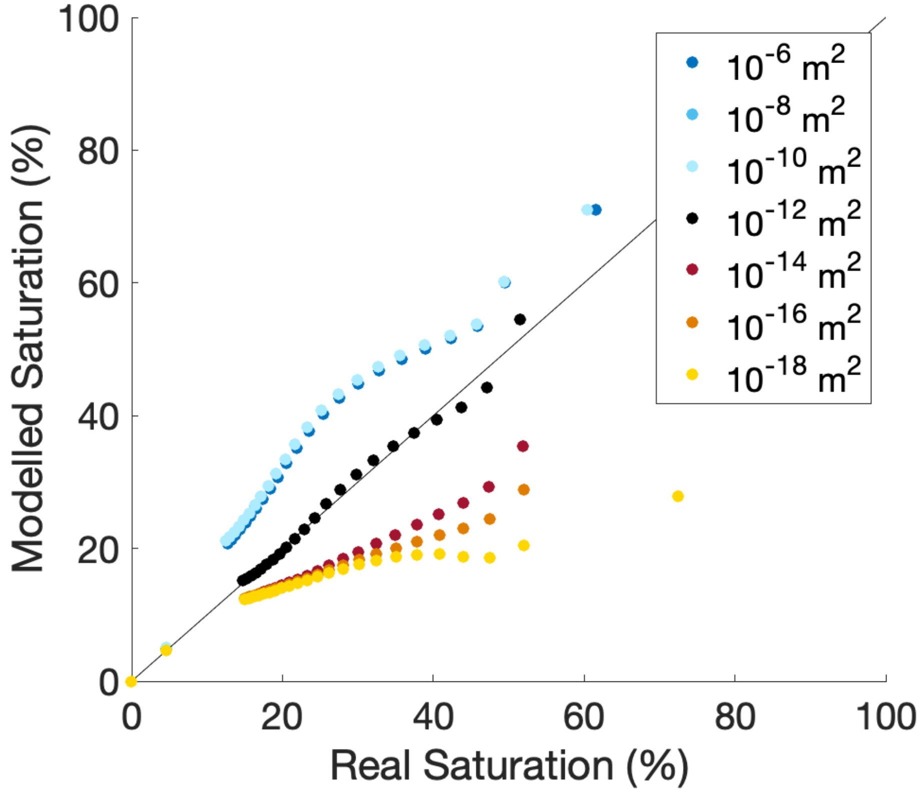

Figure 4.8: The effect on accuracy by unique permeability values surrounding the fiber optic cable relative to the saturation measured by the observation node in default permeability conditions. These simulations test the effect of variability in soil permeability rather than the protocol's ability to account for changes in permeability relative to the observation node's location.

To test the effect of a low permeability layer above the fiber optic cable, three tests were performed with a low permeability layer above the cable with covering all but: above, to the left, and to the right side of the cable. The NSE is 0.77, 0.75, and 0.46 in the center, left, and right tests respectively (Figure 4.9). Note that the observation node is left of the cable in all three tests. The similar NSE values between the above and left cases are expected due to the proximity between the observation node and the cable. The third test diverts water on the right side of the model, where the cable is between the observation node and draining water, shielding the observation node from the water resulting in lower accuracy of aFO-DTS calculation during the timeseries.

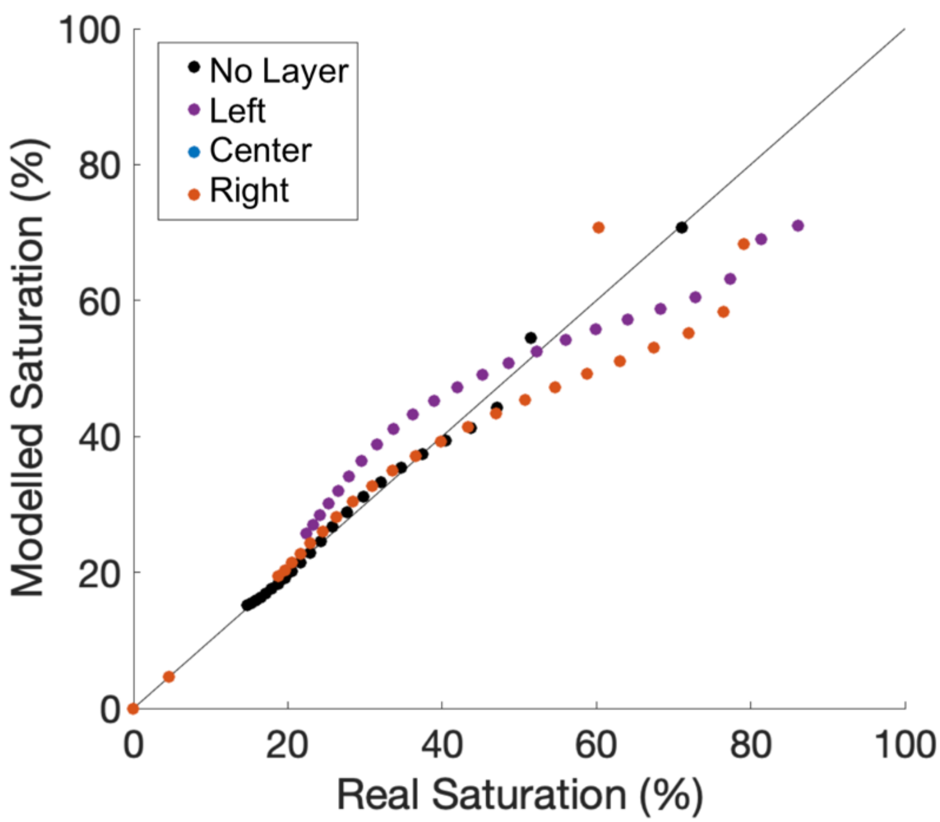

Figure 4.9: A 0.01 m thick horizontal layer of lower permeability is set above the cable through the entire model domain. A gap in the layer with the default permeability value is created left, right, and straight above the cable to force water to flow through this gap. The effect of this low permeability layer is presented. Note, the observation node remains to the left of the cable. The center and left runs produce the similar results.

4.5. Conclusion

A novel distributed calibration model was developed to address the potential errors in using aFO-DTS for measuring soil moisture. The calibration is based on a cubic function of T_{cum} to soil saturation created by simulated aFO-DTS protocols and compared with soil saturation of an adjacent observation node. The general calibration functions return a high agreement between calculated and real saturation. Changing the protocol parameters, such as the duration of active heating and the number of heating cycles, decreased the accuracy of the protocol. Imperfect conditions, such as connection to surrounding porous media, during active heating also decreased the accuracy of the aFO-DTS protocol. Permeability heterogeneity, and the intensity, length, and volume of recharge had a large impact on the predictability of the aFO-DTS.

The soil saturation values were most sensitive to a low permeability layer surrounding the fiber optic cable, and in some cases would reduce NSE to 0. This case highlights the importance of having adequate contact between the cable and soil, and to allow for an appropriate timeframe for soil regeneration following direct cable burial. The challenging aspect of these issues is that they must be addressed by a site-specific case. While disturbances are likely to cause higher permeability adjacent to the cable, lower permeability area adjacent to the fiber optic cable can be caused by hysteresis in fine textured soils. Managing aFO-DTS protocol by lowering the amount and length of heat generated by repeated active heat pulses can reduce this effect of hysteresis.

A calibration method is usually developed for a site-specific soil for application of the aFO-DTS soil saturation method. In principle, a possible alternative calibration procedure would be based on the theory that the calibration curves relating T_{cum} to saturation should have a similar characteristic shape that is scalable to fit a particular soil by few measured T_{cum} - saturation couples. It is similar to what is observed with the relationship between thermal conductivity and saturation. We employed a simple cubic function to model saturation from T_{cum} with a high degree of accuracy. However, following changes to the model parameters, we observe decreases in model accuracy to calculate saturation. Heterogeneity in soils is often accounted for in field-based aFO-DTS studies, however the effect of variable recharge rates and localized micropores are challenging to account for and can be a major source of error in aFO-DTS measurements.

Active FO-DTS measurements offer a very powerful tool to measure distributed soil moisture. Heterogeneity is a fundamental challenge in hydrogeology that is difficult to overcome with isolated point measurements of soil. With the ability to deploy kilometres of cable, aFO-DTS can provide unprecedented measurement capability. But, as our analysis shows, care must be taken in evaluating results. The fundamental challenge is that the method requires a valid calibration that may not be applicable for varying recharge and soil conditions. In particular, calibration may be an issue for settings in which soil moisture is measured in a variety of soil types and/or land cover.

4.6. Acknowledgements

The authors would like to thank the Natural Sciences and Engineering Research Council of Canada (NSERC) and the Ouranos Consortium for financial support. The authors would also like to thank Clifford Voss and Alden Provost (USGS) for technical support with SUTRA.

4.7. Conflict of Interest

The authors declare no conflict of interest.

4.8. References

Amin, A., Zuecco, G., Geris, J., Schwendenmann, L., McDonnell, J. J., Borga, M., & Penna, D. (2020). Depth distribution of soil water sourced by plants at the global scale: A new direct inference approach. *Ecohydrology*, *13*(2), e2177. https://doi.org/10.1002/eco.2177

Benítez-Buelga, J., Rodríguez-Sinobas, L., Calvo, R. S., Gil-Rodríguez, M., Sayde, C., & Selker, J. S. (2016). Calibration of soil moisture sensing with subsurface heated fiber optics using numerical simulation. *Water Resources Research*, *52*(4), 2985–2995. https://doi.org/10.1002/2015WR017897

Bobba, A. G. (1993). Field validation of 'SUTRA' groundwater flow model to Lambton County, Ontario, Canada. *Water Resources Management*, *7*(4), 289–310. https://doi.org/10.1007/BF00872286

Buntebarth, G., & Schopper, J. R. (1998). Experimental and theoretical investigations on the influence of fluids, solids and interactions between them on thermal properties of porous rocks. *Physics and Chemistry of the Earth*, *23*(9), 1141–1146. https://doi.org/10.1016/S0079-1946(98)00142-6

Burns, E. R., Williams, C. F., Ingebritsen, S. E., Voss, C. I., Spane, F. A., & DeAngelo, J. (2015). Understanding heat and groundwater flow through continental flood basalt provinces: Insights gained from alternative models of permeability/depth relationships for the Columbia Plateau, USA. *Geofluids*, *15*(1–2), 120–138. https://doi.org/10.1111/gfl.12095

Burns, Erick R., Bershaw, J., Williams, C. F., Wells, R., Uddenberg, M., Scanlon, D., Cladouhos, T., & van Houten, B. (2020). Using saline or brackish aquifers as reservoirs for thermal energy storage, with example calculations for direct-use heating in the

Portland Basin, Oregon, USA. *Geothermics*, *88*, 101877. https://doi.org/10.1016/j.geothermics.2020.101877

Cao, D., Shi, B., Loheide, S. P., Gong, X., Zhu, H.-H., Wei, G., & Yang, L. (2018). Investigation of the influence of soil moisture on thermal response tests using active distributed temperature sensing (A–DTS) technology. *Energy and Buildings*, *173*, 239–251. https://doi.org/10.1016/j.enbuild.2018.01.022

de Vries, D. A. (1952). A nonstationary method for determining thermal conductivity of soil in situ. *Soil Science*, *73*(2), 83–90.

Deeds, N. E., & Jones, T. L. (2011). *An Assessment of Modeling Approaches to Brackish Aquifers in Texas (IWT BRACS) | Texas Water Development Board*. Texas Water Development Board. https://www.twdb.texas.gov/innovativewater/bracs/projects/aquifermodel/index.asp#04

Dorigo, W. A., Wagner, W., Hohensinn, R., Hahn, S., Paulik, C., Xaver, A., Gruber, A., Drusch, M., Mecklenburg, S., van Oevelen, P., Robock, A., & Jackson, T. (2011). The International Soil Moisture Network: A data hosting facility for global in situ soil moisture measurements. *Hydrology and Earth System Sciences*, *15*(5), 1675–1698. https://doi.org/10.5194/hess-15-1675-2011

Gingerich, S. B., & Voss, C. I. (2005). Three-dimensional variable-density flow simulation of a coastal aquifer in southern Oahu, Hawaii, USA. *Hydrogeology Journal*, *13*(2), 436–450. https://doi.org/10.1007/s10040-004-0371-z

Hausner, M. B. (2010). *Estimating in situ integrated soil moisture content using fiber-optic distributed temperature sensing (DTS) measurements in the field* [Thesis]. https://scholarworks.unr.edu//handle/11714/4282

Kurylyk, B. L., MacQuarrie, K. T. B., & Voss, C. I. (2014). Climate change impacts on the temperature and magnitude of groundwater discharge from shallow, unconfined aquifers. *Water Resources Research*, *50*(4), 3253–3274. https://doi.org/10.1002/2013WR014588

Lamontagne-Hallé, P., McKenzie, J. M., Kurylyk, B. L., & Zipper, S. C. (2018). Changing groundwater discharge dynamics in permafrost regions. *Environmental Research Letters*, *13*(8), 084017. https://doi.org/10.1088/1748-9326/aad404

McKenzie, J. M., & Voss, C. I. (2013). Permafrost thaw in a nested groundwater-flow system. *Hydrogeology Journal*, *21*(1), 299–316. https://doi.org/10.1007/s10040-012-0942-3

Nash, J. E., & Sutcliffe, J. V. (1970). River flow forecasting through conceptual models part I — A discussion of principles. *Journal of Hydrology*, *10*(3), 282–290. https://doi.org/10.1016/0022-1694(70)90255-6

Oki, D. S., Engott, J. A., & Rotzoll, K. (2019). Numerical simulation of groundwater availability in central Moloka‘i, Hawai‘i. In *Numerical simulation of groundwater availability in central Moloka‘i, Hawai‘i* (USGS Numbered Series No. 2019–5150; Scientific Investigations Report, Vols. 2019–5150, p. 95). U.S. Geological Survey. https://doi.org/10.3133/sir20195150

Sayde, C., Buelga, J. B., Rodriguez-Sinobas, L., Khoury, L. E., English, M., Giesen, N. van de, & Selker, J. S. (2014). Mapping variability of soil water content and flux across 1–1000 m scales using the Actively Heated Fiber Optic method. *Water Resources Research*, *50*(9), 7302–7317. https://doi.org/10.1002/2013WR014983

Sayde, C., Gregory, C., Gil-Rodriguez, M., Tufillaro, N., Tyler, S., Giesen, N. van de, English, M., Cuenca, R., & Selker, J. S. (2010). Feasibility of soil moisture monitoring with heated fiber optics. *Water Resources Research*, *46*(6). https://doi.org/10.1029/2009WR007846

Scanlon, B. R., Healy, R. W., & Cook, P. G. (2002). Choosing appropriate techniques for quantifying groundwater recharge. *Hydrogeology Journal*, *10*(1), 18–39. https://doi.org/10.1007/s10040-001-0176-2

Smith, A. J. (2004). Mixed convection and density-dependent seawater circulation in coastal aquifers. *Water Resources Research*, *40*(8). https://doi.org/10.1029/2003WR002977

Sourbeer, J. J., & Loheide, S. P. (2016). Obstacles to long-term soil moisture monitoring with heated distributed temperature sensing. *Hydrological Processes*, *30*(7), 1017–1035. https://doi.org/10.1002/hyp.10615

Striegl, A. M., & Loheide II, S. P. (2012). Heated Distributed Temperature Sensing for Field Scale Soil Moisture Monitoring. *Groundwater*, *50*(3), 340–347. https://doi.org/10.1111/j.1745-6584.2012.00928.x

Tyler, S. W., & Wheatcraft, S. W. (1989). Application of Fractal Mathematics to Soil Water Retention Estimation. *Soil Science Society of America Journal*, *53*(4), 987–996. https://doi.org/10.2136/sssaj1989.03615995005300040001x

Voss, C. I., & Provost, A. M. (2002). SUTRA: A model for 2D or 3D saturated-unsaturated, variable-density ground-water flow with solute or energy transport. In *SUTRA: A model for 2D or 3D saturated-unsaturated, variable-density ground-water flow with solute or energy transport* (USGS Numbered Series No. 2002–4231; Water-Resources Investigations Report, Vols. 2002–4231). U.S. Geological Survey. https://doi.org/10.3133/wri024231

Weiss, J. D. (2003). Using Fiber Optics to Detect Moisture Intrusion into a Landfill Cap Consisting of a Vegetative Soil Barrier. *Journal of the Air & Waste Management Association*, *53*(9), 1130–1148. https://doi.org/10.1080/10473289.2003.10466268

Wigmore, O., Mark, B., McKenzie, J., Baraer, M., & Lautz, L. (2019). Sub-metre mapping of surface soil moisture in proglacial valleys of the tropical Andes using a multispectral unmanned aerial vehicle. *Remote Sensing of Environment*, *222*, 104–118. https://doi.org/10.1016/j.rse.2018.12.024

Woods, J. A., Teubner, M. D., Simmons, C. T., & Narayan, K. A. (2003). Numerical error in groundwater flow and solute transport simulation. *Water Resources Research*, *39*(6). https://doi.org/10.1029/2001WR000586

Wu, R., Martin, V., McKenzie, J., Broda, S., Bussière, B., Aubertin, M., & Kurylyk, B. L. (2020). Laboratory-scale assessment of a capillary barrier using fibre optic distributed temperature sensing (FO-DTS). *Canadian Geotechnical Journal*, *57*(1), 115–126. https://doi.org/10.1139/cgj-2018-0283

Wu, R., Martin, V., McKenzie, J., Broda, S., Bussière, B., & Aubertin, M. (2021). Fiber Optic Protocol to Monitor Water Flow and Moisture Content in a Waste Rock Pile. Groundwater Journal. 10.1111/gwat.13075

Xie, X., Lu, Y., Ren, T., & Horton, R. (2020). Thermal conductivity of mineral soils relates linearly to air-filled porosity. *Soil Science Society of America Journal*, *84*(1), 53–56. https://doi.org/10.1002/saj2.20016

Zipper, S. C., Dallemagne, T., Gleeson, T., Boerman, T. C., & Hartmann, A. (2018). Groundwater Pumping Impacts on Real Stream Networks: Testing the Performance of Simple Management Tools. *Water Resources Research*, *54*(8), 5471–5486. https://doi.org/10.1029/2018WR022707

5. Discussion, Challenges, and Conclusion

The research presented in this thesis elucidates how aFO-DTS can be applied in geoenvironmental soil moisture monitoring. The results of this research demonstrate that aFO-DTS is a feasible and important tool for understanding the processes which control the movement of moisture through waste rock piles, with implications for improved geotechnical designs and helping to decrease contamination, construction, maintenance costs. The outcome of the research project is improved understanding of the movement and distribution of water in a constructed geosystem and is also a technological advancement in geophysical approaches for mine environmental monitoring. In this section I discuss the challenges and opportunities that have arisen through my PhD research and comment on potential future research directions based on each of the three research chapters.

Chapter 2 - The laboratory experiments in Chapter 2 show that aFO-DTS applications allow operator control over the heat signal that is emitted into the soil. This control is a significant advantage over the diurnal heat signal cycle method employed with passive DTS for soil moisture estimation (e.g. Steele-Dunne et al. 2010). In the passive method the diurnal heat signal is significantly attenuated under several conditions (e.g. increasing soil depth, vegetative canopy, cloudy days or other surface energy flux limited systems). Further, as the active method is controllable, it allows for optimization of the heating power duration and intensity for given conditions.

Chapter 3 - For the field experiment, the T_{cum} calibration curve method that relates aFO-DTS to soil moisture content was obtained in a laboratory experiment. Waste rock and sand was packed to the observed field bulk density in a 0.8 m diameter soil column. This operation was tedious and time consuming as it had to cover the whole range of soil moisture conditions and the soil column was saturated, drained for several days, and then left drying over several weeks.

The most direct, if time intensive, method to properly calibrate the aFO-DTS method is to measure the thermal conductivity of a given soil over the full range of soil moisture conditions. Heat transport models could then be optimized to generate a calibration curve relating T_{cum} to soil moisture content for a given fiber optic cable design and operating conditions. Nevertheless, measuring thermal properties of soil over the full range of soil water content is a significant challenge in terms of time and effort required to complete such a procedure.

The results of the field testing show that aFO-DTS method can measure a complex spatial pattern of soil moisture content and fluxes. Heterogeneous spatial patterns are challenging to capture using few measurements from *in-situ* point scale moisture sensors. Larger scale measurements techniques, such as remote sensing, might be able to provide changes in soil moisture content with a reasonable accuracy. Nevertheless, they will fail to capture important processes at the meter scale observation required for this experiment. Monitoring such small-scale processes are of particular importance in mine waste (tailings and waste rock piles). The results showed that changes in soil moisture content can be measured and monitored across a range of values (ranging from dry to saturated conditions) that is significantly larger than the <0.06 range m^3/m^3 reported by Weiss (2003) and more informative than the qualitative *dry*, *wet* or *saturated* assessment reported by Perzlmaier et al. (2004; 2006).

Chapter 4 – Analysis of potential errors or methodological problems related to subsurface heterogeneity and calibration method using a parametric modeling approach. Heterogeneity in soils can be accounted for in field-based aFO-DTS studies, however the effect of variable recharge rates and localized macropores are challenging to account for and may be a major source of error in aFO-DTS measurements. The calibration function returns a high agreement between calculated and real saturation. However, changing the protocol parameters, such as the duration of active heating and the number of heating cycles, decreased the accuracy of the protocol if the calibration method is not recalculated. Imperfect conditions, such as connection to surrounding porous media during active heating also decreased the accuracy of the aFO-DTS protocol. Permeability heterogeneity, and the intensity, length, and volume of recharge also affected the simulated aFO-DTS results.

The calibration of the aFO-DTS method remains challenging. In theory, curves relating T_{cum} to soil moisture content should have the same basic shape if the recharge rate in the given environment remains constant for a given soil medium. This consistency suggests that calibration curves for different recharge rates could be scaled from one reference curve using as few as two field measurements. Further inquiry and field demonstration of this methodology is for future full-scale research.

In aFO-DTS protocol, the errors in soil moisture content calculations due to instrumentation and operation can be reduced by increasing the signal to noise ratio of temperature readings. The implementation of the DTS measurements can be specifically optimized to meet the resolution requirements through the applied power, DTS temperature reading error per temperature reading cycle, the spatial resolution and sampling interval of the temperature readings, and the heat pulse duration. Based on the finding of my research, future studies should focus on defining the constraining values of these parameters to further expand the applicability of the aFO-DTS method for measuring soil moisture.

6. References

Aubertin, M., Bussière, B., and Bernier, L. (2002). Environnement et gestion des rejets miniers [CD-ROM] Montréal, Québec, Les Presses Internationales de Polytechnique

Aubertin, M., Fala, O., Bussière, B., Martin, V., Campos, D., Gamache-Rochette, A., Chouteau, M., and Chapuis, R.P. (2002). Analyse des écoulements de l'eau en conditions non saturées dans les haldes à stériles, in Défis et perspectives: Symposium 2002 sur l'Environnement et les Mines, [CD-ROM] Rouyn-Noranda, Canada

Aubertin, M., Cifuentes, E., Apithy, S. A., Bussière, B., Molson, J., and Chapuis, R. P. (2009). Analyses of water diversion along inclined covers with capillary barrier effects. Canadian Geotechnical Journal, 46(10), 1146-1164. doi:10.1139/t09-050

Aubertin, M. (2013). Waste rock disposal to improve the geotechnical and geochemical stability of piles. In Proceedings of the world mining congress, Montreal, Canada.

Barry-Macaulay, D., Bouazza, A., Wang, B., and Singh, R. M. (2015). Evaluation of soil thermal conductivity models. Canadian Geotechnical Journal, 52(11), 1892-1900.

Bense, V. F., Read, T., Bour, O., Borgne, T. L., Coleman, T., Krause, S., Selker, J. S. (2016). Distributed Temperature Sensing as a downhole tool in hydrogeology. Water Resources Research, 52(12), 9259-9273. doi:10.1002/2016wr018869

Benítez-Buelga, J., Sayde, C., Rodríguez-Sinobas, L., and Selker, J. S. (2014). Heated Fiber Optic Distributed Temperature Sensing: A Dual-Probe Heat-Pulse Approach. Vadose Zone Journal, 13(11).

Bilskie, J. R. (1994). Dual probe methods for determining soil thermal properties: Numerical and laboratory study

Bonan, G. B. (2008). Forests and Climate Change: Forcings, Feedbacks, and the Climate Benefits of Forests. Science, 320(5882), 1444-1449. doi:10.1126/science.1155121z

Bristow, K.L., G.J. Kluitenberg, and R. Horton. (1994). Measurement of soil thermal properties with a dual-probe heat-pulse technique. Soil Sci. Soc. Am. J. 58:1288–1294

Briggs, M. A., Lautz, L. K., & McKenzie, J. M. (2012). A comparison of fiber-optic distributed temperature sensing to traditional methods of evaluating groundwater inflow to streams. Hydrological Processes, 26(9), 1277-1290.

Broda, S., Sayde, C., J. Selker, M. Aubertin, and D. Blessent (2013), Using temperature as a tracer for analyzing the response of a capillary barrier in waste rock, paper presented at GeoMontreal 2013: Geosciences for Sustainability, 66th CGS Conference, Montreal, Que.

Bussière, B., Aubertin, M., and Chapuis, R. P. (2003). The behavior of inclined covers used as oxygen barriers. Canadian Geotechnical Journal, 40(3), 512-535. doi:10.1139/t03-001

Campbell, Gaylon & Calissendorff, C and& Williams, J.H.. (1991). Probe for Measuring Soil Specific Heat Using A Heat-Pulse Method. Soil Science Society of America Journal. 55. 291-293.

Carslaw, H. S., and Jaeger, J. C. (1959). Conduction of heat in solids. Oxford: Clarendon Press

Chi, X., Amos, R. T., Stastna, M., Blowes, D. W., Sego, D. C., & Smith, L. (2013). The Diavik Waste Rock Project: Implications of wind-induced gas transport. Applied Geochemistry, 36, 246-255. doi:10.1016/j.apgeochem.2012.10.015

Chung, S.-O., and R. Horton (1987), Soil heat and water flow with a partial surface mulch, Water Resources. Res., 23(12), 2175–2186

Ciocca, F., Lunati, I., Giesen, N. V., and Parlange, M. B. (2012). Heated fiber optic for Distributed Soil-Moisture Measurements: A Lysimeter Experiment. Vadose Zone Journal, 11(4), 0. doi:10.2136/vzj2011.0199

Côté, Jean & Konrad, Jean-Marie. (2005). A generalized thermal conductivity model for soils and construction materials. Canadian Geotechnical Journal. 42. 443-458. 10.1139/t04-106.

de Vries D.A.: Thermal properties of soil. In: Physics of Plant Environment (ed. W.R. van Wijk) North-Holland, Amsterdam, 210-235, 1963

Dobriyal, P., Qureshi, A., Badola, R., and Hussain, S. A. (2012). A review of the methods available for estimating soil moisture and its implications for water resource management. Journal of Hydrology, 458, 110-117.

Dong, J., Agliata, R., Steele-Dunne, S., Hoes, O., Bogaard, T., Greco, R., & van de Giesen, N. (2017). The Impacts of Heating Strategy on Soil Moisture Estimation Using Actively Heated Fiber Optics. Sensors (Basel, Switzerland), 17(9), 2102. http://doi.org/10.3390/s17092102

Fala, O., Aubertin, M., Bussière, B., and Chapuis, R.P . (2002). Analyses numériques des écoulements non saturés dans des haldes à stériles, in 55th Canadian Geotechnical Conference - 3rd Joint International Association of Hydrogeologists-Canadian National Chapter-Canadian Geotechnical Society (IAH-CNC/CGS) Conference: Ground and Water: Theory to Practice, [CD-ROM] Niagara Falls, Canada.

Gil-Rodríguez, M., Rodríguez-Sinobas, L., Benítez-Buelga, J., and Sánchez-Calvo, R. (2013). Application of active heat pulse method with fiber optic temperature sensing for estimation of wetting bulbs and water distribution in drip emitters. Agricultural Water Management, 120, 72-78. doi:10.1016/j.agwat.2012.10.012

Grattan, K. T. V., and Sun, T. (2000). Fiber optic sensor technology: An overview. Sensors and Actuators, A: Physical, 82(1), 40-61. doi:10.1016/S0924-4247(99)00368-4

Halloran, L. J., Rau, G. C., & Andersen, M. S. (2016). Heat as a tracer to quantify processes and properties in the vadose zone: A review. Earth-Science Reviews, 159, 358-373. doi:10.1016/j.earscirev.2016.06.009

Herasymuik, G. M. (1996). Hydrogeology of a sulfide waste rock dump, Master's Thesis in Civil Engineering, University of Saskatchewan, 184 pp

Johansen, O. (1975). Thermal conductivity of soils. Ph.D. thesis. Trondheim, Norway (CRREL Draft Translation 637, 1977) ADA 044002

Kluitenberg, G. J., Ham, J. M., and Bristow, K. L. (1993). Error Analysis of the Heat Pulse Method for Measuring Soil Volumetric Heat Capacity. Soil Science Society of America Journal. Soil Science Society of America, 57(6), 1444.

Kluitenber, G. J. (2002). Thermal Conductivity. In: J.H. Dane and G.C. Topp, editors, Methods of soil analysis. Part 4. Physical methods. SSSA Book Ser. 5. SSSA, Madison WI. P. 1201-1209.

Lu, S., Ren, T., Gong, Y., and Horton, R. (2007). An Improved Model for Predicting Soil Thermal Conductivity from Water Content at Room Temperature. Soil Science Society of America Journal,71(1), 8. doi:10.2136/sssaj2006.0041

Martin V., Aubertin, M., Zhan, J., Bussière, B., and Chapuis, R.P. (2005). An investigation into the hydrological behaviour of exposed and covered waste rock dumps. Society of Manufacturing Engineers Transactions 318: 139-146

Morin, K.A.; Gerencher, E.; Jones; C.E., and Konasewich, D.E., (1991). Critical literature review of acid drainage from waste rock, MEND Report 1.11.1

Newman, L.L., Herasymiuk, G.M., Barbour, S.L., Fredlund, D.G., and Smith, T. (1997). The hydrogeology of waste rock dumps and a mechanism for unsaturated preferential flow, in Proceedings ICARD 1997, pp. 551-564

Nield, D. A., and Bejan, A. (1999). Convection in porous media. doi:10.1007/978-1-4757-3033-3

Perzlmaier, S., Aufleger M., and Conrad, M., (2004). Distributed fiber optic temperature measurements in hydraulic engineering—Prospects of the heat-up method, in Proceedings of the 72nd Annual Meeting—Workshop on Dam Safety Problems and Solutions-Sharing Experience, p. 31, Korean Natl. Comm. on Large Dams, Seoul

Perzlmaier, S., Straßer, K. H., Strobl, T., & Augleger, M. (2006). Integral seepage monitoring on open channel embankment dams by the DFOT heat pulse method. In Transactions of the international congress on large dams (Vol. 22, No. 3, p. 145).

Sayde, C., Gregory, C., Gil-Rodriguez, M., Tufillaro, N., Tyler, S., Giesen, N. V., and Selker, J. S. (2010). Feasibility of soil moisture monitoring with heated fiber optics. Water Resources Research, 46(6). doi:10.1029/2009wr007846

Sayde, C., Buelga, J.B., Rodriguez-Sinobas, L., Khoury, L.E., English, M., Giesen, N.V., and Selker, J. S. (2014). Mapping variability of soil water content and flux across 1-1000 m scales using the Actively Heated Fiber Optic method. Water Resources Research, 50(9), 7302-7317. doi:10.1002/2013wr014983

Striegl, A.M. and Loheide II, S.P. (2012), Heated Distributed Temperature Sensing for Field Scale Soil Moisture Monitoring. Ground Water, 50: 340–347. doi:10.1111/j.1745-6584.2012.00928.x

Van Genuchten, M. T. (1980). A closed-form equation for predicting the hydraulic conductivity of unsaturated soils. *Soil Science Society of America Journal, 44*(5), 892-898. doi:10.2136/sssaj1980.03615995004400050002x

Weiss, J.D. (2003). Using Fiber Optics to Detect Moisture Intrusion into a Landfill Cap Consisting of a Vegetative Soil Barrier. Journal of the Air & Waste Management Association, 53(9), 1130-1148. doi:10.1080/10473289.2003.10466268

Wilson, J.A., Wilson, G W., and Fredlund, D.G. (2000). Numerical modeling of vertical and inclined waste rock layers, in Proceedings of 5th International Conference on Acid Rock Drainage. Denver, Colorado, pp. 257-266

Appendix:

Following is the code used for analyzing the DTS data. The code is written for MATLAB and runs on version 2016B. There are two sections of code. The first is what was used for processing the results from the laboratory experiment (Chapter 2), and second was used for processing the results from the field experiment (Chapter 3).

DTS Laboratory Code:

```
%This function outputs a series of figures to interpret temperature, mean
%temperature, and the difference in temperature between the two adjacent
%cable segments (inbound/outbound). The function calculates the length of
%segment 2 (inbound) to be identical to segment 1 (outbound).%have to know
%where does the segment 1 and segment 2 starts, if not the function will
%not give the right variables.
%Input Definitions:
%dts_data = The Data Structure (raw data)
%start_seg1 = Start of outbound cable segment for helix of interest
%end_seg1 = End of outbound cable segment for helix of interest
%start_seg2 = Start of inbound cable segment for helix of interest

%The length of each helix must be determined and inputted manually.
%Anything requiring manually adjustment is indicated with SET MANUALLY
note
%% Location Finder
start_seg1=65;
end_seg1=105;
start_seg2=156;
end_seg2=start_seg2+(end_seg1-start_seg1); %Calculate the end segment 2
(inbound)
loc_start_seg1=find(dts_data.x==start_seg1); %Finds location of the
outbound start
loc_end_seg1=find(dts_data.x==end_seg1); %Finds location of the outbound
end
loc_start_seg2=find(dts_data.x==start_seg2); %Finds location of the
inbound start
loc_end_seg2=find(dts_data.x==end_seg2); %Finds location of the inbound
end

%% Temperature Data for Segment
%Calls every time step within the bounds defined above
seg1_data=dts_data.offset_temp(:,loc_start_seg1:loc_end_seg1);
seg2_data=dts_data.offset_temp(:,loc_start_seg2:loc_end_seg2);
%% Mirror Segment 2?
%If the cable is continuous and folds back on itself, to align the data it
%must be mirrored. Manually input whether segment needs to be mirrored.
mirrorcheck = 1; %(0 = Not Mirrored, 1 = Mirrored) SET MANUALLY.
```

```
if mirrorcheck == 1
    seg2_data_m = fliplr(seg2_data);
end
if mirrorcheck == 0
    seg2_data_m = seg2_data; %Note: Variable will retain "_m" suffix in
subsequent code, even if mirrorcheck=0
end
%% Mean Differencesx=
mean1=mean(seg1_data);
mean2=mean(seg2_data_m);
meandiff = (mean1-mean2);
delta_T=-(seg2_data_m-seg1_data); %Temperature difference between
inbound/outbound
%% Segment Data Structure
DeltaT_Overlay.notes_n= 'Updated data structure'; %Identifying Notes
DeltaT_Overlay.juliandate=dts_data.juliandate; %Time
DeltaT_Overlay.k=dts_data.k; %Measurement #
DeltaT_Overlay.seg1_x=dts_data.x(loc_start_seg1:loc_end_seg1); %Segment 1
(outbound) length
DeltaT_Overlay.seg2_x=dts_data.x(loc_start_seg2:loc_end_seg2); %Segment 2
(inbound) length
DeltaT_Overlay.segment1=seg1_data; %Segment 1 (outbound) data
DeltaT_Overlay.segment2=seg2_data_m; %Segment 2 (inbound) data
DeltaT_Overlay.delta_T=delta_T; %Temperature difference between segments
DeltaT_Overlay.delta_Tm=meandiff; %Mean temperature difference between
cables
DeltaT_Overlay.Tseg1=mean1; %Mean temperature of segment 1 (outbound)
DeltaT_Overlay.Tseg2=mean2; %Mean temperature of segment 2 (inbound)

%helix 1
helix1_start1=find(dts_data.x==65);
helix1_end1=find(dts_data.x==72.5);
helix1_start2=find(dts_data.x==188.5);
helix1_end2=find(dts_data.x==196);
helix1_temp1=fliplr(dts_data.offset_temp(:,helix1_start1:helix1_end1));
helix1_temp2=(dts_data.offset_temp(:,helix1_start2:helix1_end2));
helix1_delta_t=transpose(helix1_temp1-helix1_temp2);
helix1_length=(0:0.5:7.5)*100;
helix1_rad=15;
helix1_depth=8.6*(helix1_length/(2*pi*helix1_rad));

%helix 2
helix2_start1=find(dts_data.x==72.5);
helix2_end1=find(dts_data.x==86);
helix2_start2=find(dts_data.x==175);
helix2_end2=find(dts_data.x==188.5);
helix2_temp1=(dts_data.offset_temp(:,helix2_start1:helix2_end1));
helix2_temp2=fliplr(dts_data.offset_temp(:,helix2_start2:helix2_end2));
helix2_delta_t=transpose(helix2_temp1-helix2_temp2);
helix2_length=(0:0.5:13.5)*100;
helix2_rad=25;
helix2_depth=8.6*(helix2_length/(2*pi*helix2_rad));

%helix3
```

```
helix3_start1=find(dts_data.x==86);
helix3_end1=find(dts_data.x==105);
helix3_start2=find(dts_data.x==158);
helix3_end2=find(dts_data.x==177);
helix3_temp1=fliplr(dts_data.offset_temp(:,helix3_start1:helix3_end1));
helix3_temp2=dts_data.offset_temp(:,helix3_start2:helix3_end2);
helix3_delta_t=(helix3_temp1)'-(helix3_temp2)';
helix3_length=(0:0.5:19)*100;
helix3_rad=35;
helix3_depth=8.6*(helix3_length/(2*pi*helix3_rad));
save('helices_temp');

figure;
subplot(3,1,1);
pcolor(DeltaT_Overlay.juliandate,flipud(helix3_depth),helix3_temp2');
shading interp;
datetick('x');
set(gca,'Ydir','reverse','layer','top');
caxis([min(min(helix3_temp1)) max(max(helix3_temp1))]);
caxis ([25 70]);
title('Heated Cable Temperature Variation in Helix 3');
colorbar;

subplot(3,1,2);
pcolor(DeltaT_Overlay.juliandate,flipud(helix3_depth),helix3_temp1');
shading interp;
datetick('x');
set(gca,'Ydir','reverse','layer','top');
%caxis([min(min(helix3_temp1)) max(max(helix3_temp1))]);
caxis ([25 60]);
title('Unheated Cable Temperature Variation in Helix 3');
ylabel('Depth (cm)');
colorbar;

subplot(3,1,3);
pcolor(DeltaT_Overlay.juliandate,helix3_depth,helix3_delta_t);
shading interp;
datetick('x');
set(gca,'Ydir','reverse','layer','top');
%caxis([min(min(helix3_delta_t)) max(max(helix3_delta_t))]);
caxis ([-40 0]);
title('Temperature Differences in Helix 3');
colorbar;



% subplot(3,3,2);
% pcolor(DeltaT_Overlay.juliandate,flipud(helix2_depth), helix2_temp2');
% shading interp;
% datetick('x');
% set(gca,'Ydir','reverse','layer','top');
% %caxis([min(min(helix2_temp1)) max(max(helix2_temp1))]);
% caxis ([25 60]);
% title('Heated Cable Temperature Variation in Helix 2');
```

```
% colorbar;
%
% subplot(3,3,5);
% pcolor(DeltaT_Overlay.juliandate,flipud(helix2_depth), helix2_temp1');
% shading interp;
% datetick('x');
% set(gca,'Ydir','reverse','layer','top');
% %caxis([min(min(helix2_temp1)) max(max(helix2_temp1))]);
% caxis ([25 60]);
% title('Unheated Cable Temperature Variation in Helix 2');
% colorbar;
%
% subplot(3,3,8);
% pcolor(DeltaT_Overlay.juliandate,helix2_depth,helix2_delta_t);
% shading interp;
% datetick('x');
% set(gca,'Ydir','reverse','layer','top');
% %caxis([min(min(helix2_delta_t)) max(max(helix2_delta_t))]);
% caxis ([-10 0]);
% title('Temperature Differences in Helix 2');
% xlabel('Time');
% colorbar;
%
% subplot(3,3,3);
% pcolor(DeltaT_Overlay.juliandate,flipud(helix1_depth), helix1_temp2');
% shading interp;
% datetick('x');
% set(gca,'Ydir','reverse','layer','top');
% %caxis([min(min(helix1_temp1)) max(max(helix1_temp1))]);
% caxis ([25 60]);
% title('Heated Cable Temperature Variation in Helix 1');
% colorbar;
%
% subplot(3,3,6);
% pcolor(DeltaT_Overlay.juliandate,flipud(helix1_depth), helix1_temp1');
% shading interp;
% datetick('x');
% set(gca,'Ydir','reverse','layer','top');
% %caxis([min(min(helix1_temp1)) max(max(helix1_temp1))]);
% caxis ([25 60]);
% title('Unheated Cable Temperature Variation in Helix 1');
% colorbar;
%
% subplot(3,3,9);
% pcolor(DeltaT_Overlay.juliandate,helix1_depth,helix1_delta_t);
% shading interp;
% datetick('x');
% set(gca,'Ydir','reverse','layer','top');
% %caxis([min(min(helix1_delta_t)) max(max(helix1_delta_t))]);
% caxis ([-10 0]);
% title('Temperature Differences in Helix 1');
% colorbar;
% colormap(jet)
```

```
colormap(subplot(3,1,3),bone);%colormap(subplot(3,3,8),bone);colormap(subp
lot(3,3,9),bone);
%
% %saveas(gcf,'z.png')
```

DTS Field Work Code:

```
function corrected_dts_structure = DTS_bath_correction(dts,
cold_bath_time, cold_bath_temp, warm_bath_time,
warm_bath_temp,lys,plot_data, x1, x2, y1, y2, z1, z2)
%
% function [calibrated_DTS_data_structure] = two_bath_correction(dts,
x_bath_time, x_bath_temp, x1, x2, y_bath_time, y_bath_temp, y1, y2,
plot_data);
%
% Function to calculate offset correction for DTS for 1 temperature bath
%       dts = data structure with uncorrected DTS data
%       x_bath_time = time series for x cold bath temperatures (units in
days)
%       x_bath_temp = temperature of x cold temperature bath
(corresponding to bath_time
%       x1 = distance along dts cable to start of x bath (units in m)
%       x2 = distance along dts cable to end of x bath (units in m)
%       y_bath_time = time series for y warm bath temperatures (units in
days)
%       y_bath_temp = temperature of y warm temperature bath
(corresponding to bath_time
%       y1 = distance along dts cable to start of y bath (units in m)
%       y2 = distance along dts cable to end of y bath (units in m)
%       z1 = distnace along dts cable to start of the last cold bath
%       z2 = distnace along dts cable to end of the last cold bath
%       transit = 1 do the transit correction, =0 if do not want the
%       transit correction.
%       lys= put 1 if it is the lysimeter layer and put 0 if it is the
%       surface layer, put 2 if you want the whole data set with the bath
%       and the exit points
%       plot_data = if 1 then plot summary graph. If blank or 0 then
nothing
%       surface and waste layer is the same.
%       for lys first cold bath = 24-32, warm bath = 9-19, and last cold
%       bath is 790-798.
%       for waste first cold bath = 31-46, warm bath = 12-26, and last
cold
%       bath is 1231-1246.
%       put z1 and z2 = nan if the third cold bath is not needed.

%%
if nargin == 7
    if lys==1
        x1=25;
        x2=27;
```

```
        y1=10;
        y2=16;
        z1=790;
        z2=798;
        transit = 0;
    elseif lys==0
        x1=31;
        x2=45;
        y1=13;
        y2=25;
        z1=622;
        z2=630;
        transit = 0;
    elseif lys == 2 %Set to helix configuration
        x1=8;
        x2=24;
        y1=36;
        y2=53;
        z1=110;
        z2=130;
        transit = 0;
    end
else if nargin == 13
        transit = 0;
    end
end

%same as offset correction, interpolate measured calibration bath data for
%same times as the dts file
m=length(dts.juliandate);
bath_temp_interp = zeros(m,2);
bath_temp_interp(:,1) =
interp1(cold_bath_time,cold_bath_temp,dts.juliandate);
bath_temp_interp(:,2)=interp1(warm_bath_time,warm_bath_temp,dts.juliandate
);

%sames as offset correct, added y values

[~,start_location_x]=min(abs(dts.x-x1));
[~,end_location_x]=min(abs(dts.x-x2));

[~,start_location_y]=min(abs(dts.x-y1));
[~,end_location_y]=min(abs(dts.x-y2));

[~,start_location_z]=min(abs(dts.x-z1));
[~,end_location_z]=min(abs(dts.x-z2));

% calculate mean dts temp between distance 1 and 2 for both baths
dts_bath=zeros(length(dts.k),2);
for i = 1:length(dts.k)
    dts_bath(i,1)=mean(dts.tempdata(i,start_location_x:end_location_x)); %
1 is always cold bath
    dts_bath(i,2)= mean(dts.tempdata(i,start_location_y:end_location_y));
%2 is always warm bath
```

```
end
%calculate offset
offset_correction=zeros(length(dts.k),2);
offset_correction(:,1)=dts_bath(:,1)-(bath_temp_interp(:,1));
offset_correction(:,2)=dts_bath(:,2)-(bath_temp_interp(:,2));

%apply offset to each step
dts_tempdata_corrected_cold=zeros(length(dts.k),length(dts.l));
dts_tempdata_corrected_warm=zeros(length(dts.k),length(dts.l));

for i=1:length(dts.k)
    dts_tempdata_corrected_cold(i,:)=dts.tempdata(i,:)-
offset_correction(i,1);
    dts_tempdata_corrected_warm(i,:)=dts.tempdata(i,:)-
offset_correction(i,2);
end

test=zeros(length(dts.k),2);
for i=1:length(dts.k)

test(i,1)=mean(dts_tempdata_corrected_cold(i,start_location_x:end_location
_x)); % 1temperature data with offset correct for each time step

test(i,2)=mean(dts_tempdata_corrected_warm(i,start_location_y:end_location
_y));
end
% linear curve fitting for each time step of the tempdata.
% using test (cold and warm bath) as the 2 points anchor.
p1=zeros(size(test));
fit1=zeros(size(test));
slope=zeros(length(test),1);
intercept=zeros(length(test),1);
for i = 1:length(test)
    p1(i,:)=polyfit(dts_bath(i,:),test(i,:),1);
    fit1(i,:)=polyval(p1(i,:),dts_bath(i,:));
    slope(i)=p1(i,1);
    intercept(i)=p1(i,2);
end

%Show the corrected tempdata in a graph of distance vs tempdata.
temp_corrected=zeros(size(dts.tempdata));
[m,n]=size(dts.tempdata);
for j=1:n
    for k=1:m
        temp_corrected(k,j)=slope(k).*dts.tempdata(k,j)+intercept(k);
    end
end

%Transit correction --? using only the cold bath (mainly for the waste
%rock pile and not for the lysimeter.
%The transit correct add an unwanted intercept on the first cold bath,
%rendering it a bit above the correct temperature of 0C. Thus, adding
%an error on the overall curve.
if transit==1
```

```
    dist1=(start_location_x+end_location_x)/2; %get the middle point of
the first cold bath
    dist2=(start_location_z+end_location_z)/2; %get the middle point of
the last cold bath
    mid_coldbath=[dts.x(dist1) dts.x(dist2)];
    mean_coldbath=zeros(length(dts.k),2); %mean coldbath is the mean
tempdata of the first coldbath of each timestep.

    for i = 1:length(dts.k)

mean_coldbath(i,1)=mean(temp_corrected(i,start_location_x:end_location_x))
;
        mean_coldbath(i,2)=
mean(temp_corrected(i,start_location_z:end_location_z));
    end
    %curve fitting --> each time step has its own curve.
    p2=zeros(size(mean_coldbath));
    fit2=zeros(size(mean_coldbath));
    slope2=zeros(length(mean_coldbath),1);
    intercept2=zeros(length(mean_coldbath),1);
    for i = 1:length(mean_coldbath)
        p2(i,:)=polyfit(mid_coldbath,mean_coldbath(i,:),1);
        fit2(i,:)=polyval(p2(i,:),mid_coldbath);
        slope2(i)=p2(i,1);
        intercept2(i)=p2(i,2);
    end

    transit_correction=zeros(size(dts.tempdata));
    [m,n]=size(dts.tempdata);
    for j=1:n
        for k=1:m
            transit_correction(k,j)=slope2(k).* dts.x(1,j)+intercept2(k);
        end
    end
else if transit==0
        transit_correction=nan;
    end
end

%delta T of cold baths
transit_corrected=temp_corrected-transit_correction;
delta_temp_transit = zeros(length(dts.k),3);
for i = 1:length(dts.k)
    delta_temp_transit(i,1)=
mean(transit_corrected(i,start_location_x:end_location_x))-
mean(transit_corrected(i,start_location_z:end_location_z));
    delta_temp_transit(i,2)=
mean(transit_corrected(i,start_location_x:end_location_x-15))-
mean(transit_corrected(i,1245:1260));
    delta_temp_transit(i,3)=
mean(transit_corrected(i,start_location_x:end_location_x-15))-
mean(transit_corrected(i,1292:1307));
end
```

```
%removal of unneccessary datapoint such as calibration baths, the cable
exiting the piles
%since the cold bath position on the lysimeter and waste rock cable is
%different, lys allows you to correct the original data without having
%to change the code. enter 2 for no removal, 1 for removal in lysimeter
%and 0 for removal in the waste rock/
x=dts.x;
tempdata=dts.tempdata;
if lys ==2
    x=dts.x;
    tempdata=dts.tempdata;
end
%locations of calibration baths and cables outside the rock pile in
lysimeter.
if lys==1
    for i=1:length(dts.x)
        if x(1,i) >= 0 && x(i)<= 46
            x(i)=nan;
            tempdata(:,i)=nan;
            temp_corrected(:,i)=nan;
            transit_corrected(:,i)=nan;
        else if x(i)>= 128 && x(i)<= 139
                x(i)=nan;
                tempdata(:,i)=nan;
                temp_corrected(:,i)=nan;
                transit_corrected(:,i)=nan;
            end
        end
        if x(1,i)>= 215 && x(1,i)<=232
            x(i)=nan;
            tempdata(:,i)=nan;
            temp_corrected(:,i)=nan;
            transit_corrected(:,i)=nan;
        else if x(i)>= 305 && x(i)<= 317
                x(i)=nan;
                tempdata(:,i)=nan;
                temp_corrected(:,i)=nan;
                transit_corrected(:,i)=nan;
            end
        end
        if x(i) >=309 && x(i) <=315
            x(i)=nan;
            tempdata(:,i)=nan;
            temp_corrected(:,i)=nan;
            transit_corrected(:,i)=nan;
        end
        if x(i)>= 389 && x(i)<= 436
            x(i)=nan;
            tempdata(:,i)=nan;
            temp_corrected(:,i)=nan;
            transit_corrected(:,i)=nan;
        else if x(i)>= 507 && x(i)<= 519
                x(i)=nan;
                tempdata(:,i)=nan;
```

```
                temp_corrected(:,i)=nan;
                transit_corrected(:,i)=nan;
            end
        end
        if x(i)>= 594 && x(i)<= 605
            x(i)=nan;
            tempdata(:,i)=nan;
        else if x(i)>= 682.5 && x(i)<= 695
                x(i)=nan;
                tempdata(:,i)=nan;
                temp_corrected(:,i)=nan;
                transit_corrected(:,i)=nan;
            end
        end
        if x(i)>= 774 && x(i)<= length(dts.x)
            x(i)=nan;
            tempdata(:,i)=nan;
            temp_corrected(:,i)=nan;
            transit_corrected(:,i)=nan;
            %          else if x(i)>= 779.5 & x(i)<= 788;
            %              x(i)=nan;
            %              tempdata(:,i)=nan;
            %              end
        end
    end
    %location of the calibration baths and cable outside the rock pile in
waste.
else if lys==0
        for i= 1:length(dts.x)
            if x(1,i) >= 0 && x(i)<= 69.5
                x(i)=nan;
                tempdata(:,i)=nan;
                temp_corrected(:,i)=nan;
                transit_corrected(:,i)=nan;
            else if x(i)>= 325 && x(i)<= 340
                    x(i)=nan;
                    tempdata(:,i)=nan;
                    temp_corrected(:,i)=nan;
                    transit_corrected(:,i)=nan;
                end
            end
            if x(i)>= 598 && x(i)<= 676
                x(i)=nan;
                tempdata(:,i)=nan;
                temp_corrected(:,i)=nan;
                transit_corrected(:,i)=nan;
            else if x(i)>= 935 && x(i)<= 948.5
                    x(i)=nan;
                    tempdata(:,i)=nan;
                    temp_corrected(:,i)=nan;
                    transit_corrected(:,i)=nan;
                end
            end
            if x(i)>= 1210 && x(i)<= length(dts.x)
```

```
                x(i)=nan;
                tempdata(:,i)=nan;
                temp_corrected(:,i)=nan;
                transit_corrected(:,i)=nan;
            end
            %         else if x(i)>= 310 & x(i)<= 316;
            %             x(i)=nan;
            %             tempdata(:,i)=nan;
            %             end
            %         end
            %         if x(i)>= 512 & x(i)<= 518;
            %             x(i)=nan;
            %             tempdata(:,i)=nan;
            %         else if x(i)>= 599 & x(i)<= 605;
            %             x(i)=nan;
            %             tempdata(:,i)=nan;
            %             end
            %         end
            %         if x(i)>= 685 & x(i)<= 692;
            %             x(i)=nan;
            %             tempdata(:,i)=nan;
            %         else if x(i)>= 779.5 & x(i)<= 788;
            %             x(i)=nan;
            %             tempdata(:,i)=nan;
            %             end
            %         end
        end
    end
end

%% creation of new structure to facilitate the storage of data. remember
which lys did you input to correctly name the structure.
corrected_dts_structure.notes='Corrected dts data structure';
corrected_dts_structure.juliandate=dts.juliandate;
corrected_dts_structure.k=dts.k;
corrected_dts_structure.offset_temp=temp_corrected;
corrected_dts_structure.transit_temp=transit_corrected;
corrected_dts_structure.x=x;
corrected_dts_structure.channel=dts.channel;
corrected_dts_structure.l=dts.l;
corrected_dts_structure.datestring=dts.datestring;
corrected_dts_structure.orginal_tempdata=dts.tempdata;
corrected_dts_structure.mean=mean(transit_corrected);
corrected_dts_structure.std=std(transit_corrected);
corrected_dts_structure.file=dts.file;

% data plotting
if plot_data==1
    figure
    plot(dts.juliandate,dts_bath(:,1),'ro')% Plot temperature bath data
    datetick
    hold on
    plot(dts.juliandate, test(:,1),'r--*')% Plot mean DTS data for bath
```

```
    plot(dts.juliandate, bath_temp_interp(:,1),'gx')% Plot corrected DTS
data
    plot(dts.juliandate,offset_correction(:,1),'b--x');
    hold off
    legend('DTS Bath Temperatures', 'Corrected DTS Bath Temperatures',
'Bath Temperatures','offset correction')
    grid
    ylabel('Temperature (C)')
    xlabel('Time')
    title ('Offset Correction coldbath')

    figure
    plot( dts.juliandate,dts_bath(:,2),'ro')% Plot temperature bath data
    datetick
    hold on
    plot(dts.juliandate, test(:,2),'r--*')% Plot mean DTS data for bath
    plot(dts.juliandate, bath_temp_interp(:,2),'gx')% Plot corrected DTS
data
    plot(dts.juliandate,offset_correction(:,2),'b--x');
    hold off
    legend('DTS Bath Temperatures', 'Corrected DTS Bath Temperatures',
'Bath Temperatures','offset correction')
    grid
    ylabel('Temperature (C)')
    xlabel('Time')
    title ('Offset Correction warmbath')

    figure;
    subplot(2,2,1);
    plot(x,tempdata);
    title('original data');
    xlabel('distance');
    ylabel('temperature in C');
    axis([0 max(dts.x) 0 30]); %set the limit depending on the dts
experiment.
    set(gca, 'ButtonDownFcn', @createnew_fig);

    subplot(2,2,2);
    plot(x,temp_corrected);
    hold on
    if transit==1
        plot(mid_coldbath,fit2);
    end
    hold off
    legend('temperature corrected');
    title('offset correction of raw data');
    xlabel('distance');
    ylabel('temperature in C');
    axis([0 max(dts.x) 0 30]);
    set(gca, 'ButtonDownFcn', @createnew_fig);

    subplot(2,2,3);
    plot(x,temp_corrected-transit_correction);
    legend('transit corrected data');
```

```
    title('Transit correction');
    xlabel('distance');
    ylabel('temperature in C');
    axis([0 max(dts.x) 0 30]);
    set(gca, 'ButtonDownFcn', @createnew_fig);

    subplot(2,2,4);
    plot(delta_temp_transit(:,1));
    hold on
    plot(delta_temp_transit(:,2));
    plot(delta_temp_transit(:,3));
    hold off
    legend('first and final bath', 'first and second','first and third');
    title('temperature difference between the cold baths in the surface
experiment');
    xlabel('number of timesteps');
    ylabel('temperature in degree celsius');
    xlim([0 max(dts.k)]); ylim([-30 30]);
    set(gca, 'ButtonDownFcn', @createnew_fig);

    figure;
    scatter(x,tempdata(1,:),'.');
    hold on
    scatter(x,temp_corrected(1,:),'.');
    scatter(x,transit_corrected(1,:),'.');
    hold off
    legend('original data','offset correction','transit correction');
    title('Dts 20160609 temperature distribution in the surface layer of
the waste rock pile')
    xlabel('distance in meters');
    ylabel('temperature in degree celsius');

    figure;
    if transit ==1
        pcolor(x,dts.juliandate,transit_corrected);
        %caxis([min(min(transit_corrected)) max(max(transit_corrected))]);
    else if transit==0
            pcolor(x,dts.juliandate,temp_corrected);
            if min(min(temp_corrected)) >= -2 && max(max(temp_corrected))
<= 15
                %caxis([min(min(temp_corrected))
max(max(temp_corrected))]);
            else if min(min(temp_corrected)) <= -2 &&
max(max(temp_corrected)) >= 15
                    %caxis([25 60]);
                end
            end
        end
    end
    set(gca,'layer','top')
    shading interp;
    datetick('y');
    xlabel('distance');
    ylabel('time');
```

```
    title('DTS temperature distribution');
    if lys == 1
        xlim([0 818]);
    else if lys == 0
            xlim([0 1277]);
        end
    end
    caxis ([0 30]);
    colorbar;
end
```